# POLITECNICO DI MILANO

Scuola di Ingegneria Industriale e dell'Informazione

Corso di Laurea Magistrale in Ingegneria Biomedica
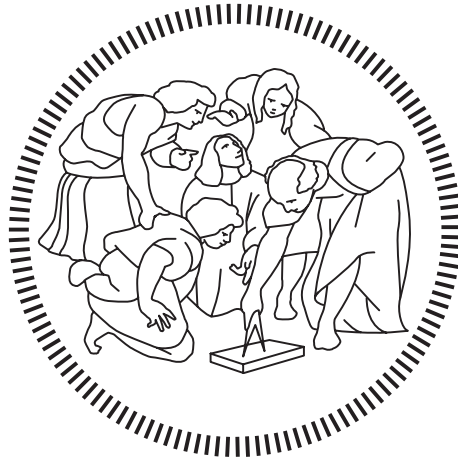
Development of a mechanically active, multi-tissue microfluidic device for the culture of three-dimensional osteochondral tissues

Relatore: Prof. Marco Rasponi

Correlatori: Prof. Andrea Barbero

Andrea Mainardi

Tesi di laurea di:

Mariuzzo Federico 916168

Anno accademico 2019/2020

RINGRAZIAMENTI

TABLE OF CONTENTS

TABLE OF CONTENTS

TABLE OF CONTENTS

LIST OF ABBREVIATIONS

1D	One-dimensional
2D	Bidimensional
3D	Three-dimensional
ACAN	Aggrecan
ACI	Autologous Chondrocyte Implantation
ADAMTS	A Disintegrin and Metalloproteinase with Thrombospondin motifs
ALP	Alkaline Phosphatase
BGLAP	Bone Gamma-Carboxyglutamate Protein
BMI	Body Mass Index
BMP	Bone Morphogenetic Protein
BPE	Biphasic Poroelastic
BPVE	Biphasic Poroviscoelastic
CAD	Computer-Aided Design
cDNA	Complementary Deoxyribonucleic Acid
CHM	Chondrogenic Medium
CLSM	Confocal Laser Scanning Microscopy
CM	Complete Medium
COL10A1	Collagen type X alpha 1 chain
COL11A2	Collagen type XI alpha 2 chain
COL1A1	Collagen type I alpha 1 chain
COL2A1	Collagen type II alpha 1 chain
COL9A1/2/3	Collagen type IX alpha 1, 2 and 3 chains
COMP	Cartilage Oligomeric Matrix Protein
CXCL8	C-X-C Motif Chemokine Ligand 8
DAPI	4',6-diamidino-2-phenylindole
DKK1	Dickkopf-related protein 1
DMEM	Dulbecco's Modified Eagle Medium
DMSO	Dimethyl Sulfoxide
dNTP	Deoxynucleotide Triphosphate
DTT	Dithiothreitol

LIST OF ABBREVIATIONS

ECM	Extracellular Matrix
EDTA	Ethylenediaminetetraacetic Acid
FACS	Fluorescence-Activated Cell Sorting
FBS	Fetal Bovine Serum
FDA	Food and Drug Administration
FGF	Fibroblast Growth Factor
FN1	Fibronectin
FRZB	Frizzled Related Protein
GAG	Glycosaminoglycan
GAPDH	Glyceraldehyde-3-phosphate Dehydrogenase
GFP	Green Fluorescent Protein
Gln	Glutamine
GREM1	Gremlin1
HACs	Human Articular Chondrocytes
HAPLN1	Hyaluronan And Proteoglycan Link Protein 1
HEPES	4-(2-hydroxyethyl)-1-piperazineethanesulfonic Acid
HSA	Human Serum Albumin
HUVECs	Human Umbilical Vein Endothelial Cells
IBSP	Integrin Binding Sialoprotein
IGF-1	Insulin-like Growth Factor 1
IgG	Immunoglobulin G
IHH	Indian Hedgehog
IL	Interleukin
IQR	Interquartile Range
ITS	Insulin-Transferrin-Sodium Selenite
LECT1	Leukocyte cell derived chemotaxin 1
Lys	Lysine
MACI	Matrix-induced Autologous Chondrocyte Implantation
MCP-1	Monocyte Chemoattractant Protein 1
MEM α	Minimum Essential Medium Alpha
MMP	Matrix Metalloproteinase
MRI	Magnetic Resonance Imaging

LIST OF ABBREVIATIONS

MSCs	Mesenchymal Stem Cells
NCs	Nasal Chondrocytes
NE	Nominal Strain
NGF	Nerve Growth Factor
NO	Nitric Oxide
NSAIDs	Nonsteroidal Anti-inflammatory Drugs
OA	Osteoarthritis
OCM	Osteochondral Medium
PBS	Phosphate Buffered Saline
PCR	Polymerase Chain Reaction
PDMS	Polydimethylsiloxane
PEG	Polyethylene Glycol
PG	Proteoglycan
PGE2	Prostaglandin E2
PSG	Penicillin-Streptomycin-Glutamine
qPCR	Quantitative Polymerase Chain Reaction
RNA	Ribonucleic Acid
ROI	Region of Interest
RT-qPCR	Quantitative Reverse Transcription-Polymerase Chain Reaction
RUNX2	Runt-related Transcription Factor 2
SD	Standard Deviation
SOX	SRY-Box Transcription Factor
TBS	Tris Buffered Saline
TGF	Transforming Growth Factor
TMCS	Trimethylchlorosilane
TNF-α	Tumour Necrosis Factor Alpha
TRPV4	Transient Receptor Potential Vanilloid 4
UV	Ultraviolet
VEGF	Vascular Endothelial Growth Factor
YLD	Years Lived with Disability
ZCC	Zone of Calcified Cartilage

ABSTRACT

INTRODUCTION

Osteoarthritis (OA) is a degenerative joint disease, and a major source of pain, disability and socioeconomic cost worldwide [1], with 15 million new cases diagnosed every year [2].

Current therapies, including lifestyle modification and pharmacological treatments [1], are all aimed at alleviating symptoms, while there are no available effective disease-modifying drugs able to reverse the degenerative process [3]. As a result, prosthetization remains the only option to restore joint functionality in severe cases [3]. While several new approaches for OA treatment, both pharmaceutical and regenerative [4], are being investigated, a deeper understanding of the pathogenesis and underlying mechanisms of this pathology is still required.

OA is in fact widely recognized as a multi-aetiological, complex pathology affecting the joint as a whole. Joint tissues such as hyaline cartilage, calcified cartilage, subchondral bone, and synovium are all affected [5]. Hyaline cartilage is an avascular and aneural tissue, populated by a single cell type: chondrocytes. Its major organic components are collagen type II and aggrecan. During OA, hyaline cartilage undergoes

alterations such as inflammation, extracellular matrix (ECM) degradation, vascularisation, and chondrocyte hypertrophy [5], [6]. Hyaline cartilage lies on calcified cartilage, a thin tissue layer populated by hypertrophic chondrocytes. One of the hallmarks of OA is the duplication of the tidemark, the interface between hyaline and calcified cartilage. Other alterations of calcified cartilage include vascularisation and development of regions of new bone formation [5]. Subchondral bone is the bone layer lying immediately beneath cartilage. It can be divided into two distinct anatomical entities, namely cortical plate and subchondral trabecular bone. OA is associated with an increased cortical plate thickness and a reduced bone stiffness [5], [7]. Finally, another tissue affected by OA is the synovium, a connective tissue lining diarthrodial joints, which undergoes hyperplasia and inflammation [8].

OA models, both *in vivo* and *in vitro*, are vital for the development and testing of new potential therapies. While *in vivo* models provide the most accurate reflection of the naturally occurring whole-joint disease, they are costly, time-consuming and seldom allow a deep dissection of the degenerative mechanisms [9], [10]. Moreover, the ease of manipulating in vitro systems, as well as a shift towards the 3R's principle of refining, reducing and replacing the use of animal

experimentation, makes *in vitro* modelling of OA desirable [10]. No satisfactory *in vitro* models, however, are yet available. Traditional monolayer cell culture models provide a too simplistic description of the pathology, and chondrocytes are known to dedifferentiate in a 2D, ECM-free environment [10]. Also, several 3D models of OA have been developed [10]. While 3D systems at the macroscale are more accurate in the recapitulation of OA, and allow the introduction of mechanical stimuli, which play a major role in this pathology, they are often cumbersome to use, and difficult to implement into high-throughput drug discovery campaigns, where parallelization is of the utmost importance [11].

The application of microfluidics to cell biology studies, with the development of organs-on-a-chip, recently opened up new perspectives, making it possible to provide cells with accurate biochemical and biomechanical stimuli and with a precisely tailored 3D microenvironment [12]. Moreover, the reduced scale determines a reduction of experimental costs and time, and facilitates the implementation of high-throughput analyses [13]. A previous study has already proven the feasibility of developing a representative microfluidic model of OA [14]. This model, however, only focused on hyaline cartilage, while OA is widely recognized as a whole joint pathology [5]. Therefore, a multi-tissue model is needed to better recapitulate its complexity.

In this framework, the present work aimed at developing a microfluidic device for the culture and mechanical stimulation of two 3D hydrogel-based cell constructs with a direct interface. The device was used to generate mature osteochondral constructs with a hyaline cartilage compartment (derived from human articular chondrocytes, HACs) and a calcified cartilage compartment (derived from mesenchymal stem cells, MSCs). Moreover, the induction of some key features of OA in the constructs through the application of a cyclic hyperphysiological compression was demonstrated.

MATERIALS AND METHODS
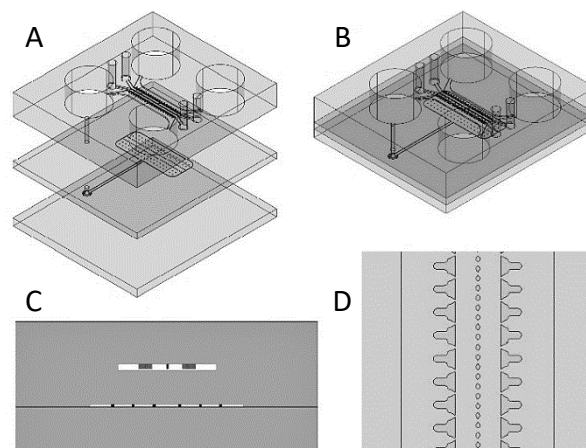
Fig. 1: A) exploded view of the three layers composing the device, namely the culture chamber (top), the actuation membrane (middle), and the floor (bottom); B) 3D view of the assembled device. A single functional unit, composed of a culture chamber and an actuation chamber, is shown. The whole device comprises three flanked functional units; C) section of the culture chamber and the actuation chamber; D) top view of the four channels composing the culture chamber.

ABSTRACT

A sketch of the engineered microfluidic device is shown in Fig. 1. The device consists in three polydimethylsiloxane (PDMS) layers: a culture chamber, an actuation membrane, and a floor. The culture chamber is composed of two central channels, where two different hydrogel-based cell constructs can be injected (one representing hyaline cartilage, the other calcified cartilage), and two lateral channels for the culture medium. The gel channels are separated from the medium channels by a row of T-shaped, overhanging lateral pillars. A gap is present between the bottom surface of the pillars and the underlying membrane. The membrane and the floor are sealed together forming an actuation chamber. When the actuation chamber is pressurised, the membrane bends upwards until it abuts against the pillars, delivering strain-controlled compressive stimuli to the cell constructs.

Three different versions of the device were designed. Features with different geometries were considered, to allow the injection of different hydrogels in the two central channels while guaranteeing a direct interface between them. Hexagonal shaped pillars and a continuous overhanging wall were considered as alternatives to separate the two hydrogels. Moreover, devices that could deliver either a symmetric mechanical stimulation, providing both cell constructs with the same strain level, or an asymmetric stimulation, compressing the hyaline cartilage construct more than the calcified cartilage one, were designed and realized.

The culture chamber was dimensioned to guarantee an adequate diffusion of nutrients and chemicals within the cell constructs and to achieve the desired hyperphysiological compression level, set to 30% according to literature [14]. Widths of 300 and 500 μm were adopted for the gel channels; the heights of the pillars and the gap were set to 100 μm and 43 μm, respectively, leading to a total culture chamber height of 143 μm. Lateral pillars were designed to minimize the lateral expansion of cell constructs upon compression, reduce the leakage probability during the hydrogel injection (according to a modified capillary burst valve model [15]) and provide a sufficient contact surface between the constructs and the culture medium.

Finite element models were implemented to evaluate the strain field within the cell constructs in the different device versions. PDMS was described as a Mooney-Rivlin hyperelastic material, while a biphasic poroelastic model was adopted for the hydrogel-based constructs, both for the hyaline cartilage compartment and for the calcified cartilage one. Only the Young modulus was varied between the two compartments: 100 kPa for the hyaline

ABSTRACT

cartilage construct, and 200 kPa for the calcified cartilage one.

Microfluidic devices were fabricated through soft lithography techniques. The geometrical features were translated into masks for soft lithography. Two masks were produced for the culture chamber (one corresponding to the pillars and one to the gap), and one for the actuation membrane. No masks were needed for the floor of the device, being its surface unpatterned. The features were transferred onto silicon wafers by photolithography. The wafers were subsequently used as master molds for the production of the PDMS layers. Liquid PDMS was poured onto the patterned master molds for the culture chamber and the actuation chamber. The unpatterned floor of the device was obtained by pouring PDMS onto a Petri dish. The polymer was allowed to reticulate on a levelled shelf at 65°C for two and a half hours. The obtained layers were exposed to air plasma and sealed together.

A geometrical characterization of the devices was performed, assessing the accuracy of the fabrication process. Thin sections of the culture chamber were obtained. The height of the pillars and the gap was measured, and used to calculate the compression level produced by the devices. The optimal actuation pressure, required to make the actuation membrane abut against the pillars, was also experimentally assessed.

Microfluidic devices were then used to generate a cellular model of OA. The biological phase of the work was articulated into several steps: first, an optimization of the culture parameters for the generation of MSCs-based calcified cartilage constructs in single culture and the induction of OA traits in these constructs was performed; secondly, the maturation of osteochondral cell constructs with a hyaline cartilage compartment and a calcified cartilage compartment was assessed; finally, the induction of OA traits in the osteochondral constructs through the application of a cyclic hyperphysiological compression was evaluated.

To generate the osteochondral constructs, MSCs and HACs were laden into 2% enzymatically crosslinkable and cleavable eight-arm polyethylene glycol (PEG) hydrogels [16], and seeded into the devices. Two weeks of conditioning with 10 ng/ml transforming growth factor (TGF)-β3, Dexamethasone 10^{-7} M, β-Glycerophosphate 10 mM and ascorbic acid 0.1 mM in static conditions were carried on. Tissue maturation and ECM deposition were analysed through phase contrast microscopy and immunofluorescence. Constructs were stained for cell nuclei, hydroxyapatite, aggrecan and collagen type II at different time points (namely day 0, day 7

13

ABSTRACT

and day 14). Quantitative reverse transcription-polymerase chain reaction (RT-qPCR) was used to further investigate tissue maturation at the gene level. The constructs were subjected to enzymatic digestion and cell sorting prior to RT-qPCR, to separate HACs and MSCs-derived hypertrophic chondrocytes. For this reason, HACs modified to express green fluorescent protein (GFP) had to be used for the constructs to be analysed through RT-qPCR. Genes associated with chondrogenesis (ACAN), chondrocyte hypertrophy (COL10A1), mineralization (ALPL), and bone formation (IBSP) were analysed at day 0 and day 14.

To assess the effect of hyperphysiological compression on the constructs, MSCs and GFP-expressing HACs were seeded into the devices and cultured for two weeks in static conditions and one further week under cyclic mechanical stimulation. At day 21, cells were sorted based on GFP expression, and RT-qPCR was performed. Constructs subjected to mechanical stimulation and static controls were compared. Genes associated with hypertrophy inhibition (FRZB), inflammation (CXCL8), catabolism (MMP13), mineralization (ALPL), and bone formation (BGLAP) were considered to evaluate the acquisition of OA traits in the two tissues following hyperphysiological loading.

RESULTS

An evaluation of the strain field within the hyaline cartilage and the calcified cartilage compartments upon compression, in both the symmetric and the asymmetric configuration, was provided by the finite element models of the device. Fig. 2 shows a contour plot of the nominal strain along the vertical direction in the two device configurations.
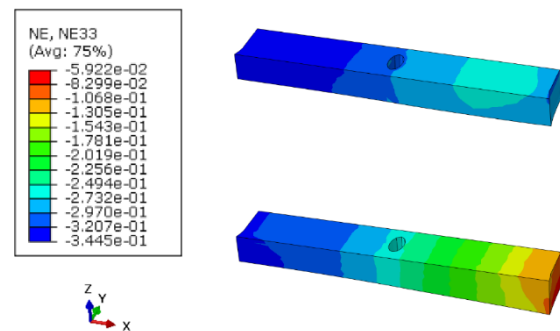
Fig. 2: contour plot of the strain along the vertical direction within the hydrogels, in the symmetric (top) and asymmetric (bottom) configuration of the device. The calcified cartilage construct is on the right, the hyaline cartilage one on the left.

In the symmetric configuration, the strain along the vertical direction (NE33) and the lateral strain (NE11) were -31.3% ± 1.5% and -0.8% ± 2.0% in the hyaline cartilage compartment and -27.5% ± 1.6% and 1.7% ± 2.4% in the calcified cartilage compartment, respectively (median ± interquartile range, IQR). In the asymmetric configuration, NE33 and NE11 were 30.2% ± 4.6% and 0.4% ± 3.6% in the hyaline cartilage compartment and -17.4% ± 12.0% and 0.1% ± 7.4% in the calcified cartilage compartment, respectively. The strain along the axial direction (NE22) was negligible in both configurations.

ABSTRACT

The geometrical characterization of the devices demonstrated the accuracy of the fabrication process. Achieved compression levels were in line with the target value of 30% for all the device versions. The characterization of the optimal actuation pressure produced a final value of 400 millibars, which was adopted for all the following biological experiments.

Once the characterization of the devices was complete, they were exploited to generate a cellular model of OA. The culture parameters for the achievement of mature hyaline cartilage constructs in a microfluidic device were known [17], while little knowledge was available on the differentiation of MSCs into hypertrophic chondrocytes and their behaviour when subjected do deleterious mechanical stimuli. A characterization of these matters was performed as a necessary preconcept of the more complex OA osteochondral model.

A mature calcified cartilage construct was achievable after 14 days of static culture. Genes associated with chondrogenesis (ACAN and COL2A1), chondrocyte hypertrophy (COL10A1 and IHH), mineralization (ALPL), and bone formation (IBSP) were all upregulated. Moreover, Calcein staining revealed the deposition of a mineralized matrix.

After the achievement of a mature construct, the effect of hyperphysiological compression was evaluated. Gene expression analysis revealed a 5.5-fold downregulation of the hypertrophy inhibitor FRZB, a 2.8-fold upregulation of the bone marker BGLAP, and a 3.7-fold downregulation of the antiangiogenic factor LECT1.
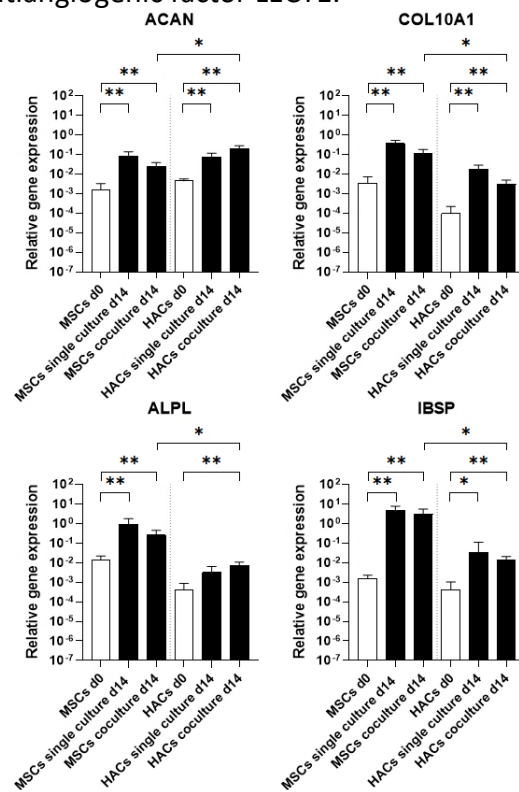
Fig. 3: *expression levels of relevant genes in the osteochondral constructs at day 0 and day 14. Mean and standard deviation (SD) are reported. Statistical significance was determined by Mann-Whitney test. * p < 0.05, ** p < 0.01.*

Once the characterization of calcified cartilage constructs in single culture was performed, the maturation of healthy osteochondral constructs was assessed. After 14 days of static coculture, HACs and MSCs-derived hypertrophic chondrocytes were able to maintain their respective gene signatures. RT-qPCR showed a higher expression of ACAN (8.4-fold) in the hyaline cartilage compartment at day 14 with respect to the

calcified cartilage one. The expression of COL10A1 was significantly lower (39-fold) in the hyaline cartilage compartment as compared to the calcified cartilage one. The expression levels of ALPL and IBSP were respectively 35-fold and 215-fold higher in the calcified cartilage compartment as compared to the hyaline cartilage one. All the genes were upregulated at day 14 as compared to day 0, in both compartments (Fig. 3).
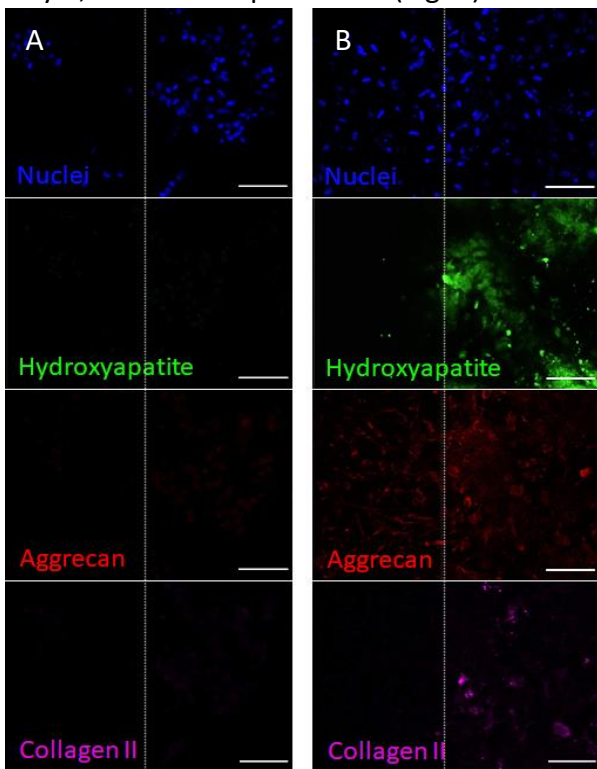
Fig. 4: *immunofluorescence analysis of osteochondral constructs at day 0 (A) and day 14 (B). The dashed lines indicate the interface between the hyaline cartilage construct (on the left) and the calcified cartilage construct (on the right). Scale bar 100 µm.*

Retainment of distinct differentiation profiles was confirmed by matrix deposition analyses. Immunofluorescence revealed the deposition of a mineralized matrix in the calcified cartilage compartment, while the hyaline cartilage compartment remained non-

mineralized. Aggrecan was detected in both compartments, suggesting the development of cartilaginous constructs. However, collagen type II, another marker of chondrogenesis, was only detected in the calcified cartilage compartment (Fig. 4).

The effect of symmetric or asymmetric hyperphysiological compression on the osteochondral constructs was assessed.
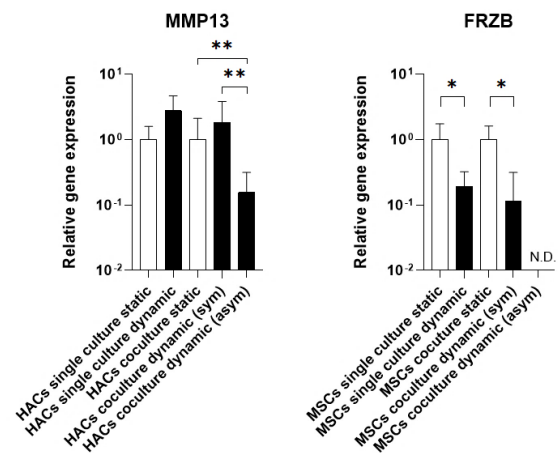
Fig. 5: *expression levels of relevant genes in the osteochondral constructs subjected to hyperphysiological compression. Mean and SD are reported. Statistical significance was determined by Mann-Whitney test. * p < 0.05, ** p < 0.01.*

In the hyaline cartilage compartment, hyperphysiological compression induced a 1.8-fold upregulation of MMP13 in the symmetric configuration of the device and a 6.4-fold downregulation in the asymmetric configuration. CXCL8 was upregulated in both the configurations with respect to static controls. The increase was 2.4-fold in the symmetric configuration of the device and 1.2-fold in the asymmetric one. FRZB was downregulated in both the configurations, 1.3-fold and 2.1-fold, respectively. In the calcified cartilage compartment,

16

hyperphysiological compression induced a 1.2-fold upregulation of BGLAP in the symmetric configuration and a 1.4-fold upregulation in the asymmetric configuration. ALPL was upregulated in both the configurations, 2.1-fold and 1.8-fold, respectively. FRZB was 5.2-fold downregulated in the symmetric configuration. This gene was not detected in any of the analysed samples for the asymmetric device configuration, due to the low amount of genetic material obtained after enzymatic digestion and cell sorting (Fig. 5).

DISCUSSION

In the present work, a microfluidic device for the coculture and the mechanical stimulation of two 3D cell constructs with a direct interface was developed.

Finite element models of the device demonstrated the possibility to obtain a confined compression of the constructs with the adopted design. Overall, the computed strain field was in line with the project requirements for the symmetric configuration of the device, while some discrepancies were found for the asymmetric configuration. In particular, this configuration produced an inhomogeneous strain in the hyaline cartilage compartment, and a strain appreciably different from the target one in the calcified cartilage compartment. Anyway, it was

considered to represent a good compromise between the different optimal conditions required for the two tissues, and it was used without further modifications.

The devices were used to generate a load-based, multi-tissue cellular model of OA, representing two tissues greatly involved in this pathology, namely hyaline cartilage and calcified cartilage.

Preliminary biological tests allowed to optimise the culture conditions for the generation of MSCs-derived calcified cartilage constructs, serving as a basis for the more complex osteochondral model. Moreover, the application of a cyclic hyperphysiological compression on the constructs allowed to replicate some of the key features of the zone of calcified cartilage in a native osteoarthritic joint, such as an enhanced chondrocyte hypertrophy, a higher proneness to vascularization, and the development of regions of new bone formation [5].

Once the preliminary experiments were complete, the devices were exploited to generate healthy osteochondral cell constructs. Mature cartilaginous tissues with two distinct compartments, one of which mineralized, the other non-mineralized, were achieved after two weeks of static culture.

Finally, the devices were used to expose the osteochondral constructs to cyclic hyperphysiological compression, recreating

the condition of mechanical overloading typical of the native osteoarthritic joint. While the asymmetric configuration of the device produced contradictory results, the symmetric configuration allowed to replicate some hallmarks of OA, such as chondrocyte hypertrophy, catabolism, and inflammation in hyaline cartilage, as well as hypertrophy and proneness to bone formation in calcified cartilage. However, further studies considering a larger pool of cell donors are needed to come to more reliable conclusions.

CONCLUSIONS AND FUTURE DEVELOPMENTS

A mechanically active, PDMS-based microfluidic device was designed, fabricated, and successfully exploited to generate 3D multi-tissue osteochondral constructs. The device guaranteed an adequate diffusion of nutrients and differentiation factors within the constructs and was compatible with medium-long term cell culture. Furthermore, it was able to provide the constructs with defined compressive stimuli, resembling the condition of mechanical overloading typical of the native osteoarthritic joint. A repetition of the performed experiments, considering a larger pool of cell donors and samples, is required to confirm the obtained biological results.

After a more complete validation, the newly developed model could be used to test possible innovative anti-OA therapies, targeting different aspects of the pathology not recapitulated by previous models (e.g., the advancement of bone formation in the deeper cartilage layers). Moreover, the introduction into the model of additional tissues involved in OA, such as vasculature, could provide a deeper understanding of this pathology. The addition of other cell types, however, would require the possibility to use different medium compositions for the different tissues cultured in the device. This feature could be achieved by integrating the microfluidic device developed in the present work with a perfusion system able to generate a continuous flow of medium in its lateral channels, and a stable gradient between the two hydrogel compartments. Finally, some modifications to the device design could be implemented to achieve a strain field more representative of the one found in the native joint, where the two tissues are overlying and not flanked.

Overall, the introduction of these features in a microfluidic device would represent a further step towards the development of a model of joint-on-a-chip, able to fully recapitulate *in vitro* the complexity of OA.

BIBLIOGRAPHY

[1] S. Glyn-Jones et al., "Osteoarthritis," Lancet, vol. 386, no. 9991, pp. 376–387, 2015, doi: 10.1016/S0140-6736(14)60802-3.

[2] L. March, M. Cross, N. Arden, and G. Hawker, "Osteoarthritis: A Serious Disease, Submitted to the U. S. Food and Drug Administration," Oarsi, pp. 1–103, 2016.

[3] M. Kloppenburg and F. Berenbaum, "Osteoarthritis year in review 2019: epidemiology and therapy," Osteoarthr. Cartil., vol. 28, no. 3, pp. 242–248, 2020, doi: 10.1016/j.joca.2020.01.002.

[4] S. Grässel and D. Muschter, "Recent advances in the treatment of osteoarthritis," F1000Research, vol. 9, no. May, 2020, doi: 10.12688/f1000research.22115.1.

[5] S. R. Goldring and M. B. Goldring, "Changes in the osteochondral unit during osteoarthritis: Structure, function and cartilage bone crosstalk," Nat. Rev. Rheumatol., vol. 12, no. 11, pp. 632–644, 2016, doi: 10.1038/nrrheum.2016.148.

[6] S. Suri and D. A. Walsh, "Osteochondral alterations in osteoarthritis," Bone, vol. 51, no. 2, pp. 204–211, 2012, doi: 10.1016/j.bone.2011.10.010.

[7] G. Li et al., "Subchondral bone in osteoarthritis: Insight into risk factors and microstructural changes," Arthritis Res. Ther., vol. 15, no. 6, 2013, doi: 10.1186/ar4405.

[8] M. J. Benito, D. J. Veale, O. FitzGerald, W. B. Van Den Berg, and B. Bresnihan, "Synovial tissue inflammation in early and late osteoarthritis," Ann. Rheum. Dis., vol. 64, no. 9, pp. 1263–1267, 2005, doi: 10.1136/ard.2004.025270.

[9] P. J. Cope, K. Ourradi, Y. Li, and M. Sharif, "Models of osteoarthritis: the good, the bad and the promising," Osteoarthr. Cartil., vol. 27, no. 2, pp. 230–239, 2019, doi: 10.1016/j.joca.2018.09.016.

[10] C. I. Johnson, D. J. Argyle, and D. N. Clements, "In vitro models for the study of osteoarthritis," Vet. J., vol. 209, pp. 40–49, 2016, doi: 10.1016/j.tvjl.2015.07.011.

[11] C. Probst, S. Schneider, and P. Loskill, "High-throughput organ-on-a-chip systems: Current status and remaining challenges," *Curr. Opin. Biomed. Eng.*, vol. 6, pp. 33–41, 2018, doi: https://doi.org/10.1016/j.cobme.2018.02.004.

[12] D. Huh, G. A. Hamilton, and D. E. Ingber, "From 3D cell culture to organs-on-chips," Trends Cell Biol., vol. 21, no. 12, pp. 745–754, 2011, doi: 10.1016/j.tcb.2011.09.005.

[13] S. K. Sia and G. M. Whitesides, "Microfluidic devices fabricated in poly(dimethylsiloxane) for biological studies," Electrophoresis, vol. 24, no. 21, pp. 3563–3576, 2003, doi: 10.1002/elps.200305584.

[14] P. Occhetta et al., "Hyperphysiological compression of articular cartilage induces an osteoarthritic phenotype in a cartilage-on-a-chip model," Nat. Biomed. Eng., vol. 3, no. 7, pp. 545–557, 2019, doi:10.1038/s41551-019-0406-3.

[15] C. P. Huang et al., "Engineering microscale cellular niches for three-dimensional multicellular co-cultures," Lab Chip, vol. 9, no. 12, pp. 1740–1748, 2009, doi: 10.1038/jid.2014.371.

[16] M. Ehrbar et al., "Biomolecular hydrogels formed and degraded via site-specific enzymatic reactions," Biomacromolecules, vol. 8, no. 10, pp. 3000–3007, 2007, doi: 10.1021/bm070228f.

[17] A. Mainardi, "Towards the knee on a chip: development of a microfluidic platform for the mechanical stimulation of three dimensional cartilaginous constructs," 2016.

SOMMARIO

INTRODUZIONE

L'osteoartrosi (OA) è una patologia articolare degenerativa, e una delle maggiori cause globali di dolore, disabilità e costo socioeconomico [1], con 15 milioni di nuovi casi diagnosticati ogni anno [2].

Le terapie attualmente in uso, dalle modifiche allo stile di vita ai trattamenti farmacologici [1], hanno il solo scopo di alleviare i sintomi, mentre non sono disponibili soluzioni in grado di invertire il processo degenerativo [3]. L'artroplastica rimane l'unica opzione per ripristinare il funzionamento articolare nei casi più severi [3]. Malgrado numerosi approcci innovativi per il trattamento dell'OA, sia farmaceutici sia rigenerativi, siano in fase di studio [4], resta necessaria una maggiore comprensione della patogenesi e dei meccanismi di questa patologia.

L'OA interessa vari tessuti all'interno dell'articolazione, ovvero cartilagine ialina, cartilagine calcificata, osso subcondrale e sinovio [5]. La cartilagine ialina è un tessuto avascolare e aneurale, popolato da un unico tipo cellulare: i condrociti. I suoi maggiori costituenti organici sono il collagene di tipo II e l'aggrecano. Durante l'OA, questo tessuto è affetto da profonde alterazioni, tra cui infiammazione, degradazione della normale matrice extracellulare (ECM), angiogenesi e ipertrofia [5], [6]. La cartilagine ialina giace sulla cartilagine calcificata, uno strato tissutale popolato da condrociti ipertrofici. Un tratto fondamentale dell'OA è la duplicazione del fronte di mineralizzazione tra i due tessuti. Altre alterazioni della cartilagine calcificata includono l'angiogenesi e la formazione di regioni di ossificazione [5]. L'osso subcondrale è lo strato osseo posto immediatamente sotto la cartilagine. È suddiviso in osso corticale e trabecolare. L'OA è associata a un ispessimento dello strato corticale e a una riduzione della rigidezza ossea [5], [7]. Infine, il sinovio, un tessuto connettivo specializzato che riveste le articolazioni, è affetto da infiammazione e ipertrofia a causa dell'OA [8].

I modelli di OA, sia *in vivo* sia *in vitro*, sono di vitale importanza per lo sviluppo e la sperimentazione di nuove potenziali terapie. I modelli *in vivo* sono i più accurati nel ricapitolare il processo patologico naturale, ma sono costosi, di lunga durata e raramente permettono un'analisi approfondita dei meccanismi degenerativi [9], [10]. Inoltre, la facile manipolazione dei sistemi *in vitro*, insieme al principio di affinamento, riduzione e sostituzione della sperimentazione animale, rende desiderabile la modellizzazione *in vitro* dell'OA [10]. Tuttavia, non sono ancora presenti dei modelli *in vitro* soddisfacenti di OA. I modelli tradizionali, basati sulla coltura in monostrato,

forniscono infatti una descrizione troppo semplicistica della patologia, e i condrociti tendono a de-differenziare in un ambiente 2D e privo di ECM [10]. Inoltre, sono stati sviluppati molti modelli 3D di OA [10]. Sebbene i sistemi 3D alla macro-scala siano più accurati nel ricapitolare l'OA, e permettano di introdurre stimoli meccanici, che hanno un ruolo fondamentale nello sviluppo della patologia, essi risultano spesso ingombranti e di difficile utilizzo in campagne di sviluppo farmaceutico ad alto rendimento, dove la parallelizzazione è fondamentale [11].

L'applicazione della microfluidica alla biologia cellulare, insieme allo sviluppo degli organi su chip, ha aperto nuove prospettive, grazie alla possibilità di fornire alle cellule stimoli biochimici e biomeccanici accurati, e un microambiente 3D realizzato su misura [12]. Inoltre, la riduzione di scala permette di diminuire costi e durata degli esperimenti, e facilita l'implementazione di analisi ad alto rendimento [13]. Uno studio precedente ha già dimostrato la fattibilità di un modello microfluidico di OA [14]. Questo studio, tuttavia, si è focalizzato esclusivamente sulla cartilagine ialina, mentre l'OA interessa l'intera articolazione [5]. Di conseguenza, per ricapitolare più accuratamente la complessità della patologia è necessario un modello multi-tessuto.

In questo contesto, l'obiettivo del presente lavoro è sviluppare un dispositivo microfluidico per la coltura e la stimolazione meccanica di due costrutti cellulari 3D a base di idrogeli aventi un'interfaccia diretta. Il dispositivo è stato utilizzato per generare dei costrutti osteocondrali maturi, con un compartimento di cartilagine ialina (derivata da condrociti articolari umani, HACs) e un compartimento di cartilagine calcificata (derivato da cellule mesenchimali, MSCs). Inoltre, è stata valutata l'induzione nei costrutti di alcuni tratti tipici dell'OA, tramite l'applicazione di una compressione sovrafisiologica ciclica.

MATERIALI E METODI
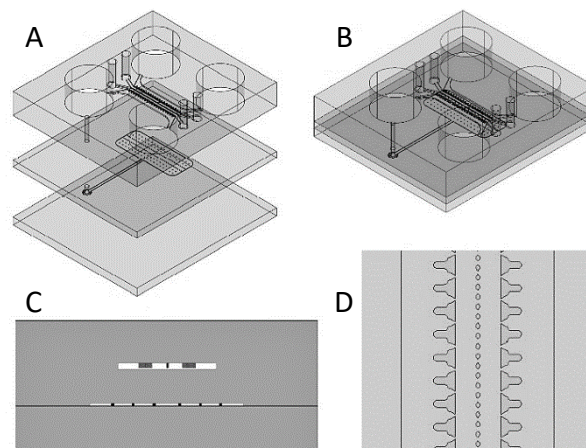
Fig. 1: A) vista esplosa dei tre strati del dispositivo, ovvero la camera di coltura (in alto), la membrana di attuazione (in mezzo) e il pavimento (in basso); B) vista 3D del dispositivo assemblato. È mostrata una singola unità funzionale, composta da una camera di coltura e una camera di attuazione. Il dispositivo comprende tre unità funzionali affiancate; C) sezione della camera di coltura e della camera di attuazione; D) vista dall'alto dei quattro canali che compongono la camera di coltura.

Uno schema del dispositivo microfluidico è mostrato in Fig. 1. Il dispositivo

consiste in tre strati realizzati in polidimetilsilossano (PDMS): una camera di coltura, una membrana di attuazione e un pavimento. La camera di coltura è composta da due canali centrali, in cui possono essere iniettati due diversi costrutti cellulari a base di idrogeli (uno per modellizzare la cartilagine calcificata, uno per quella ialina), e due canali laterali per il mezzo di coltura. I canali centrali sono separati da quelli laterali da una serie di micro-colonne sospese con sezione a T. Uno spazio vuoto è presente tra la membrana e la superficie inferiore delle micro-colonne. La membrana e il pavimento sono sigillati insieme a formare una camera di attuazione. Quando la camera di attuazione viene pressurizzata, la membrana si piega verso l'alto fino a raggiungere le micro-colonne, comprimendo i costrutti cellulari.

Sono state sviluppate tre versioni del dispositivo. Diverse geometrie, ovvero delle micro-colonne esagonali e una parete sospesa continua, sono state considerate, in modo da consentire l'iniezione di due diversi idrogeli nei canali centrali, garantendo allo stesso tempo un'interfaccia diretta tra essi. Inoltre, sono stati sviluppati e realizzati dispositivi in grado produrre una stimolazione meccanica simmetrica, per comprimere entrambi i costrutti allo stesso modo, o asimmetrica, per comprimere la cartilagine ialina maggiormente rispetto a quella calcificata.

La camera di coltura è stata dimensionata per garantire un'adeguata diffusione di nutrienti e specie chimiche nei costrutti, e per ottenere il livello desiderato di compressione sovrafisiologica, posto pari al 30% in accordo con la letteratura [14]. Per i canali centrali sono state adottate larghezze di 300 e 500 µm; l'altezza delle micro-colonne e dello spazio vuoto sottostante è stata posta pari a 100 µm e 43 µm, rispettivamente, portando l'altezza totale della camera di coltura a 143 µm. Le micro-colonne sono state disegnate in modo da minimizzare l'espansione laterale dei costrutti durante la compressione, ridurre la probabilità di perdite durante l'iniezione degli idrogeli (in accordo con un modello di *capillary burst valve* modificata [15]) e fornire un'area di contatto sufficiente tra i costrutti e il mezzo di coltura.

Dei modelli agli elementi finiti sono stati implementati per valutare il campo di deformazione all'interno dei costrutti cellulari nelle diverse versioni del dispositivo. Il PDMS è stato descritto come un materiale iperelastico alla Mooney-Rivlin, mentre per gli idrogeli è stato adottato un modello bifasico poroelastico. Tale modello è stato usato sia per il costrutto di cartilagine ialina, sia per quello di cartilagine calcificata, cambiando solo il modulo elastico: nel primo caso è stato adottato un valore di 100 kPa, nel secondo caso un valore di 200 kPa.

SOMMARIO

I dispositivi sono stati fabbricati tramite tecniche di soft-litografia. Le caratteristiche geometriche sono state tradotte in maschere. Sono state prodotte due maschere per la camera di coltura (una per le micro-colonne e una per lo spazio vuoto sottostante) e una per la membrana di attuazione. Per il pavimento del dispositivo non è stata necessaria alcuna maschera, essendo la sua superficie priva di rilievi geometrici. La geometria delle maschere è stata trasferita tramite fotolitografia su due wafer di silicio, che sono stati poi utilizzati come stampi per la produzione degli strati del dispositivo. Le camere di coltura e di attuazione sono state ottenute versando PDMS liquido nei rispettivi stampi, mentre per realizzare il pavimento il PDMS è stato versato in una piastra di Petri. Il polimero è stato lasciato a 65°C per due ore e mezza su un piano livellato, per consentirne la reticolazione. Gli strati ottenuti sono stati sigillati mediante trattamento al plasma.

La geometria dei dispositivi è stata caratterizzata, verificando l'accuratezza del processo di fabbricazione. Sono state ottenute delle sezioni sottili della camera di coltura. L'altezza delle micro-colonne e dello spazio vuoto sottostante è stata misurata e utilizzata per calcolare il livello di compressione prodotto dai dispositivi. È stata inoltre effettuata una valutazione sperimentale della pressione di attuazione necessaria a un corretto funzionamento dei dispositivi.

I dispositivi microfluidici sono poi stati utilizzati per generare un modello cellulare di OA. La validazione biologica è stata articolata in più fasi: inizialmente, sono stati ottimizzati i parametri di coltura necessari allo sviluppo di costrutti di cartilagine calcificata a partire da MSCs in monocoltura, e all'induzione di tratti di OA in tali costrutti; in secondo luogo, è stata valutata la maturazione di costrutti osteocondrali bicompartimentali, composti da cartilagine ialina e cartilagine calcificata; infine, è stata valutata l'induzione di tratti di OA in tali costrutti tramite una compressione ciclica sovrafisiologica.

Per generare i costrutti osteocondrali, degli idrogeli a base di glicole polietilenico (PEG) al 2%, enzimaticamente reticolabili e degradabili [16], sono stati seminati con MSCs e HACs e iniettati nei dispositivi. Sono state effettuate due settimane di condizionamento con 10 ng/ml di fattore di crescita trasformante (TGF)-β3, Dexametasone 10^{-7} M, β-Glicerofosfato 10 mM e acido ascorbico 0.1 mM in condizioni statiche. La maturazione dei tessuti e la deposizione di ECM sono state analizzate tramite microscopia a contrasto di fase e immunofluorescenza. I costrutti sono stati marcati per i nuclei cellulari, l'idrossiapatite, l'aggrecano e il collagene di tipo II, ai giorni 0, 7 e 14 della coltura. La

quantitative reverse transcription-polymerase chain reaction (RT-qPCR) è stata utilizzata per studiare la maturazione dei tessuti a livello genetico. I costrutti sono stati sottoposti a digestione enzimatica e *cell sorting* prima della RT-qPCR, per separare HACs e condrociti ipertrofici derivati dalle MSCs. Per questa ragione, i costrutti da analizzare tramite RT-qPCR sono stati generati con condrociti modificati per esprimere la *green fluorescent protein* (GFP). L'espressione di geni associati a condrogenesi (ACAN), ipertrofia (COL10A1), mineralizzazione (ALPL), e ossificazione (IBSP) è stata analizzata al giorno 0 e al giorno 14.

Per valutare l'effetto della compressione sovrafisiologica sui costrutti, MSCs e HACs modificati per esprimere la GFP sono stati coltivati staticamente per due settimane nei dispositivi, mentre dal giorno 14 al giorno 21 è stata applicata la stimolazione meccanica. Al giorno 21, le cellule sono state separate sulla base dell'espressione della GFP, e la loro espressione genica è stata analizzata tramite RT-qPCR. I costrutti sottoposti a stimolazione meccanica sono stati confrontati con i controlli statici. L'acquisizione di tratti OA in seguito alla compressione sovrafisiologica è stata valutata analizzando geni associati all'inibizione dell'ipertrofia (FRZB), all'infiammazione (CXCL8), al catabolismo (MMP13), alla mineralizzazione (ALPL) e all'ossificazione (BGLAP).

RISULTATI

I modelli agli elementi finiti del dispositivo hanno fornito una valutazione dello stato di deformazione nei costrutti cellulari durante la compressione, sia nella configurazione simmetrica del dispositivo, sia in quella asimmetrica. La Fig. 2 mostra una rappresentazione della deformazione in direzione verticale nelle due configurazioni.
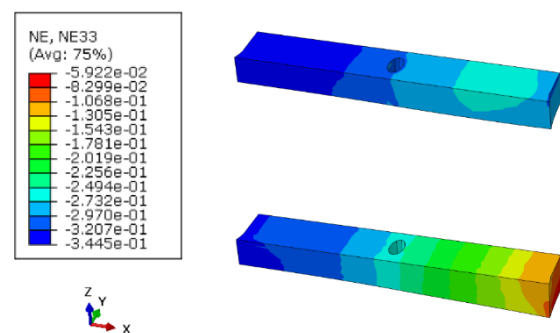
Fig. 2: *mappa dello stato di deformazione in direzione verticale nei costrutti, nella configurazione simmetrica (A) e asimmetrica (B) del dispositivo. La cartilagine calcificata è a destra, quella ialina a sinistra.*

Nella configurazione simmetrica, la deformazione nominale in direzione verticale (NE33) e la deformazione laterale (NE11) sono risultate pari a -31.3% ± 1.5% e -0.8% ± 2.0% nella cartilagine ialina e -27.5% ± 1.6% e 1.7% ± 2.4% nella cartilagine calcificata, rispettivamente (mediana ± scarto interquartile, IQR). Nella configurazione asimmetrica, NE33 e NE11 sono risultate pari a 30.2% ± 4.6% e 0.4% ± 3.6% nella cartilagine ialina e -17.4% ± 12.0% e 0.1% ± 7.4% in quella calcificata, rispettivamente. La deformazione in direzione longitudinale (NE22) è risultata trascurabile in entrambe le configurazioni.

SOMMARIO

La caratterizzazione geometrica dei dispositivi ha dimostrato l'accuratezza del processo di fabbricazione. I livelli di compressione ottenuti in tutte le versioni del dispositivo sono risultati in linea con il valore desiderato del 30%. L'ottimizzazione della pressione di attuazione ha prodotto un valore finale di 400 millibar, che è stato adottato per gli esperimenti biologici seguenti.

Una volta terminata la caratterizzazione dei dispositivi, questi sono stati utilizzati per generare un modello cellulare di OA. I parametri di coltura per ottenere costrutti di cartilagine ialina erano noti [17], mentre le informazioni sulla differenziazione delle MSCs in condrociti ipertrofici e sulla loro risposta a stimoli meccanici deleteri erano scarse. È stata quindi effettuata un'indagine preliminare su questi argomenti, necessaria per sviluppare il modello osteocondrale di OA più complesso.

Dopo due settimane di coltura statica è stato possibile ottenere dei costrutti maturi di cartilagine calcificata. L'espressione di geni associati a condrogenesi (ACAN e COL2A1), ipertrofia (COL10A1 e IHH), mineralizzazione (ALPL) e ossificazione (IBSP) è aumentata. Inoltre, la marcatura con Calceina ha rivelato la deposizione di una matrice mineralizzata.

La compressione sovrafisiologica dei costrutti ha indotto una riduzione di 5.5 volte dell'espressione dell'inibitore di ipertrofia

FRZB, un aumento di 2.8 volte di BGLAP, gene associato all'ossificazione, e una riduzione di 3.7 volte del fattore anti-angiogenico LECT1.
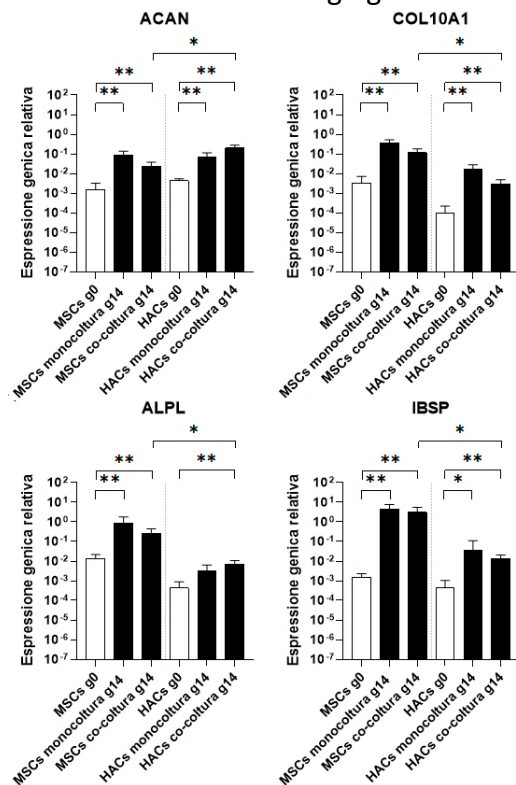
Fig. 3: espressione genica nei costrutti osteocondrali al giorno 0 e 14. Sono riportate media e deviazione standard (SD). La significatività è stata determinata tramite test di Mann-Whitney. * $p < 0.05$, ** $p < 0.01$.

Successivamente, è stata valutata la maturazione di costrutti osteocondrali bicompartimentali. Dopo 14 giorni di coltura statica, HACs e condrociti ipertrofici derivati da MSCs sono risultati in grado di mantenere i loro rispettivi profili genici. La RT-qPCR ha mostrato un'espressione di ACAN 8.4 volte maggiore nella cartilagine ialina rispetto a quella calcificata al giorno 14. L'espressione di COL10A1 è risultata significativamente minore (di 39 volte) nella cartilagine ialina rispetto a quella calcificata. L'espressione di ALPL e IBSP è risultata rispettivamente 35 e 215 volte

maggiore nella cartilagine calcificata rispetto a quella ialina. Per tutti i geni, in entrambi i compartimenti l'espressione al giorno 14 è risultata significativamente maggiore rispetto al giorno 0 (Fig. 3).
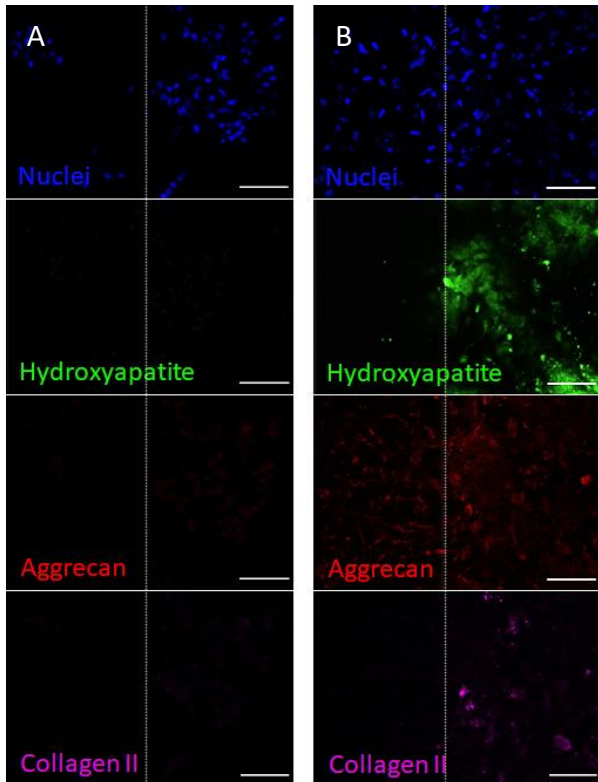
Fig. 4: immunofluorescenza dei costrutti osteocondrali al giorno 0 (A) e 14 (B). Le linee tratteggiate indicano l'interfaccia tra la cartilagine ialina (a sinistra) e la cartilagine calcificata (a destra). La barra rappresenta 100 µm.

Il mantenimento di profili di differenziazione distinti è stato confermato da analisi dell'ECM. L'immunofluorescenza ha rivelato la deposizione di una matrice mineralizzata nella cartilagine calcificata, ma non nella cartilagine ialina. L'aggrecano è stato osservato in entrambi i compartimenti, suggerendo lo sviluppo di tessuti cartilaginei. Il collagene di tipo II, altra proteina tipica della cartilagine, è stato invece osservato solo nella cartilagine calcificata (Fig. 4).

In seguito, è stato valutato l'effetto della compressione sovrafisiologica, simmetrica o asimmetrica, sui costrutti osteocondrali.
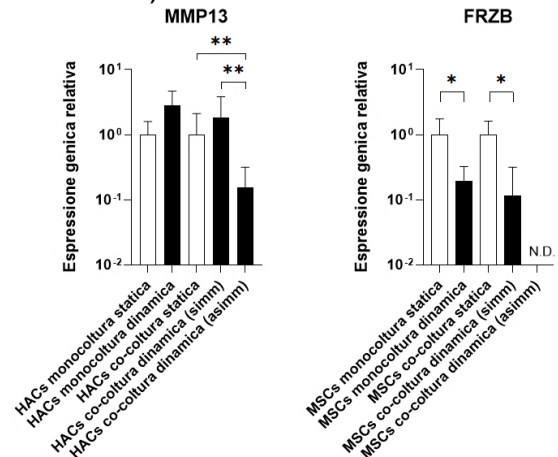
*Fig. 5: espressione di geni rilevanti nei costrutti osteocondrali sottoposti a compressione sovrafisiologica. Sono riportate media e SD. La significatività è stata determinata tramite test di Mann-Whitney. * p < 0.05, ** p < 0.01.*

Nella cartilagine ialina, la compressione sovrafisiologica ha indotto un aumento di 1.8 volte dell'espressione di MMP13 nella configurazione simmetrica del dispositivo, e una riduzione di 6.4 volte in quella asimmetrica. La CXCL8 è risultata maggiormente espressa nei costrutti stimolati rispetto ai controlli statici, di 2.4 volte e 1.2 volte nella configurazione simmetrica e asimmetrica, rispettivamente. L'espressione di FRZB è risultata minore nei costrutti stimolati rispetto a quelli non stimolati, di 1.3 volte e 2.1 volte per le due configurazioni, rispettivamente. Nella cartilagine calcificata, la compressione ha determinato un aumento dell'espressione di BGLAP (di 1.2 volte nella configurazione simmetrica e 1.4 volte in quella asimmetrica), e una diminuzione

dell'espressione di ALPL (rispettivamente di 2.1 volte e 1.8 volte), rispetto ai controlli statici. Nella configurazione simmetrica è stata osservata una riduzione di 5.2 volte dell'espressione di FRZB, mentre non è stato possibile analizzare questo gene nella configurazione asimmetrica, a causa del poco materiale genetico disponibile dopo la digestione enzimatica e il *cell sorting* (Fig. 5).

DISCUSSIONE

Nel presente lavoro è stato sviluppato un dispositivo microfluidico per la co-coltura e la stimolazione meccanica di due costrutti cellulari 3D con un'interfaccia diretta.

Le analisi computazionali hanno mostrato la capacità del dispositivo di produrre una compressione confinata dei costrutti. Globalmente, il campo di deformazione calcolato per la configurazione simmetrica del dispositivo è risultato in linea con i requisiti di progetto, mentre per la configurazione asimmetrica sono state riscontrate alcune discrepanze. In particolare, la deformazione della cartilagine ialina è risultata disomogenea, e la deformazione della cartilagine calcificata è risultata sensibilmente diversa da quella desiderata. Tuttavia, la deformazione prodotta è stata comunque ritenuta un compromesso accettabile tra le condizioni ottimali necessarie per i due tessuti, e la

configurazione asimmetrica è stata utilizzata senza ulteriori modifiche.

I dispositivi sono stati poi utilizzati per generare un modello cellulare meccanicamente attivo e multi-tessuto di OA, in grado di rappresentare due dei tessuti più affetti da questa patologia, ovvero cartilagine ialina e cartilagine calcificata.

Gli esperimenti biologici preliminari hanno permesso di ottimizzare le condizioni di coltura per generare costrutti di cartilagine calcificata da MSCs, servendo da punto di partenza per il modello osteocondrale più complesso. Inoltre, l'applicazione di una compressione sovrafisiologica ciclica sui costrutti ha permesso di replicare alcuni tratti distintivi della zona della cartilagine calcificata in un'articolazione nativa affetta da OA, come un elevato grado di ipertrofia, una predisposizione alla vascolarizzazione e lo sviluppo di regioni di ossificazione [5].

Una volta completati gli esperimenti preliminari, i dispositivi sono stati sfruttati per generare dei costrutti osteocondrali bicompartimentali. Dopo due settimane di coltura statica, sono stati ottenuti dei tessuti cartilaginei con due compartimenti distinti, uno mineralizzato e uno non mineralizzato.

Infine, i dispositivi hanno permesso di esporre i costrutti a una compressione sovrafisiologica ciclica, ricreando la condizione di sovraccarico meccanico tipica

dell'OA *in vivo*. Mentre la configurazione asimmetrica del dispositivo ha prodotto risultati contradditori, quella simmetrica ha permesso di replicare alcuni tratti distintivi dell'OA, tra cui ipertrofia, aumento del catabolismo e infiammazione nella cartilagine ialina, nonché predisposizione alla vascolarizzazione e sviluppo di regioni di ossificazione nella cartilagine calcificata. Ulteriori studi con un numero più elevato di donatori cellulari sono necessari per giungere a conclusioni più affidabili.

CONCLUSIONI E SVILUPPI FUTURI

Un dispositivo microfluidico meccanicamente attivo in PDMS è stato disegnato, fabbricato e impiegato con successo per generare costrutti osteocondrali 3D multi-tessuto, consistenti in idrogeli a base di PEG seminati con HACs o MSCs. Il dispositivo ha garantito un'adeguata diffusione di nutrienti e fattori di differenziazione nei tessuti ed è risultato compatibile con la coltura cellulare di medio-lungo termine. Inoltre, ha permesso di fornire ai costrutti degli stimoli meccanici definiti, ricreando la condizione di sovraccarico meccanico tipica delle articolazioni native affette da OA. Una ripetizione degli esperimenti svolti, considerando un numero maggiore di donatori cellulari, sarà necessaria per confermare i risultati biologici ottenuti.

Dopo una validazione più esaustiva, il modello sviluppato potrebbe essere utilizzato per testare nuove possibili terapie anti-OA, mirate ad aspetti della patologia non ricapitolati dai modelli precedenti (ad esempio la formazione di regioni di ossificazione negli strati più profondi della cartilagine). L'introduzione nel modello di ulteriori tessuti coinvolti nell'OA, come la rete vascolare, consentirebbe una maggiore comprensione della patologia. L'aggiunta di nuovi tipi cellulari, tuttavia, renderebbe necessario l'uso di mezzi di coltura diversi per i diversi tessuti considerati. Ciò potrebbe essere reso possibile integrando il dispositivo sviluppato nel presente lavoro con un sistema di perfusione in grado di generare un flusso continuo di mezzo di coltura nei canali laterali del dispositivo, e un gradiente biochimico stabile tra i due compartimenti. Infine, si potrebbero apportare delle modifiche al design del dispositivo, per ottenere un campo di deformazione più simile a quello presente nell'articolazione nativa, in cui i due tessuti sono sovrapposti e non affiancati.

Globalmente, la realizzazione di un dispositivo microfluidico con queste caratteristiche rappresenterebbe un passo ulteriore verso lo sviluppo di un modello di articolazione su chip, in grado di ricapitolare pienamente *in vitro* la complessità dell'OA.

BIBLIOGRAFIA

[1] S. Glyn-Jones et al., "Osteoarthritis," Lancet, vol. 386, no. 9991, pp. 376–387, 2015, doi: 10.1016/S0140-6736(14)60802-3.

[2] L. March, M. Cross, N. Arden, and G. Hawker, "Osteoarthritis: A Serious Disease, Submitted to the U. S. Food and Drug Administration," Oarsi, pp. 1–103, 2016.

[3] M. Kloppenburg and F. Berenbaum, "Osteoarthritis year in review 2019: epidemiology and therapy," Osteoarthr. Cartil., vol. 28, no. 3, pp. 242–248, 2020, doi: 10.1016/j.joca.2020.01.002.

[4] S. Grässel and D. Muschter, "Recent advances in the treatment of osteoarthritis," F1000Research, vol. 9, no. May, 2020, doi: 10.12688/f1000research.22115.1.

[5] S. R. Goldring and M. B. Goldring, "Changes in the osteochondral unit during osteoarthritis: Structure, function and cartilage bone crosstalk," Nat. Rev. Rheumatol., vol. 12, no. 11, pp. 632–644, 2016, doi: 10.1038/nrrheum.2016.148.

[6] S. Suri and D. A. Walsh, "Osteochondral alterations in osteoarthritis," Bone, vol. 51, no. 2, pp. 204–211, 2012, doi: 10.1016/j.bone.2011.10.010.

[7] G. Li et al., "Subchondral bone in osteoarthritis: Insight into risk factors and microstructural changes," Arthritis Res. Ther., vol. 15, no. 6, 2013, doi: 10.1186/ar4405.

[8] M. J. Benito, D. J. Veale, O. FitzGerald, W. B. Van Den Berg, and B. Bresnihan, "Synovial tissue inflammation in early and late osteoarthritis," Ann. Rheum. Dis., vol. 64, no. 9, pp. 1263–1267, 2005, doi: 10.1136/ard.2004.025270.

[9] P. J. Cope, K. Ourradi, Y. Li, and M. Sharif, "Models of osteoarthritis: the good, the bad and the promising," Osteoarthr. Cartil., vol. 27, no. 2, pp. 230–239, 2019, doi: 10.1016/j.joca.2018.09.016.

[10] C. I. Johnson, D. J. Argyle, and D. N. Clements, "In vitro models for the study of osteoarthritis," Vet. J., vol. 209, pp. 40–49, 2016, doi: 10.1016/j.tvjl.2015.07.011.

[11] C. Probst, S. Schneider, and P. Loskill, "High-throughput organ-on-a-chip systems: Current status and remaining challenges," Curr. Opin. Biomed. Eng., vol. 6, pp. 33–41, 2018, doi: https://doi.org/10.1016/j.cobme.2018.02.004.

[12] D. Huh, G. A. Hamilton, and D. E. Ingber, "From 3D cell culture to organs-on-chips," Trends Cell Biol., vol. 21, no. 12, pp. 745–754, 2011, doi: 10.1016/j.tcb.2011.09.005.

[13] S. K. Sia and G. M. Whitesides, "Microfluidic devices fabricated in poly(dimethylsiloxane) for biological studies," Electrophoresis, vol. 24, no. 21, pp. 3563–3576, 2003, doi: 10.1002/elps.200305584.

[14] P. Occhetta et al., "Hyperphysiological compression of articular cartilage induces an osteoarthritic phenotype in a cartilage-on-a-chip model," Nat. Biomed. Eng., vol. 3, no. 7, pp. 545–557, 2019, doi:10.1038/s41551-019-0406-3.

[15] C. P. Huang et al., "Engineering microscale cellular niches for three-dimensional multicellular co-cultures," Lab Chip, vol. 9, no. 12, pp. 1740–1748, 2009, doi: 10.1038/jid.2014.371.

[16] M. Ehrbar et al., "Biomolecular hydrogels formed and degraded via site-specific enzymatic reactions," Biomacromolecules, vol. 8, no. 10, pp. 3000–3007, 2007, doi: 10.1021/bm070228f.

[17] A. Mainardi, "Towards the knee on a chip: development of a microfluidic platform for the mechanical stimulation of three dimensional cartilaginous constructs," 2016.

1 INTRODUCTION

1.1 Osteoarthritis

Osteoarthritis (OA) is a degenerative joint disease, and a major source of pain, disability and socioeconomic cost worldwide [1]. OA affects all joints, but preferentially hands and weight-bearing articulations such as knees, hips, and spine [2]. The main symptoms are pain and stiffness, accompanied in many cases by a reduced range of motion or by a complete articulation loss of function [3].

OA is the most common musculoskeletal disorder in the world. In 2017, more than 303 million people were estimated to suffer from it [4]. Different studies report various values of its incidence and prevalence, depending on the definition of the pathology, the joint under study and the considered population. For instance, the Zoetermeer study [5], performed in 1989 on a pool of 6568 subjects, reported that 11.2% of men and 16.1% of women aged 50-54 suffered from knee OA. The prevalence increased respectively to 24.7% and 40.2% for men and women aged 70-74. More recently, the European Project on Osteoarthritis analysed the burden of OA among European countries [6]. The study found out that 31.7% of subjects aged over 65 showed clinical evidence of OA at least at one site of the body, and 20.2% were affected by knee OA. These data are likely to increase in the next future, given the constant increase in life expectancy.

The high values of incidence and prevalence of OA come with serious consequences from the economical point of view: OA-related costs amount to 1 − 2.5% of the gross domestic product of developed countries [7], considering both direct (i.e., medical expenses), and indirect costs (e.g., lost earnings and job-related costs such as loss of productivity due to disability). In fact, OA accounts for 2.4% of all years lived with disability (YLD) worldwide, and it is associated with early retirement and forced unemployment [4].

Disability and reduced physical activity associated with OA can also increase the risk of comorbidities: a recent systematic review [8] found that people living with OA had an overall pooled prevalence for cardiovascular disease of 38.4%, compared to that of 9% of non-OA controls. Subjects with OA were almost three times more likely to have heart failure and two times more likely to have ischemic heart disease as compared to matched non–OA cohorts. As a consequence, OA is also indirectly associated with increased premature mortality, mostly due to cardiovascular comorbidities. For these reasons, in 2016 the Osteoarthritis Research Society International

INTRODUCTION

submitted a White Paper to the FDA, describing OA as a serious disease and a major worldwide challenge for health systems in the 21st century [4].

Based on its aetiology, OA can be classified as primary (idiopathic) or secondary [9]. Secondary OA has no specific joints of occurrence, and it is caused by specific disorders which can be divided into four categories: metabolic (e.g., haemochromatosis), anatomic (e.g., epiphyseal dysplasia, slipped femoral epiphysis, leg length inequality), traumatic (e.g., fracture through a joint, joint surgery) and inflammatory (e.g., septic arthritis). Primary OA, on the other hand, mostly affects hands, knees, and hips, and has no specific evidenced causes, although some factors have been proven to play a substantial role in its development [9]. An enumeration of the factors correlated with primary OA is presented below.

Among the systemic risk factors, the most widely recognized is age [1]–[10]. The causal connection between age and OA development is probably mediated by age-related biomechanical risk factors, such as excessive joint loading due to impaired neuromuscular joint protective mechanisms and increased joint instability (e.g., ligamentous laxity) [11]. The resilience and the reparative capacity of cartilage may also decrease with age, making joints more vulnerable to the effects of biomechanical insults [9]. Another systemic risk factor is gender. Most studies show that the occurrence of knee, hip, hand and generalized (i.e., affecting multiple joints) OA is higher in women than in men, in particular after the age of 50. Postmenopausal sex hormones alterations, and specifically oestrogen deficiency, may play a role in the systemic predisposition to OA. Some studies found a lower occurrence of OA in postmenopausal women using oestrogen [12], [13]. However, the protective effect of this hormone is still controversial. Another well-established risk factor for OA is obesity. An excessive Body Mass Index (BMI) determines the overloading of weight-bearing joints such as knee and hip, causing breakdown of cartilage and damage to ligaments and other support structures. This, in turn, can increase the risk of subsequent OA development or worsen the progression of pre-existing OA [14], [15]. Obese (BMI > 30) and overweight (BMI = 25.5 – 30) subjects were shown to be 9.3 and 3.8 times more likely to develop knee OA as compared to normal weight subjects, respectively [14]. Hip OA was also positively associated with obesity, although less strongly than knee OA. Some studies even found a higher risk of hand OA in obese subjects [14], [16], suggesting that adiposity-related metabolic factors (such as circulating adipocytokines, chronic inflammation and high levels of blood glucose) may also play a role in the development of the pathology. Other risk factors correlated with OA include high bone mineral density, gene mutations and poor nutrition [9].

1.1.1 Tissue alterations

Until the 1980s, OA was considered as a mere result of wear and tear of the articular surfaces [17]. Nowadays, however, it is widely acknowledged as a complex condition affecting various tissues of the joint, namely hyaline cartilage, calcified cartilage, subchondral bone, and synovium:

- Hyaline cartilage: in normal articular cartilage there is a delicate balance between matrix synthesis and degradation. In OA, this balance is disturbed, with both degradation and synthesis enhanced. An enhanced inflammatory microenvironment, characterized by cytokines such as interleukin-1 (IL-1), tumour necrosis factor alpha (TNF-α), IL-17, and IL-18, causes, in turn, an increase in the synthesis of catabolic enzymes such as matrix metalloproteinases (MMPs), a decrease in MMP enzyme inhibitors, and a diminished extracellular matrix (ECM) synthesis [18]. The cytokine-induced proteolytic enzyme release is mediated by nitric oxide (NO), prostaglandin E2 (PGE2) and reactive oxygen species [19]. On the other hand, the anabolic cytokines insulin-like growth factor 1 (IGF-1), transforming growth factors beta (e.g., TGF-β1, TGF- β2, and TGF- β3), fibroblast growth factors (e.g., FGF-2, FGF-4, and FGF-8), and bone morphogenetic proteins (BMPs) act to stimulate ECM production [18]. Overall, a net loss of proteoglycans (PG) and collagen type II occurs in all stages of OA. PG degradation is mediated by aggrecanases of the ADAMTS (A Disintegrin and Metalloproteinase with Thrombospondin motifs) family, while the collagen network can be disrupted either by physical forces or by the increased activity of MMPs [20]. A study on OA patients undergoing total knee replacement found an increased expression of the non-chondrogenic genes COL1A1 (encoding for Collagen type I alpha 1 chain), COMP (encoding for Cartilage Oligomeric Matrix Protein) and FN1 (encoding for Fibronectin) in damaged cartilage, and a downregulation of the chondrogenic genes SOX9 (SRY-Box Transcription Factor 9), SOX6 (SRY-Box Transcription Factor 6), COL11A2 (Collagen type XI alpha 2 chain), COL9A1/2/3 (Collagen type IX alpha 1, 2 and 3 chains), ACAN (Aggrecan) and HAPLN1 (Hyaluronan And Proteoglycan Link Protein 1) [21]. The synthesis of non-chondrogenic proteins, together with the enhanced catabolic activity, determines deep changes in the composition of osteoarthritic cartilage matrix.

  Another feature of OA is chondrocyte hypertrophy [20]. Hypertrophic chondrocytes are terminally differentiated cartilage cells characterised by an increase in cell volume and by the expression of collagen type X and vascular endothelial growth factor (VEGF). They normally populate the zone of calcified cartilage (ZCC), at the interface between hyaline

cartilage and bone. However, during OA, chondrocytes in the articular cartilage may also assume an hypertrophic phenotype [20].

Non-calcified hyaline articular cartilage in healthy adults is normally avascular and aneural. Normal chondrocytes express antiangiogenic factors such as chondromodulin-1 [22] and thrombospondin-1 [23]. Furthermore, proteoglycans and glycosaminoglycans (GAGs) present in cartilage matrix form a barrier against vascular invasion. This barrier may be reduced in OA, due to changes in matrix composition such as loss of GAG and PG [24]. Meanwhile, hypertrophic chondrocytes release VEGF, which facilitates angiogenesis [20]. As a consequence, osteoarthritic cartilage loses its ability to remain avascular, and blood vessels invade it from the underlying ZCC. Furthermore, vascularisation is accompanied by the growth of sensory and sympathetic nerves, resulting in a potential source of pain for subjects affected by OA. The perivascular localisation of nerves implies that angiogenesis drives or guides the innervation of hyaline cartilage. Indeed, nerve growth factor (NGF) expression has been found in blood vessels invading cartilage [25].

From a histological point of view, OA is associated with a number of tissue alterations, which involve increasingly deeper layers of articular cartilage as the pathology becomes more severe [17]. Healthy hyaline cartilage shows a smooth articular surface (Fig. 1.1.1 A). In early OA, the articular surface may present mild abrasion, called fibrillation, characterized by microscopic cracks (Fig. 1.1.1 B). In late OA, these cracks extend into the mid zone of articular cartilage, forming vertical fissures (Fig. 1.1.1 C). Finally, delamination of the superficial layer and extensive erosion in fissured domains can be observed in advanced OA (Fig. 1.1.1 D).
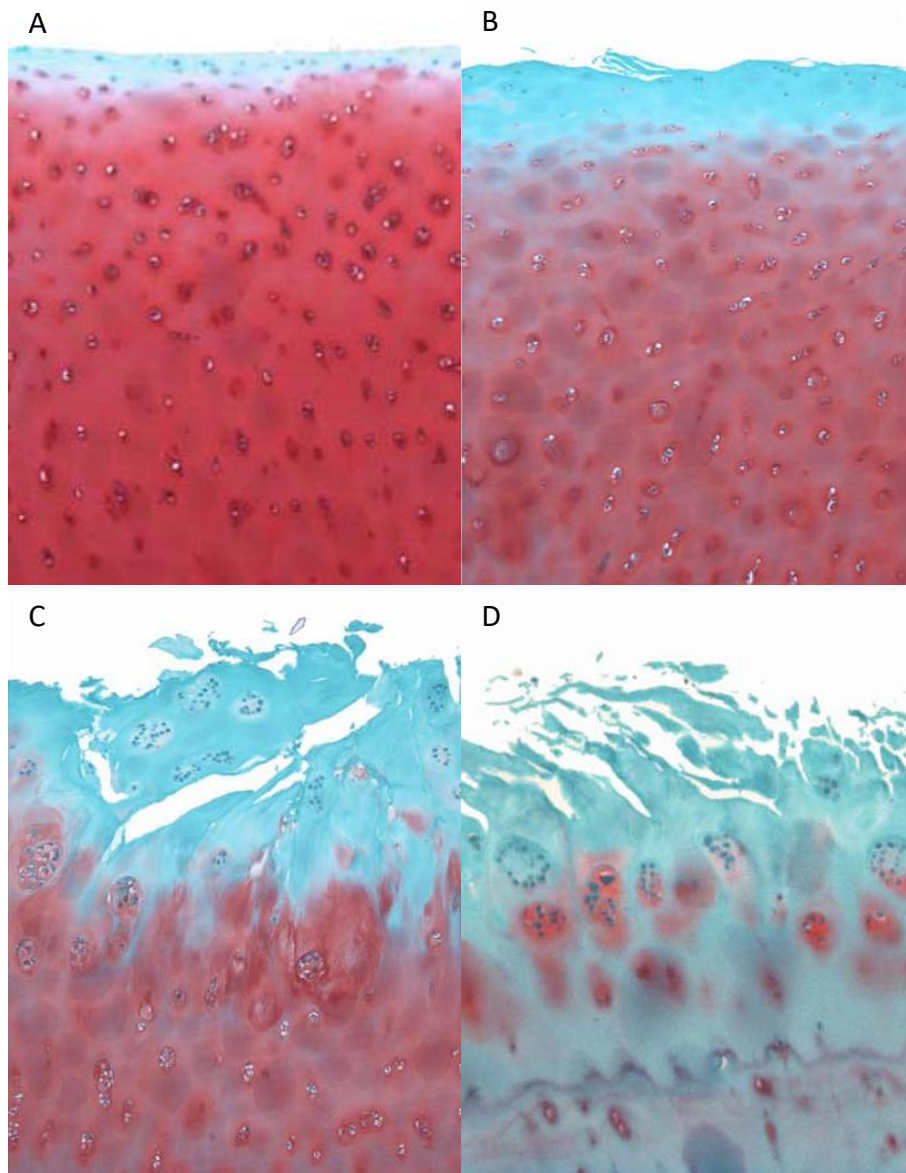
Fig. 1.1.1: Safranin O staining of cartilage samples at various stages of OA, original magnification 5x [17]. A) healthy hyaline cartilage (grade 0); B) grade 1 OA cartilage; C) grade 3 OA cartilage; D) grade 4 OA cartilage.

- Calcified cartilage: the ZCC is separated from the overlying hyaline cartilage by the so-called tidemark, a dark line appearing in Safranin O stainings and resulting from the accumulation of large molecules produced by apoptotic chondrocytes [26]. One of the hallmarks of OA is the duplication of the tidemark (Fig. 1.1.2), with the subsequent advancement of the calcified cartilage into the articular cartilage [20], thinning of the hyaline cartilage layer, and impaired mechanical load distribution. This process is initiated by the penetration of the calcified cartilage by vascular elements in correspondence of microcracks and fissures at the interface with the subchondral bone. Regions of new bone formation develop in cuffs around the newly formed vessels. Cells in the osteoarthritic ZCC undergo changes in the expression

of genes responsible for maintaining cartilage/bone differentiation. In particular, transcription factors essential for cartilage formation, such as SOX9, were reported to be downregulated, while transforming growth factor alpha (TGF-α), which inhibits the anabolic capacity of chondrocytes, was reported to be upregulated [27].
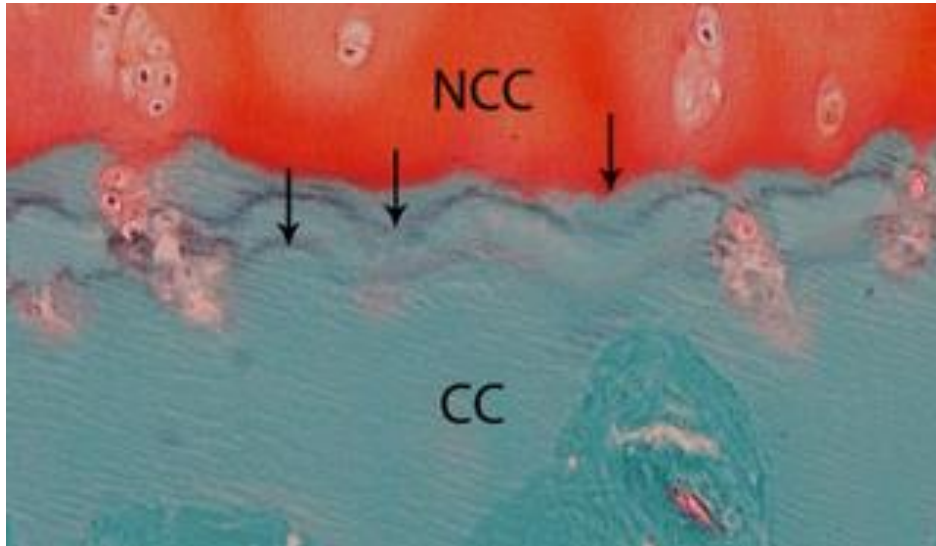
Fig. 1.1.2: interface between non-calcified cartilage (NCC) and calcified cartilage (CC) in an osteoarthritic joint. The arrows indicate the multiple tidemarks [28].

- Subchondral bone: subchondral sclerosis, i.e., an abnormal increase in the volumetric density of subchondral bone, is commonly considered as an indisputable sign of OA [28]. However, this increased density does not result in higher mechanical properties: the deposited matrix is hypomineralized, determining a reduced bone stiffness [28]. Another hallmark of OA is the formation of bony outgrowths, known as osteophytes, at the joint margins [20]. Osteophyte growth involves a program of endochondral bone formation that is initiated by the proliferation of periosteal cells at the joint margin, followed by the infiltration and differentiation of hypertrophic chondrocytes. However, some studies suggest that osteophytes might serve to stabilize the joint, rather than contribute to joint dysfunction and OA progression [29]. Additional OA-related changes include an increased cortical plate thickness, the formation of bone cysts, and the development of bone marrow oedema-like lesions, strongly correlated with joint pain [20].

- Synovium: the synovium is a specialized connective tissue lining diarthrodial joints [30]. In OA, the synovium undergoes hyperplasia, sub-lining fibrosis, and stromal vascularization [30], [31]. Synovial inflammation is another hallmark of this pathology. Synovial tissue from OA patients is characterized by an increased infiltration of mononuclear cells (T lymphocytes and macrophages) and an increased production of proinflammatory cytokines and mediators of joint damage, such as TNF-α and IL-1β [31]. Moreover, the number of cells

producing TNF-α and IL-1β was found to be significantly greater in early OA, as compared to late OA [31].

1.1.2 Conventional therapy

There are three main therapeutic approaches available for the treatment of osteoarthritis: lifestyle modification, pharmacological treatment, and surgical intervention [1]. However, all of them are finalized to alleviate symptoms (namely joint pain and stiffness) and to improve the patients' quality of life, while there are no currently available effective disease-modifying therapies able to reverse the degenerative process [2].

Lifestyle changes include physical exercise, weight loss for obese subjects, and measures to reduce the mechanical load borne by damaged joints. Radiographic structural modifications due to weight loss have not been shown, but benefits are evident in terms of changes in biochemical markers and pain perception. Physical activity, and in particular exercises focusing on increased muscle strength and aerobic capacity, improves OA symptoms and confers benefits in cardiovascular health, contributing to an overall mortality reduction [1].

Pharmacological treatments range from paracetamol, nonsteroidal anti-inflammatory drugs (NSAIDs), and corticosteroids, to weak opioids such as tramadol [2]. These drugs are prescribed for symptom alleviation, but do not show any disease-modifying effects. Paracetamol provides only minimal improvements in pain and function, but does not increase the risk of adverse events. NSAIDs are effective in the treatment of pain and inflammation, but are associated with gastric, renal, and cardiovascular adverse events. Intraarticular and intramuscular injections of corticosteroids are frequently prescribed to reduce joint pain and inflammation, but they are also associated with a wide range of side effects. Moreover, repeated intraarticular injections can determine cartilage loss and an overall worsening of OA. Finally, opioids are effective analgesics, but they may induce constipation, respiratory depression, drug tolerance and dependence, and their use is therefore limited. Huge efforts are currently being made in the development of new anti-OA drugs able to stop or reverse the degenerative process. The therapies under study include opioid receptor agonists, anti-NGF antibodies, anti-catabolic drugs and treatments targeting inflammatory mediators and pathways [32]. However, no pharmacological treatment was so far able to halt or reverse OA long-term progression.

Surgical treatment can be an effective option to prevent or reduce the progression of hip or knee OA. Some malformations, producing an impaired mechanical load distribution and favouring the development and the progression of OA, can be corrected by surgical interventions. In particular, the progression of OA secondary to hip dysplasia can be delayed by a reorientation of the acetabulum.

INTRODUCTION

Arthroscopic hip surgery to recontour the proximal femur and prevent femoroacetabular impingement has also shown symptomatic benefits. As for the knee, temporary surgical distraction, aimed at unloading the joint, has been proven to produce symptomatic and structural improvements in end-stage OA. Periarticular osteotomies to correct the mechanical axis of the knee are also promising. However, evidence for the effectiveness of these interventions is still limited, and further investigations with long-term follow-up are needed [1]. In case of end-stage OA, total joint replacement is also a valid option. However, it is associated with adverse events such as infection, stiffness, loss of function as a result of scar tissue, and increased post-operative mortality in patients with comorbidities [4]. Furthermore, prostheses have a limited life span, and younger patients undergoing joint replacement are likely to require revision surgery [2].

1.1.3 Regenerative approaches

Regenerative medicine is the branch of medicine that develops methods to regrow, repair or replace damaged tissues and organs [33]. Regenerative approaches therefore represent a promising solution for the future treatment of OA, possibly stopping the degenerative process or introducing viable substitutes for the damaged tissues.

Many attempts to develop regenerative approaches for the treatment of OA have been based on mesenchymal stem cells (MSCs), which display chondroprotective, anti-inflammatory and immunomodulatory effects. Autologous MSCs can be directly injected into the osteoarthritic joint through a minimally invasive procedure [32]; alternatively, MSCs secretome can be injected into the osteoarthritic joint or loaded into a surgically implantable scaffold [34]. However, the efficacy of these strategies is still unclear, and different studies report heterogeneous results [2].

Currently, there is doubt among surgeons and researchers about whether or not MSCs are really the optimal tool for the treatment of OA. Primary chondrocytes could represent an attractive alternative cell source for the repair of OA cartilage defects. The implantation of articular chondrocytes is an established approach, often adopted for the regeneration of traumatic lesions. Chondrocytes can be directly injected into the damaged site (through autologous chondrocyte implantation, ACI), or loaded onto a collagen membrane and surgically implanted (a procedure called matrix-induced autologous chondrocyte implantation, MACI) [35]. However, these procedures result in unpredictable and donor-dependent outcomes when applied for the treatment of degenerative diseases such as OA, probably due to the poor quality of the isolated cells [36]. The availability of intact articular cartilage in patients with OA is often very limited, and even chondrocytes harvested from intact articular cartilage have an inferior quality as compared to the

ones isolated from healthy donors [21]. Moreover, the harvesting of biopsies from articular cartilage would produce an additional injury in the already damaged joint site.

An alternative solution, preventing joint damage and allowing to obtain healthy cells, could be the isolation of chondrocytes from heterotopic compartments. Nasal chondrocytes (NCs), in particular, are very appealing, since they can be harvested with minimal donor site morbidity [37]. Moreover, NCs have shown an enhanced proliferation capacity and a higher and more reproducible chondrogenic capacity after *in vitro* expansion, as compared to articular chondrocytes [36], [37]. A recent study showed that grafts generated with autologous NCs were able to maintain a cartilaginous matrix after prolonged exposure to inflammatory cytokines, reduce the production of inflammatory and catabolic molecules by osteoarthritic cells, and preserve the cartilaginous features in an *in vivo* OA environment [36]. However, further investigations are needed to validate this approach: in particular, the capacity of NCs-derived grafts to bear the mechanical solicitations of an osteoarthritic joint should be assessed.

All these solutions, although promising, require a deeper understanding of the pathogenesis and the underlying mechanisms of OA. A model able to recapitulate the complexity of this pathology would therefore be very helpful for the development and the testing of new pharmacological or regenerative therapies.

1.2   Joint mechanical environment

The mechanical environment of the joint, i.e., the structure of the osteochondral unit, its mechanical properties, and the deformations it is subjected to, are fundamental aspects to be understood and replicated in the development of a proper OA model. A brief description of these aspects is proposed in the present chapter.

1.2.1 Structure and properties of the osteochondral unit
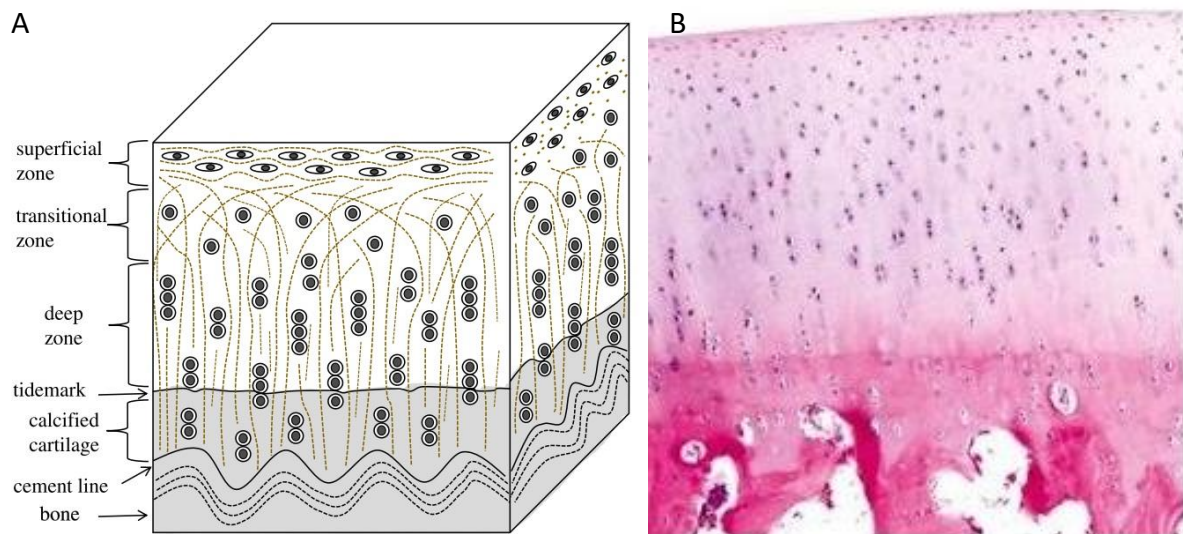
Fig. 1.2.1: A) schematization of the structure of the osteochondral unit [38]; B) haematoxylin and eosin staining of hyaline cartilage, calcified cartilage, and subchondral bone. Adapted from https://www.orthobullets.com/basic-science/9017/articular-cartilage.

The osteochondral unit is a complex structure including distinct functional elements, namely articular (hyaline) cartilage, calcified cartilage, and subchondral bone (Fig. 1.2.1).

Hyaline cartilage is an avascular and aneural tissue, with a high water content (>70%) and a low cellular density. Chondrocytes are the only cell type present in this tissue, and account for only 1–2% of its total volume. The major organic components of hyaline cartilage are collagen type II, which provides tensile strength, and aggrecan, which retains water within the tissue and provides compressive resilience [20]. Based on cell morphology and collagen network organization, hyaline cartilage can be divided into three zones: the superficial zone, where collagen fibrils are arranged predominantly with a direction parallel to the articular surface, and chondrocytes display a flattened morphology; the transitional zone, where chondrocytes appear spherical, and collagen fibrils have a random orientation; and the deep zone, where collagen fibrils are arranged perpendicular to the articular surface, and chondrocytes are aligned in columns [38]. The mechanical properties of cartilage are highly dependent on the organization of the collagen fibrils, with the Young modulus along the direction perpendicular to the articular surface varying from 0.25 MPa in the superficial zone to 0.5 MPa in the deep zone [39].

Hyaline cartilage lies on calcified cartilage, a thin tissue layer populated by hypertrophic chondrocytes expressing collagen type X [40]. Calcified cartilage transfers and distributes mechanical forces from hyaline cartilage to subchondral bone, attenuating the force gradient across

the joint [20], [40]. It has a Young modulus of approximately 0.32 GPa [41], intermediate between those of hyaline cartilage and subchondral bone. Calcified and non-calcified cartilage are separated by a histologically defined tidemark, resulting from the accumulation of large stainable molecules produced by apoptotic chondrocytes (see section 1.1.1). Undulations in the tidemark help transform shear stresses into compressive and tensile stresses during joint loading and motion, contributing to force distribution [20].

Subchondral bone, which is separated from calcified cartilage by the cement line, has a Young modulus of approximately 2.3 GPa [41]. It can be divided into two distinct anatomic entities: subchondral cortical plate and subchondral trabecular bone [28]. The cortical plate is a thin lamella, lying immediately beneath calcified cartilage. It is invaded by a high number of arterial and venous vessels, as well as nerves. The subchondral trabecular bone is more porous and metabolically active than the bone plate. It is a dynamic structure, able to adjust trabecular orientation and scale parameters in adaptation to the mechanical forces imposed across the joint.

1.2.2   Joint deformations

Knowledge of the *in vivo* deformational behaviour of joints is essential for the implementation of a load-based OA model. Joints can be subjected to a wide range of strains, depending on their location within the body and on the performed physical activity. Through magnetic resonance imaging (MRI) and 3D digital image analysis, Eckstein *et al.* [42] measured the *in vivo* deformation of patellar cartilage after different activities. The strain was -2.8% after walking, -5.0% after running, and approached -5.9% after knee bends. However, due to the depth-dependent mechanical properties of cartilage, strain was not homogeneous in the whole tissue. Zheng *et al.* [43] showed that an average deformation of -5% applied to articular cartilage explants produced a local strain of approximately -35% in the superficial zone, -5% in the transitional zone and -1% in the deep zone.

Chan *et al.* [44] introduced a non-invasive technique allowing the *in vivo* measurement of intra-tissue cartilage strain. The study considered nine volunteers with no medical history of cartilage or knee problems. MRI acquisitions were synchronized with physiologically relevant compressive loading (equal to half the body weight of each subject) and used to visualize and measure the regional displacement and strain of tibiofemoral articular cartilage (Fig. 1.2.2). The maximum compressive strain was found to be -9.7% and -7.6% in femoral and tibial cartilage, respectively, while shear strain reached 8.5% and 7.8%, respectively.
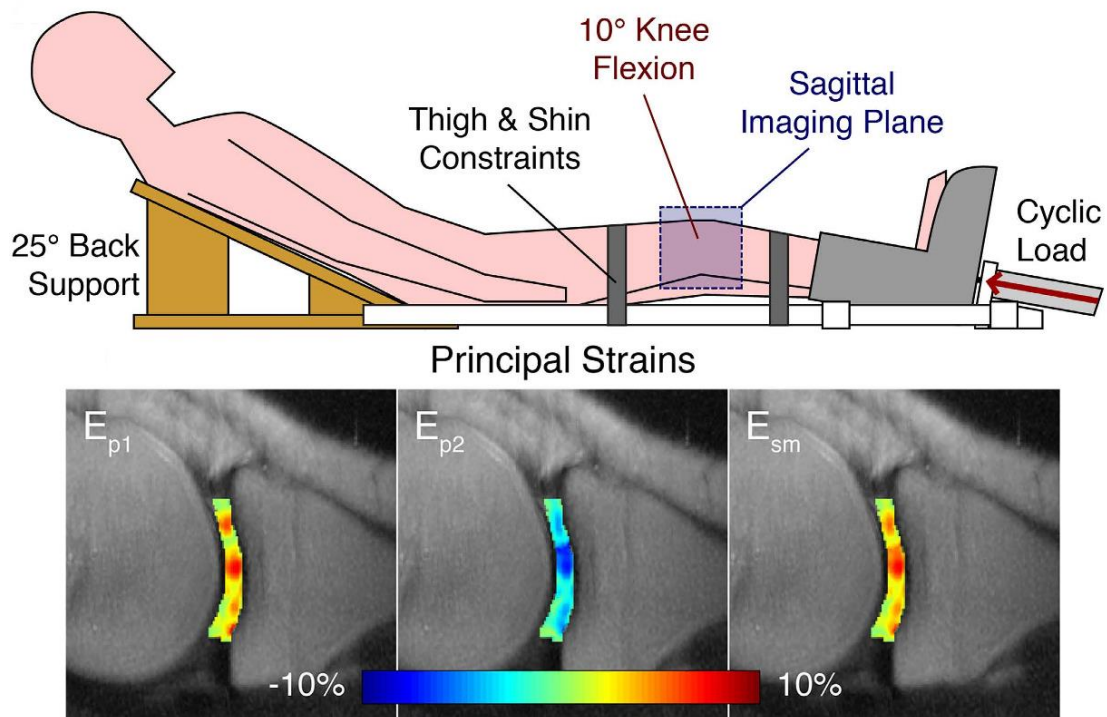
Fig. 1.2.2: top: setup of the experiment performed by Chan et al. *[44]; bottom: contour plot of the principal strains within tibiofemoral cartilage.*

1.2.3 Cartilage loading regime

Articular cartilage has a strain rate-dependent stiffness, as a consequence of the flow of interstitial fluid occurring upon loading and the viscoelasticity of the collagen fibril network [45]: if a compressive strain is applied at a low rate, the load is mostly borne directly by the solid constituents, with little contribution from the fluid; in contrast, in case of faster compression, the extra load is predominantly borne by the fluid, preventing cartilage from damage. However, if the compression is prolonged, the interstitial fluid flows out of the solid skeleton, and it is the fibril network to be progressively loaded.

Another phenomenon related to interstitial fluid flow is ratcheting: under cyclic compression, if the recovery time for cartilage rehydration is not allowed, a continuous strain accumulation can be produced [46]. This strain accumulation could produce irretrievable plastic deformations. To avoid this, periods of mechanical stimulation should be alternated with resting periods. This should be considered when realizing a load-based *in vitro* model of OA, since the loading regime should replicate as closely as possible the one of native articular cartilage. Mechanical stimuli should therefore be regulated both in frequency and in the balance between stimulation and resting periods.

1.3   OA models

Different models have been used to study the underlying mechanisms of osteoarthritis and to test new potential therapies. Models can be broadly classified as *in vivo* and *in vitro*.

In vivo models are widely used, as they provide the most accurate reflection of the naturally occurring whole-joint disease [19]. In these models, OA can be spontaneous, surgically induced or chemically induced [47]. In particular, anterior cruciate ligament transection and meniscectomy are commonly used methods to surgically induce degenerative joint lesions, which resemble those observed in post-traumatic OA. At least eighteen different animal species have been used to study established pathological features of OA. Small animals, such as mice, rats, rabbits, and guinea pigs, are relatively cheap, readily available and can be handled and housed with ease. However, tissue samples extracted from these animals tend to differ to a great extent in their anatomical and histological structure when compared to human ones. Larger animals, such as horses, pigs, sheep, and dogs, are more anatomically similar to humans and have a long life span, allowing for slower disease progression. These advantages, however, come with higher costs, longer experimental time, and greater ethical concerns. For these reasons, at present, there is no gold standard animal model used in OA research [47].

Despite the fact that a higher affinity to the clinical manifestations of OA can indeed be reached through *in vivo* experimentation, the complexity of *in vivo* models, as well as a shift towards the 3R's principle of refining, reducing and replacing the use of animals in science [48], makes *in vitro* modelling of the disease desirable [19]. Moreover, drug discovery campaigns require high-throughput experimentation and a high degree of parallelization, which are more easily achievable using *in vitro* models. The two most commonly used *in vitro* models of OA are cytokine-based and load-based models.

1.3.1   Cytokine-based models

During OA, synoviocytes, mononuclear cells or chondrocytes may increase their expression of catabolic proteins following the exposure to cytokines or chemokines, including IL-1β and TNF-α, which are present in the joint following synovial inflammation [19]. Pro-inflammatory cytokines are therefore ideal candidates for the induction of OA-like biological changes in articular cells or tissues in culture. Models of OA where cytokines are the primary method of induction are very common, due to their low cost and ease of manipulation. Cytokines added to culture medium have been shown to produce OA-like responses in chondrocytes in monolayer, such as a decrease in the expression of collagen type II and aggrecan [49] and an increase in the expression of MMP13,

collagen type X, VEGF and Runt-related transcription factor 2 (RUNX2) [50]. However, culturing chondrocytes in monolayer is problematic, due to their proneness to dedifferentiate into fibroblasts after a small number of passages [51], and to the absence of the normal ECM, which removes possible relevant matrix effects. A more accurate model of OA should therefore consider a 3D environment, which could be provided by explants or by tissue engineered constructs. Beekhuizer *et al.* [52] assessed the effect of OA synovium on human cartilage explants. Coculture of the two tissues, as compared to monocultures, resulted in a reduced GAG content and in the production of cytokine subsets more similar to the ones detected in OA synovial fluid *in vivo*. Francioli *et al.* [53] assessed the effect of IL-1β on pellets obtained from human articular chondrocytes (HACs). Exposure to IL-1β induced a decreased GAG content and an increased release of MMP1, MMP13, IL-8, monocyte chemoattractant protein-1 (MCP-1) and TGF-β1. Maturation of engineered cartilage was shown to regulate the response to cytokine stimulation: as compared to immature pellets, mature pellets responded to IL-1β by releasing lower amounts of MMP1 and MMP13, and increased amounts of IL-8, MCP-1, and TGF-β1. Sun *et al.* proposed another 3D model of OA [54]. Primary chondrocytes were cultured in silk protein porous scaffolds up to 21 days in static culture, with and without cytokine (IL-1β and TNF- α) exposure or with the use of macrophage conditioned medium. Cytokines suppressed aggrecan and upregulated MMP13, while macrophage conditioned medium suppressed collagen type II, upregulated ADAMTS5 and induced cell hypertrophy and apoptosis.

Subchondral bone plays an important role in OA [20], [28], and an accurate OA model should account for it. However, *in vitro* models considering the response of bone to cytokine stimulation are scarce. Pecchi *et al.* [55] showed that the exposure of osteoblasts to IL-1β resulted in an increased release of PGE2, MMP3 and MMP13. Osteoblasts stimulated with IL-1α actively synthesised NO in a dose-dependent fashion, while TNF-α failed to elicit a response [56]. Lin *et al.* [57] engineered an MSCs-derived osteochondral construct with a bone and a cartilage compartment, and exposed it to IL-1β. Treatment of the bone compartment with IL-1β resulted in an increased expression of MMP1, MMP3 and MMP13 in the chondral layer. This response was more pronounced than that seen with IL-1β application to the chondral component directly, suggesting an active biochemical communication between the two tissues.

Overall, anyway, no consensus on the most appropriate model for the representation of OA has been reached, and a clear understanding of all the pro-inflammatory cytokines involved in the pathology is still lacking.

1.3.2 Load-based models

Since OA is associated with several biomechanical risk factors (see section 1.1), an accurate *in vitro* model of this pathology should account not only for biochemical stimuli, but also for mechanical loading. For this reason, various load-based models of OA have been developed, both strain-controlled and stress-controlled. Cartilage is a mechanosensitive tissue, and is exposed to a wide range of mechanical stimuli *in vivo*. Chondrocytes sense the loading of their environment through a variety of mechanotransduction mechanisms, including integrin receptors [58], Piezo receptors [59], ion channels such as Transient receptor potential vanilloid 4 (TRPV4) [60], and the primary cilium, a unique, non-motile organelle located on the chondrocyte surface [61]. A moderate mechanical loading is necessary to maintain ECM homeostasis, but excessive forces stimulate stress-induced intracellular pathways, leading to the production of pro-inflammatory cytokines such as IL-1 and TNF-α [58]. Subchondral bone is also sensitive to load, varying its thickness, modulating its matrix resorption rate and changing its trabecular orientation in adaptation to the mechanical forces it is subjected to [28], [62].

The use of tissue explants is the simplest method to assess the effects of load, as it does not alter normal cell-matrix interactions [19]. Fitzgerald *et al.* [63] applied 25% and 50% static compression to bovine cartilage explants for periods between 1 and 24 hours. 24 hours of 50% compression produced a decrease in the expression of aggrecan and collagen type II, and an upregulation of MMP3, 9 and 13. Such a high strain exaggerates the maximal normal physiological load experienced by a joint *in vivo*, although this reflects the requirement of inducing an effect within a shorter time frame [19].

The response of cells to load can also be assessed by isolating cells, embedding them in an artificial scaffold and compressing them using a bioreactor [19]. As compared to the use of explants, this approach has the advantage of a higher reproducibility and a higher control over loading parameters. On the other hand, removing cells from their native matrix and embedding them into an artificial scaffold alters the native signalling network, and the force used in the experiments is dependent on the mechanical properties of the scaffold itself [19]. The choice of a suitable scaffold is therefore crucial. In a work by De Croos *et al.*, application of uniaxial, cyclic compression (1 kPa, 1 Hz, 30 min) on chondrocyte-laden calcium polyphosphate substrates significantly increased the expression of MMP3 and MMP13, resulting in ECM degradation [64]. However, this catabolic effect was followed by a significant increase in collagen type II and aggrecan expression at 12 h post-stimulation. Young *et al.* [65] assessed the effect of static and dynamic loading on chondrocyte-

laden chitosan/gelatine/β-glycerophosphate hydrogels. A static load exceeding 40 psi determined a decrease in the GAG content, an upregulation of MMP13 and IL-6 expression and a downregulation of aggrecan and collagen type II encoding genes within 24 h. In the cyclic group, a moderate (30-40 psi) loading resulted in enhanced ECM synthesis, while higher compression levels (60-120 psi) induced production of reactive oxygen species and ECM degradation.

As for bone loading models, Vazquez *et al.* [66] assessed the effect of cyclic compression on collagen gels seeded with osteocyte cell lines and layered with osteoblasts on their surface. Constructs showed an increased collagen type I expression upon loading, and osteocytes expressed PGE2 after mechanical stimulation.

Coculture models have also been used to assess the effect of loading on different articular tissues, studying their interactions. This is a fundamental aspect to be considered when realizing a model of OA, since this pathology affects multiple tissues of the native joint. Chondrocytes cocultured with osteoblasts showed a phenotypic shift towards hypertrophy, characterized by a decreased expression of collagen type II, aggrecan and SOX9, and an increased expression of collagen type X [67]. These changes were more marked in chondrocytes cocultured with excessively mechanically stressed osteoblasts. Moreover, application of excessive tensile stress on osteoblasts resulted in an increased expression of MMP1, MMP3 and MMP13 in chondrocytes, while proteoglycan and collagen were significantly decreased.

Overall, all models used in OA research seek to answer specific biological questions, but none of them allows the whole disease process to be studied. As a matter of fact, the absence of effective disease-modifying therapies is partly due to the lack of *in vitro* models able to recapitulate the complexity of OA and to provide insight into its pathogenesis [19], [47]. More advanced models therefore need to be developed, to better reflect the natural *in vivo* disease. A sufficiently accurate model of OA should comply with at least three requirements, namely a 3D environment, the involvement of multiple tissues, and the presence of both biochemical and biomechanical stimuli.

1.4 Microfluidics

Microfluidics is the science and technology of systems that process or manipulate small amounts of fluids, using channels with dimensions of tens to hundreds of micrometres [68]. This technology is widely spreading in the fields of chemistry, biology and medicine, thanks to a great number of advantages, including decreased cost in manufacture, reduced consumption of reagents

and analytes, decreased time of analysis, increased portability and unprecedented control over microenvironmental conditions [69], [70].

One of the main features of microfluidic devices is an extremely low Reynolds number. This dimensionless parameter is defined as the ratio between inertial forces and viscous forces within a fluid. For a fluid flow in a channel, the Reynolds number is expressed by the following equation:

$$Re = \frac{\rho v D_H}{\mu}$$
1.4.1

where ρ is the density of the fluid, v is the mean velocity, D_H is the hydraulic diameter of the channel and μ is the dynamic viscosity of the fluid. When the Reynolds number is low (<2000), the flow is laminar, while high Reynolds numbers correlate with turbulent fluid flows. Under typical microfluidic conditions, the Reynolds number is almost always lower than 1 [71]. This means that streams of fluid within the channels flow parallel along each other, and mass transport phenomena are exclusively diffusion driven, and therefore deeply controllable.

Scale effects also play a major role in microfluidics. The surface-to-volume ratio increases as the characteristic length L of a physical system decreases, being volume proportional to L^3 and surface to L^2. Therefore, when downscaling, diffusion, surface tension and surface effects become dominant with respect to volume forces such as gravity and inertia. Transport distances are minimized and interfaces between different phases are maximized, enhancing the efficiency of mass and energy transfer phenomena, and leading to faster reactions.

1.4.1 Soft lithography

Most of early microfluidic devices were fabricated by technologies derived from microelectronics, primarily photolithography [69]. This technique, however, has a number of limitations for applications related to biological systems. First of all, the need to carry out the whole process in a clean room is incompatible with a low-cost bulk production of microfluidic devices. Secondly, photolithography can be successfully applied only to a limited set of materials [72]. These limitations determined a shift towards soft lithography, a family of non-photolithographic techniques for fabricating and replicating micropatterns using soft substrates. In particular, one of the most used soft lithography techniques for the fabrication of microfluidic devices is based on rapid prototyping and replica molding [69]. The whole process, as schematized by Ng *et al.* [73], is shown in Fig. 1.4.1.
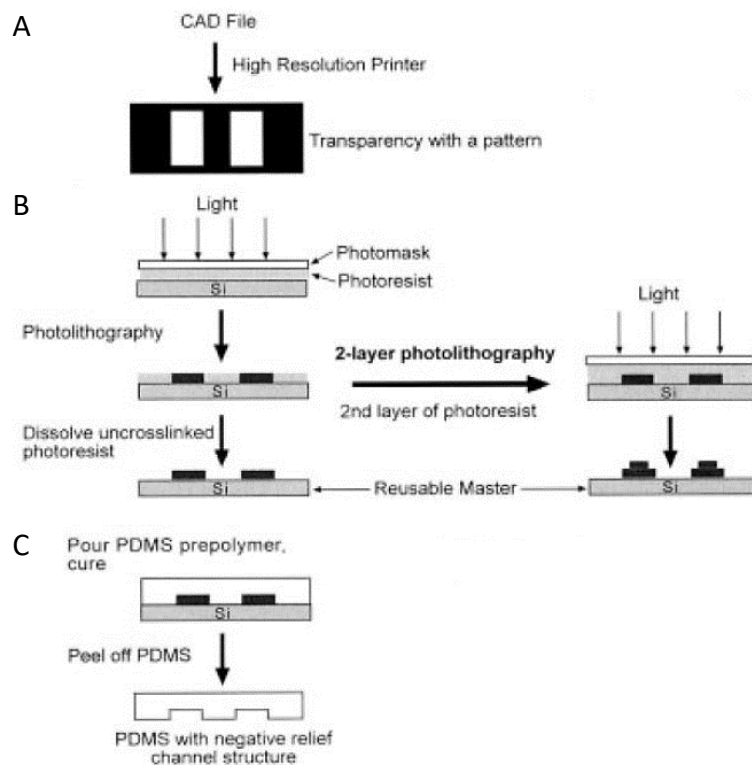
Fig. 1.4.1: *schemes for A) rapid prototyping; B) master fabrication by contact photolithography; C) replica molding [73].*

Rapid prototyping begins with the creation of a design for a device, through a computer-aided design (CAD) software. The CAD image is printed at high resolution on a transparent film, which serves as a photomask for contact photolithography (Fig. 1.4.1 A).

To produce the master mold, a layer of photoresist is spin-coated onto a silicon wafer, and is exposed to UV light through the photomask. This procedure can be repeated to obtain master molds with multiple layers. A solvent, called a developer, is applied to the surface after exposure to light. There are two classes of photoresists: positive and negative. Negative photoresists polymerize or crosslink when exposed to UV light. Areas that are not covered by the photomask become insoluble, while unexposed regions are dissolved by the developer. Positive photoresists, on the contrary, are degraded by UV light. Areas that are not covered by the photomask become soluble to the developer, while unexposed regions remain insoluble. After the removal of all the soluble portions of the photoresist, the desired features are left in relief on the surface of the wafer, serving as master mold for subsequent processing (Fig. 1.4.1 B).

Replica molding consists in pouring a mixture of polydimethylsiloxane (PDMS) and curing agent onto the master mold, to generate a negative replica of its features (Fig. 1.4.1 C). After a curing phase, PDMS can be peeled off the master, and inlets for microfluidic channels can be realized using a borer or a biopsy puncher. This phase no longer requires the use of a clean room, and can be

carried on under bench top conditions. Multiple replicas can therefore be produced from a single master, reducing the cost of production while increasing the ease of the process.

1.4.2 PDMS-based microfluidic devices

PDMS is a silicon-based elastomer, consisting of repeated units of $-O-Si(CH_3)_2-$. Its mechanical properties can be tuned varying the curing temperature, with a Young modulus ranging between 1.32 and 2.97 MPa [74]. PDMS offers several advantages, which make it appealing for the fabrication of microfluidic devices for biomedical applications: it is non-toxic to cells, inexpensive, optically transparent down to 300 nm (and therefore compatible with many imaging techniques) and permeable to gases [72], [75]. It is intrinsically hydrophobic, making microchannels difficult to wet, susceptible to air bubbles entrapment and prone to the adsorption of other hydrophobic species. However, its surface can be modified by exposure to air plasma to become hydrophilic [69]. Plasma treatment introduces silanol (Si-OH) groups on the surface of PDMS; these polar groups can condense with -OH-containing groups on other surfaces, forming covalent -Si-O-Si- bonds which allow a tight, irreversible seal between PDMS and other materials, such as glass or PDMS itself.
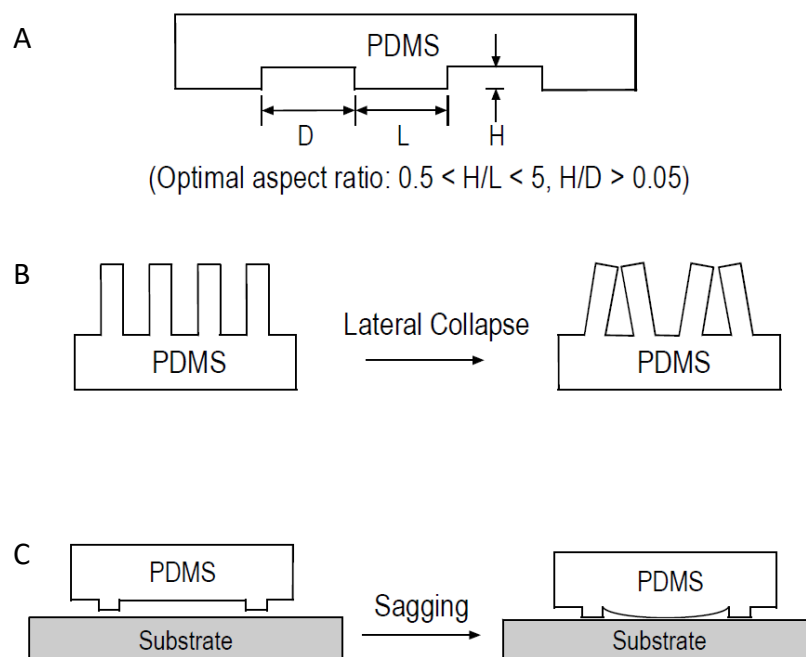
Fig. 1.4.2: A) optimal aspect ratio of PDMS structures; B) lateral collapse for aspect ratios H/L > 5; C) sagging for aspect ratios H/D < 0.05 [72].

Despite its several advantages, PDMS also has some drawbacks. Firstly, it shrinks upon curing at high temperatures. The shrinkage is about 1% for a curing temperature of 40°C, but increases to 2% when PDMS is cured at 80°C [76]. This should be considered when designing master molds. Secondly, the elastomeric character of PDMS introduces some limitations in the obtainable designs [72]. With reference to Fig. 1.4.2, if the aspect ratio H/L of the structure is too large, the stress

originating from gravity, adhesion, and capillary forces may cause a lateral collapse, also known as pairing (Fig. 1.4.2 B); alternatively, if the aspect ratio H/D is too small, the structure will not be able to withstand adhesion forces, and sagging will occur (Fig. 1.4.2 C). These problems can be minimized by designing microscopic features having 0.5 < H/L < 5, and H/D > 0.05.

1.5   Microfluidic devices for biological studies

Microfluidic systems have been used for a variety of biological applications, including immunoassays, separation of proteins and DNA, cell sorting, cell manipulation, and cell culture [71].

Immunoassays are procedures for the detection of analytes using specific antibodies. They usually require incubation times of hours, but microfluidics can significantly reduce the duration of the procedure, by minimizing the diffusion distance in microchannels, and by replenishing the diffusion layer with a fixed concentration of molecules. Linder *et al.* [77] developed an immunoassay for the detection of human immunoglobulin G (IgG) in a PDMS microchannel, requiring incubation times of only 1 – 6 minutes. Microfluidic systems also allow to perform a large number of biochemical assays in parallel. Ismagilov *et al.* [78] developed a microarray composed of two PDMS layers with orthogonal channels separated by two polycarbonate membranes and a microwell. This approach allowed the rapid, high-throughput screening of N samples against M reagents in a single device.

Another interesting application of microfluidic techniques is the separation of proteins and DNA. Capillary electrophoresis, in particular, can be easily implemented in a PDMS-based microfluidic device. The advantages of miniaturization include reduced cost and analysis time, and the possibility to separate and detect single DNA molecules [79].

The complex structures obtainable through soft lithography opened up new perspectives for cell sorting, manipulation, and culture. Microfluidic devices have been developed to separate and analyse singe cells [80], or to expose cells to stable gradients of molecules in solution [81]. Importantly, microfluidic devices can also be used to recreate *in vitro* complex 3D organ-level structures. [82]. These "organs-on-a-chip" provide an unprecedented control over the microenvironment at the cellular scale, allowing the creation of structures that support cell differentiation and recapitulate the tissue-tissue interfaces, spatiotemporal chemical gradients, and mechanical cues of living organs [82]. This approach, integrating microfluidics technologies with living cells cultured in a 3D environment, enables the study of human physiology in organ-specific contexts, and the development of specialized *in vitro* disease models. The possibility to use human

cells, the recapitulation of organ-level functionalities, and the reduced experimental costs and time make organs-on-a-chip potential replacements for animals used in drug development and toxin testing [82].
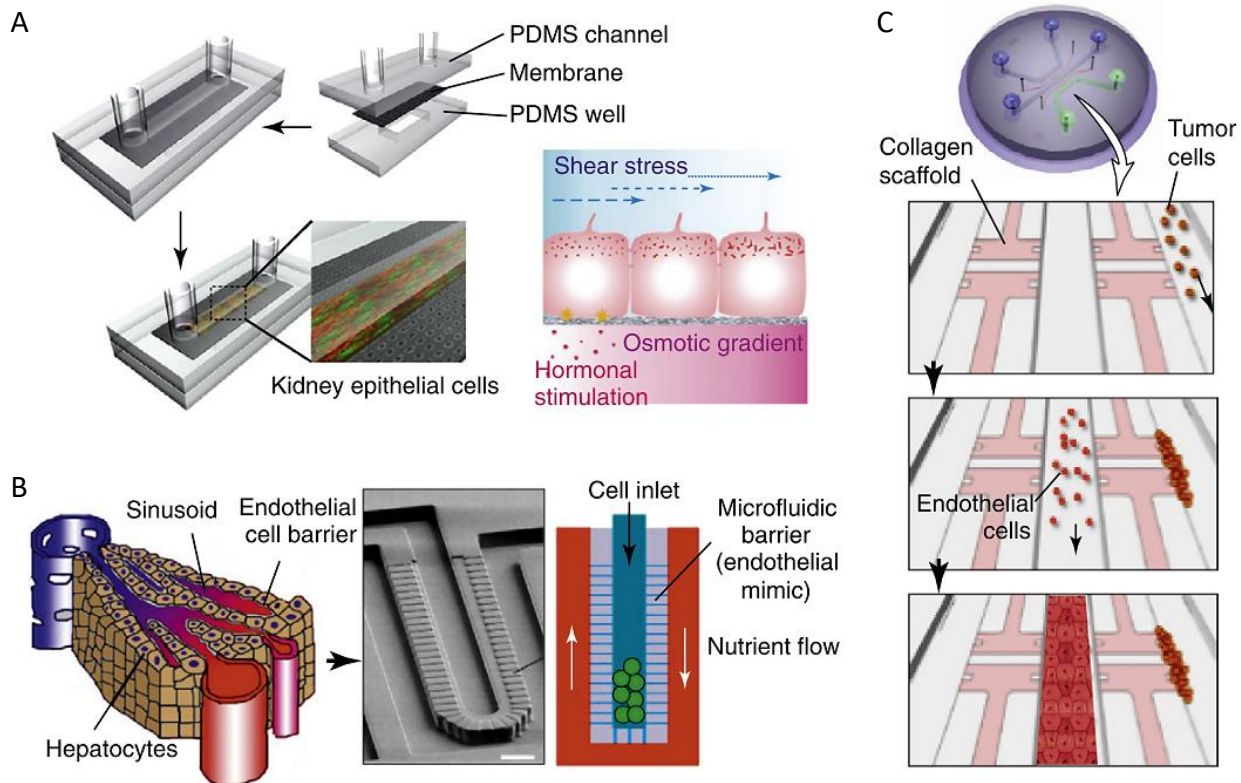
Fig. 1.5.1: *examples of micro engineered organs-on-a-chip, as reported by Huh et al. [82]. A) microfluidic model of kidney epithelium, incorporating stacked layers of PDMS microchannels and a PDMS well separated by a porous polyester membrane; B) a micro engineered liver-on-a-chip, consisting of a central liver cell culture chamber and a surrounding nutrient flow channel, separated by barriers patterned with a set of narrow microchannels that mimic the highly permeable endothelial barrier between hepatocytes and the liver sinusoid; C) microfluidic device for the study of heterotypic interactions between tumour cells and endothelial cells.*

Fig. 1.5.1 shows some representative examples of organs-on-a-chip, as reported by Huh *et al.* [82]. The microfluidic kidney epithelium model shown in Fig. 1.5.1 A provided a physiologically relevant culture environment for polarized kidney epithelial cells, and enabled precise control of fluid flow, selective exposure of the apical and basal sides of the cells to physical and biochemical stimuli, and collection of samples from both sides of the tissue [83]. The liver-on-a-chip developed by Lee *et al.* [84] (Fig. 1.5.1 B) closely approximated transport of nutrients and waste products in the liver sinusoid, and provided more favourable environments for the maintenance of primary liver cells in a differentiated state. The microfluidic system schematized in Fig. 1.5.1 C was used to model the tumour microenvironment, and gain better understanding of important processes such as angiogenesis and cancer cell invasion during cancer progression [85].

1.5.1 Pillar-based and hydrogel-incorporating microfluidic devices

A 3D culture microenvironment is a fundamental requirement for the development of sufficiently accurate physiological or pathological *in vitro* models [82]. Hydrogels, i.e., crosslinked polymeric networks that swell in the presence of water, are attractive materials for 3D cell cultures, due to their structural and mechanical properties similar to the ones of native ECM [86]. They possess a high water content and allow the transport of oxygen, nutrients, waste products and soluble factors. Furthermore, many hydrogels can be formed under mild, cytocompatible conditions, allowing the embedment of cells within the hydrogel prior to its crosslinking. Moreover, it is possible to modify the hydrogel composition in order to incorporate cell adhesion ligands and to obtain the desired mechanical properties and degradability [86]. Various natural and synthetic hydrogels have been successfully incorporated into microfluidic systems to support cells in a 3D environment. While the use of hydrogels to create 3D cell laden constructs within microfluidic devices is therefore appealing, providing an appropriate spatial localization of the still liquid solution during the injection, while allowing a sufficient contact surface with adjacent compartments and culture medium channels, poses some challenges [87].

Huang *et al.* [88] proposed a method to create a defined confinement region for cell laden hydrogels, using arrays of micropillars (Fig. 1.5.2). Regularly spaced micropillars allowed to maintain the integrity of the gels within individual channels, and concurrently permitted cell-medium and cell-cell interactions between adjacent channels. This versatile design allowed the development of microfluidic devices with multiple gel channels, which could be independently filled with distinct hydrogels, either through thermally or photo-crosslinked polymerization (Fig. 1.5.2 B). Such devices were used, for instance, to coculture breast cancer cells and tumour-associated macrophages, providing a model of the tumour microenvironment.

Gel entrapment during the injection phase was found to depend on three variables, namely the spacing between pillars, the surface properties of the microfluidic device, and the viscosity of the hydrogel precursor solutions. Various spacings were systematically tested, and spacings up to 200 μm were found to contain gels within a 400 μm wide gel channel. Hydrophobicity of the devices increased the probability of maintaining an intact gel interface, while hydrophilic surfaces facilitated gel leakage into neighbouring channels. Finally, hydrogels exhibiting a higher viscosity displayed an increased chance of leakage.
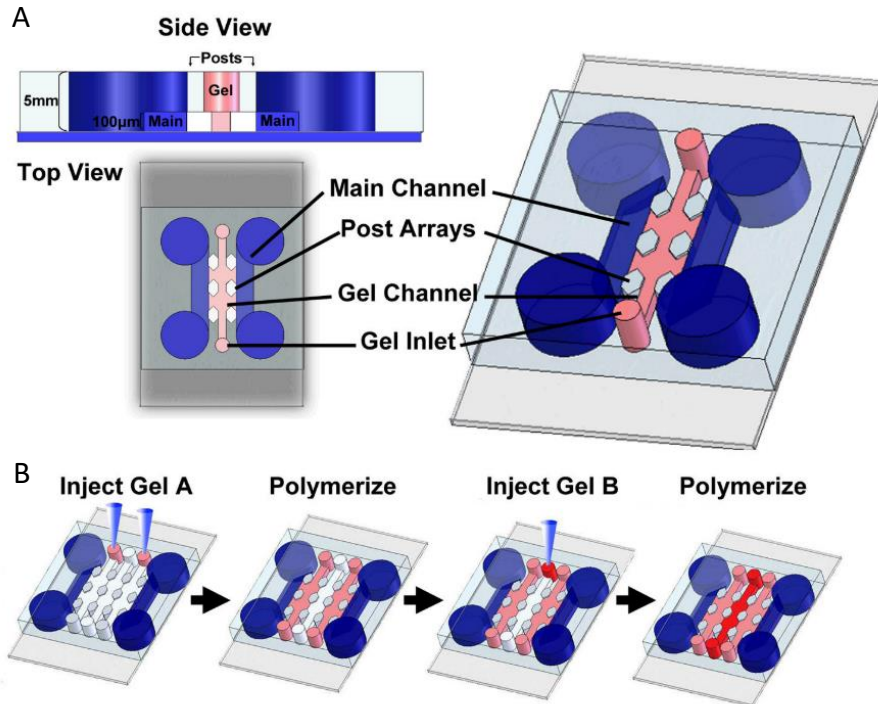
Fig. 1.5.2: *scheme of the microfluidic device developed by Huang et al. [88]. Different versions of the device were developed, hosting A) a single gel channel, or B) multiple gel channels.*

To describe the gel injection process from a physical point of view, Huang *et al.* [88] developed a mathematical model based on a modified theory of the capillary burst valve (Fig. 1.5.3). When an advancing liquid interface meets the straight section of a pillar at equilibrium, the difference between the pressure inside the liquid P_i and the atmospheric pressure P_o is given by the Young-Laplace equation:

$$P_i - P_o = -2\gamma \left(\frac{cos\theta_s}{w} + \frac{cos\theta_v}{h} \right)$$

<div align="right">***1.5.1***</div>

where γ is the surface tension of the liquid, w and h are the width and the height of the channel, respectively, θ_s is the advancing contact angle formed between the liquid interface and the side wall, and θ_v is the advancing contact angle between the liquid and the top and bottom walls. The liquid interface can only move forward when the contact angles with the walls exceed the critical advancing contact angle θ_A. When the interface meets the edge of a pillar, the contact angle with the new wall is reduced, which causes the contact line to stop. For the contact line to resume advancing, the interface should bulge until the contact angle with the new wall increases to θ_A, leading to an increase in the contact angle formed with the old wall from θ_A to θ_1. For this purpose, the driving pressure difference $P_i - P_o$ should be greater than:

$$\Delta P = -2\gamma \left(\frac{cos\theta_1}{w} + \frac{cos\theta_A}{h} \right)$$

<div align="right">***1.5.2***</div>

Through a proper dimensioning of the central channel and the spacings between confining pillars, it is therefore possible to obtain a preferential advancement direction. For a correct injection, the driving pressure difference should be greater than a minimum threshold value ΔP_{width}, necessary for the advancement of the fluid in the gel channel, but lower than a maximum value ΔP_{gap}, which would determine the leakage of the fluid in the adjacent channels. Huang *et al.* predicted that if the differential $\Delta P_{width} - \Delta P_{gap}$ exceeds a minimum value of 500 Pa, leakage will most likely not occur. This differential can be maximized by using hydrophobic materials for the device and by optimizing the design of channels, pillars and spacings.
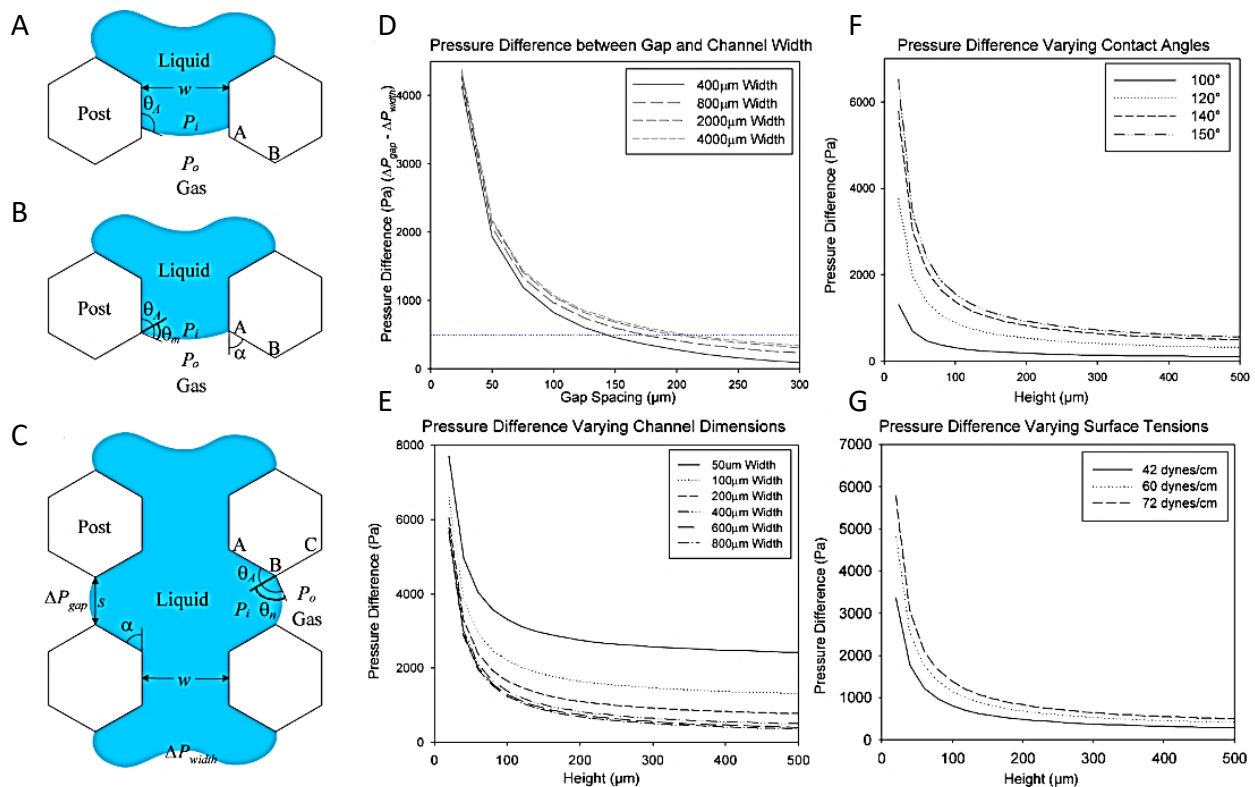
Fig. 1.5.3: *A-C) diagram of the filling process in a channel; D-G) graphs of calculated pressure differences across a variety of parameters [88].*

1.5.2   Mechanically active microfluidic devices

The capacity to deliver mechanical stimuli is a fundamental requirement for devices aimed at modelling pathophysiological states of mechanically active tissues and organs (including joints). For this reason, various microfluidic devices providing cells with mechanical stimuli have been developed. Huh *et al.* [89], for instance, developed a microfluidic device reproducing the functional alveolar-capillary interface of the human lung. Microvascular endothelial cells and alveolar epithelial cells were cultured on the two sides of a porous PDMS membrane coated with collagen or

fibronectin. The membrane was bound to two lateral chambers, as shown in Fig. 1.5.4. Vacuum was cyclically applied to the chambers, producing a stretching of the membrane which in turn provided cells with uniform and unidirectional strains matching those observed in native alveoli. Similar designs have been used to develop microfluidic models of kidney glomerulus and gut [90], [91].
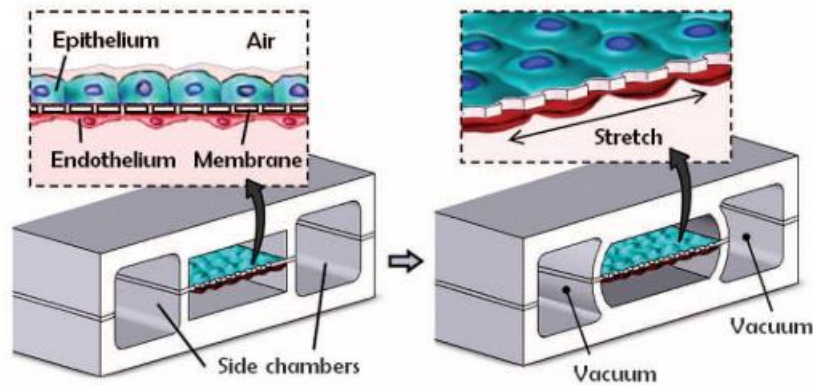
Fig. 1.5.4: *scheme of the microfluidic device developed by Huh et al. [89]. The device recreated physiological breathing movements by applying vacuum to the lateral chambers and causing mechanical stretching of the PDMS membrane.*

Another approach, developed by Marsano *et al.* [92], combined the use of a stretchable membrane to provide mechanical stimuli with the use of micropillars to confine a cell laden hydrogel within the microfluidic device. The device, schematized in Fig. 1.5.5, consisted in two compartments, separated by a 300 μm thick PDMS membrane. The top compartment was composed of two lateral channels for culture medium and a central channel hosting a cell laden hydrogel. The channels were divided by two rows of equally spaced hanging pillars with a hexagonal cross-section. A 50 μm wide gap was present between the pillars and the membrane. When the bottom compartment was pressurized by a pneumatic actuation system, the PDMS membrane bended upwards, compressing the hydrogel and eventually abutting onto the pillars. This microdevice was used to generate mature and highly functional micro-engineered cardiac tissues from both neonatal rat and human induced pluripotent stem cell-derived cardiomyocytes.
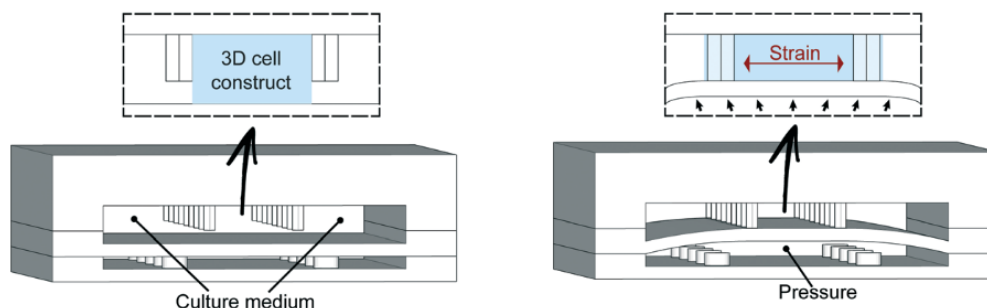
Fig. 1.5.5: *scheme of the heart-on-a-chip device developed by Marsano et al. [92]. The device recapitulated the physiological mechanical environment experienced by cells in the native myocardium, through the induction of cyclic uniaxial strains.*

1.5.3 Microfluidic osteochondral models

In recent years, many attempts have been made to develop microfluidic models of osteochondral tissues. Lee *et al.* [93], for instance, described a PDMS-based pneumatic microfluidic device for the stimulation of cartilaginous cell constructs. Chondrocyte laden alginate hydrogels were compressed by PDMS balloons, actuated by pressurized air. Balloons of different sizes allowed the generation of multiple compression conditions in a single platform. A scheme of the device is shown in Fig. 1.5.6.
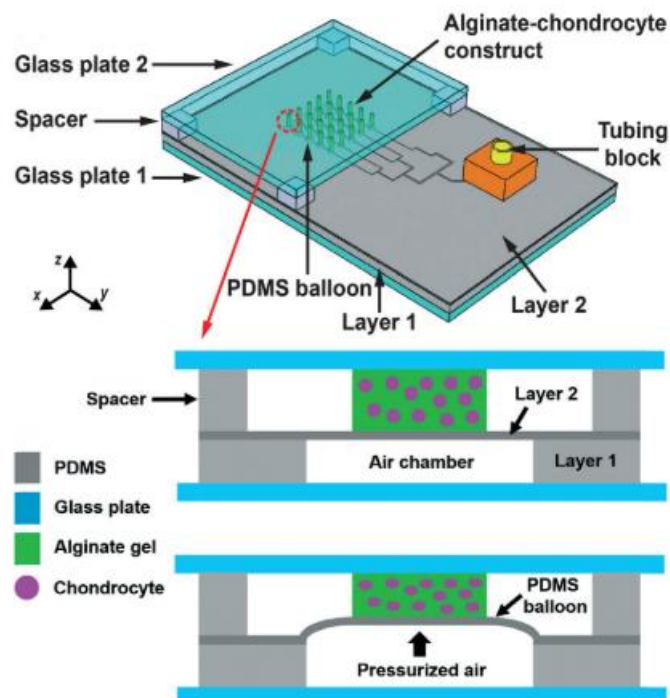
Fig. 1.5.6: *scheme of the device developed by Lee* et al. *[93].*

A different approach, based on the design previously described by Marsano *et al.* [92], was adopted by Mainardi [94] to develop a microfluidic device for the 3D culture and mechanical stimulation of cartilaginous constructs. The device consisted in a culture chamber, with two rows of micropillars confining the hydrogel-based cell construct, and an actuation chamber. The two compartments were separated by a membrane, whose thickness was increased from 300 to 750 µm to make the actuation pressure independent of the presence of the cell construct in the culture chamber. The geometry of micropillars was optimized, to provide a better hydrogel confinement and limit the unwanted lateral strain borne by cells. A T-shaped cross-section, thanks to its high area moment of inertia, was shown to be the ideal choice to limit the lateral displacement of the hydrogel without increasing too much the thickness of the pillars, which would lead to air entrapment within the device. Spacings between pillars were decreased from 50 to 30 µm, to further enhance gel confinement. Different heights were adopted for the gaps underneath the micropillars. In this way,

the device could provide cells either with physiological (10%) or hyperphysiological (30%) compression stimuli. Nasal chondrocytes were embedded in a polyethylene glycol (PEG)-based hydrogel and cultured in the device, and the effect of the cyclic application of different compression levels on the cell constructs was assessed. The device is visible in Fig. 1.5.7.
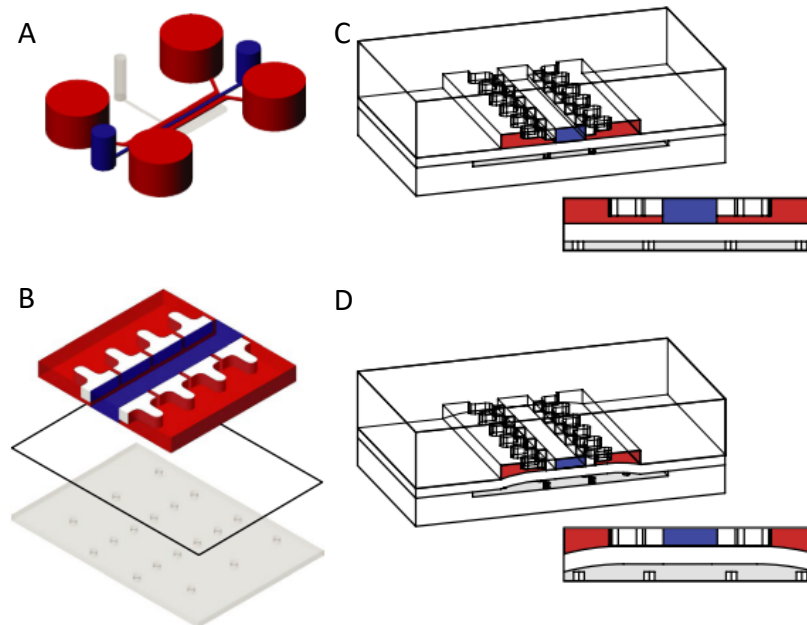
Fig. 1.5.7: *scheme of the device used by Mainardi [94] and Occhetta et al. [95]. A) the device consists in two compartments, separated by a membrane. The top compartment is composed of a central gel channel (in blue) and two lateral medium channels (in red). The bottom compartment represents the actuation chamber (in grey); B) detail of the two compartments; C) at rest condition the actuation chamber is kept at atmospheric pressure, and the actuation membrane is flat; D) when the actuation chamber is pressurized, the membrane bends upwards, compressing the cell construct.*

Occhetta *et al.* [95] used the same microfluidic platform to assess the effect of cyclic hyperphysiological compression on HACs. Cells exhibited a shift towards an osteoarthritic phenotype, characterized by an upregulation of hypertrophic markers such as collagen type X and Indian Hedgehog (IHH), and a downregulation of hypertrophy inhibitors such as Frizzled related protein (FRZB), Dickkopf-related protein 1 (DKK1) and Gremlin1 (GREM1). The model was validated on well-established anti-inflammatory and anticatabolic compounds, and was used for the testing of a novel drug candidate with MMP inhibition activity.

While cartilage is populated by a single cell type, and can be modelled *in vitro* with relative ease, the design of *in vitro* models of bone is particularly challenging, both because osteocytes are intrinsically difficult to culture *in vitro* [19], and because an exhaustive model should consider the complex interactions between bone itself and vasculature [96]. Bersini *et al.* [97] cocultured endothelial cells and MSCs differentiated towards the osteogenic lineage in a microfluidic device,

recreating a vascularized bone microenvironment. The device comprised eight 225 μm long, 120 μm wide and 150 μm high gel regions, interfacing with a central medium channel. The model was used to analyse the transendothelial migration of metastatic breast cells into bone. Nasello *et al.* [98] developed a microfluidic platform incorporating a collagen type I hydrogel seeded with primary human osteoblasts. The device consisted in three 1.145 mm wide and 290 μm high gel channels and two lateral medium channels, separated by rows of equally spaced trapezoidal pillars. The structural and biochemical microenvironment induced the mineralization of the collagen matrix and the differentiation of osteoblasts into osteocytes.

Calcified cartilage plays an important role in OA [20], [27], and it should be considered when modelling the native environment of an osteoarthritic joint. However, microfluidic models focusing on this tissue and its interactions with hyaline cartilage are lacking. Moreover, at present there are no available microfluidic models considering the response of this tissue to mechanical overloading, which is a crucial element for the development and the progression of OA. For this reason, a mechanically active, multi-tissue microfluidic device for the culture of 3D osteochondral constructs is required.

1.6 Thesis aim

OA is a musculoskeletal disease affecting nearly 5% of the global population, with 15 million new cases diagnosed each year [10]. Despite its high prevalence and incidence, no satisfactory therapies are, however, available [2]. This lack is partly due to the absence of *in vitro* models able to recapitulate the complexity of OA and provide insight into its pathogenesis [19], [47]. The application of microfluidics to cell biology studies, with the development of organs-on-a-chip, recently opened up new perspectives, making it possible to provide *in vivo*-like complex stimuli (e.g., mechanical cues, fluid flow, highly controlled chemical diffusion) with an unprecedented control over the cellular microenvironment [82]. This, together with other benefits of miniaturization, such as the reduction in costs and time of experiments, makes microfluidic devices particularly appealing to produce pathophysiological tissue models [82], [89]. Previous studies demonstrated the feasibility of developing representative microfluidic models of OA. Occhetta *et al.*, for instance, induced an osteoarthritic phenotype in articular chondrocytes in a cartilage-on-a-chip model, by means of a cyclic hyperphysiological compression [95]. This study, however, only focused on hyaline cartilage, while OA is widely recognized as a pathology affecting the whole joint [17], [20]. A multi-tissue model is therefore needed to better recapitulate the pathology complexity.

INTRODUCTION

In this framework, the aim of the present work is to develop and validate a microfluidic device able to model *in vitro* some key features proper of an osteoarthritic osteochondral interface. Specifically, the device should host two 3D hydrogel-based cell laden constructs with a direct interface, to study the direct tissue-tissue crosstalk proper of joints. Moreover, it should allow the mechanical overloading of the cell constructs, to recreate one of the major risk factors for the development and the progression of OA. A pre-existing microfluidic platform [94] was used as a starting point, and its features were re-designed to allow the hosting and the stimulation of two separate cell constructs. An enzymatically crosslinkable and cleavable eight-arm PEG-based hydrogel [99], previously demonstrated to be suitable for the differentiation of cartilaginous microtissues [94], [95], was adopted to generate the cell constructs.

The main work was articulated into three steps:

i. Design and production of a mechanically active microfluidic device for the 3D culture and the mechanical stimulation of two cell constructs with a direct interface, considering different stimulation conditions.

ii. Generation of a healthy osteochondral construct consisting in a hyaline cartilage compartment (from HACs) and a calcified cartilage compartment (from bone marrow derived MSCs), and optimization of the interface between the two tissues.

iii. Induction of OA traits in the osteochondral construct, through the application of a cyclic hyperphysiological compression.

Notably, while the culture conditions to obtain HACs-based hyaline cartilage and induce OA traits in it were available [95], no present work focuses on calcified cartilage. The generation of a calcified cartilage construct from bone marrow derived MSCs in single culture and the induction of OA traits in the construct through the application of a cyclic hyperphysiological compression were therefore pursued using an available device [94], as a preliminary biological aim and as a control to properly discern the effect of coculture.

Microfluidic devices were designed and fabricated at Politecnico di Milano (Milan, Italy), in the Microfluidics and Biomimetic Microsystems Laboratory (MiMic Lab, Department of Electronic, Information and Bioengineering); biological validation and culture optimization were performed at Universitätsspital Basel (Basel, Switzerland), in the Tissue Engineering Laboratory (TE Lab, Department of BioMedicine).

2 MATERIALS AND METHODS

2.1 Design of the microfluidic device

As previously discussed, the ultimate goal of this thesis is to produce and validate a microfluidic device able to recreate *in vitro* the environment of an osteoarthritic osteochondral interface. To achieve this goal, the device should comply with the following project requirements:

i. Allow the coculture of two 3D constructs, consisting in cell laden hydrogels, under controlled biochemical and biomechanical conditions. The two hydrogels should host two different cell populations, namely chondrocytes and hypertrophic chondrocytes, to model the hyaline cartilage and the calcified cartilage of the native joint, respectively.

ii. Guarantee the presence of a direct interface between the two cell constructs.

iii. Deliver controlled mechanical stimuli to the cell constructs. In particular, the desired compression level was set equal to 30% for the hyaline cartilage construct, since previous studies showed that this hyperphysiological stimulation was able to induce an osteoarthritic phenotype in chondrocytes [94], [95]. The desired compression level for the calcified cartilage construct was set either to 30% or to zero (see section 2.1.1).

iv. Guarantee an adequate diffusion of solutes within the hydrogels, to provide cells with the optimal amount of nutrients and differentiation factors.

Fig. 2.1.1 shows a sketch of the device. The design is based on a pre-existing microfluidic platform [94], which was adapted to host two separate cell constructs. The device, fabricated in PDMS, consists in three layers: a culture chamber (top layer, grey in Fig. 2.1.1 B), an actuation chamber (middle layer, blue in Fig. 2.1.1 B) and a floor (bottom layer, green in Fig. 2.1.1 B).The first two layers present microscopic features, while the latter is smooth and unpatterned.

The culture chamber is composed of four 6570 µm long channels: two central ones to host the hydrogel-based cell constructs, and two lateral ones to provide the culture medium. The gel channels are separated from the medium channels by a row of lateral pillars hanging from the ceiling of the chamber, while a central continuous wall or a series of pillars separates the two gel channels from each other. Each channel has its own inlet and outlet. The culture chamber lies on a deformable membrane, which separates it from the actuation chamber. A gap is present between the membrane and the bottom surface of the wall/pillars. When the actuation chamber is pressurised, the membrane bends upwards, thus compressing the hydrogels (Fig. 2.1.1 C). The wall and the pillars provide a mechanical stop to the membrane, in order to avoid an excessive

deformation of the cell constructs. In this way, by applying a cyclic pressure to the membrane, it is possible to provide cells with strain-controlled stimuli. The nominal strain in the vertical direction ε depends therefore on the height of the gap and the pillars through the following equation:

$$\varepsilon = \frac{Gap\ height}{Total\ height} = \frac{Gap\ height}{Gap\ height + Pillar\ height}$$

2.1.1

The membrane thickness had already been optimized for a device that closely resembled the ones used in the present work [94], showing that a minimum value of 750 μm was necessary to guarantee its proper functioning. This value was further increased by a security factor, and a final thickness of 1 mm was adopted in the present work. To avoid the sagging of the membrane due to its own weight, six rows of cylindrical posts were inserted in the actuation chamber. The diameter of the posts was set equal to 59 μm; the distance between two subsequent posts (centre-to-centre) ranged between 215 μm in the central region of the actuation chamber and 455 μm in the peripheral region; the distance between the rows ranged between 400 and 495 μm. The height of the actuation chamber was set equal to 50 μm.
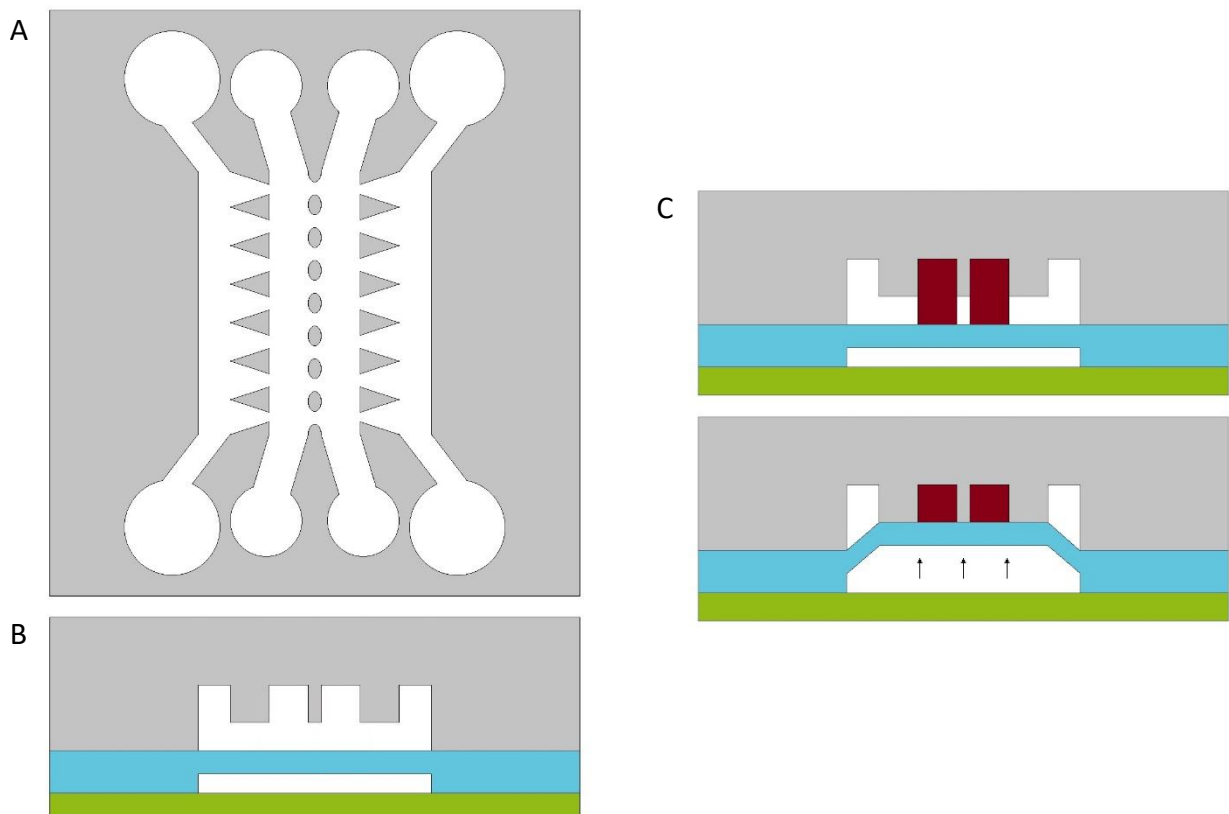
Fig. 2.1.1: *A) sketch of the culture chamber of the microfluidic device, top view; B) sketch of the section of the device. The culture chamber is represented in grey, the actuation chamber in blue and the floor in green; C) operating principle of the device. When the actuation chamber is pressurised, the membrane bends upwards, compressing the cell constructs (represented in red).*

To guarantee the proper functioning of the device and the compliance with the project requirements, further calculations were performed, to optimize the following parameters:

- Width of the gel channels;

- Height of the culture chamber and the gap;

- Design of the pillars.

2.1.1 Device versions

Different device versions were developed, varying the interface between the cell constructs, the produced mechanical stimulation, and the width of gel channels.

As regards the interface, two options were considered, one consisting in a row of pillars separating the constructs, the other consisting in a continuous wall. In principle, a wall should allow a better confinement of the hydrogels and a smoother interface between them. On the other hand, this configuration reduced the contact surface between the cell constructs, which was limited to the gap present between the bottom surface of the wall and the actuation membrane.

Two different stimulation conditions were also tested: in the first one ("symmetric"), a gap was present underneath all the lateral pillars and the central wall/pillars. In this way, a homogeneous 30% compression of both the cell constructs should ideally be achieved. In the second condition ("asymmetric"), the gap was maintained only on the side of the device aimed at containing the hyaline cartilage construct, while the lateral pillars on the other side and the central wall/pillars occupied the whole height of the culture chamber. The aim of this configuration was to apply the compression only to the hyaline cartilage construct, while reducing the amount of strain borne by the calcified cartilage one, thus being more similar to the compression levels found *in vivo*, where the superficial and middle layers of articular cartilage incur most of the deformation, while the strains in the deep and calcified layers are smaller [43].

Finally, concerning the width of the central channels, an optimization procedure was carried out as discussed in detail in section 2.1.2.

Three versions of the device were realized, combining the features described above:

- In the first version, the symmetric configuration was adopted, and the two central channels were separated by a row of suspended pillars hanging from the ceiling of the actuation chamber. Central pillars had a hexagonal cross-section, with a width of 50 μm and a length of 90 μm. The distance between two subsequent pillars was set to 50 μm. This version of the device, visible in Fig. 2.1.2 A, will be hereinafter referred to as "Pillar".

- In the second version of the device the symmetric configuration was maintained, but the central row of pillars was substituted with a continuous 50 µm wide wall. This version of the device ("Wall") is shown in Fig. 2.1.2 B.

- In the third version ("UniLat"), the central row of pillars was reintroduced instead of the continuous wall. In this case, the asymmetric configuration was adopted. The cross-section and a top view of this device are visible in Fig. 2.1.2 C. An asymmetric device with a wall interface was not produced, since this combination would eliminate completely the contact surface between the two cell constructs.
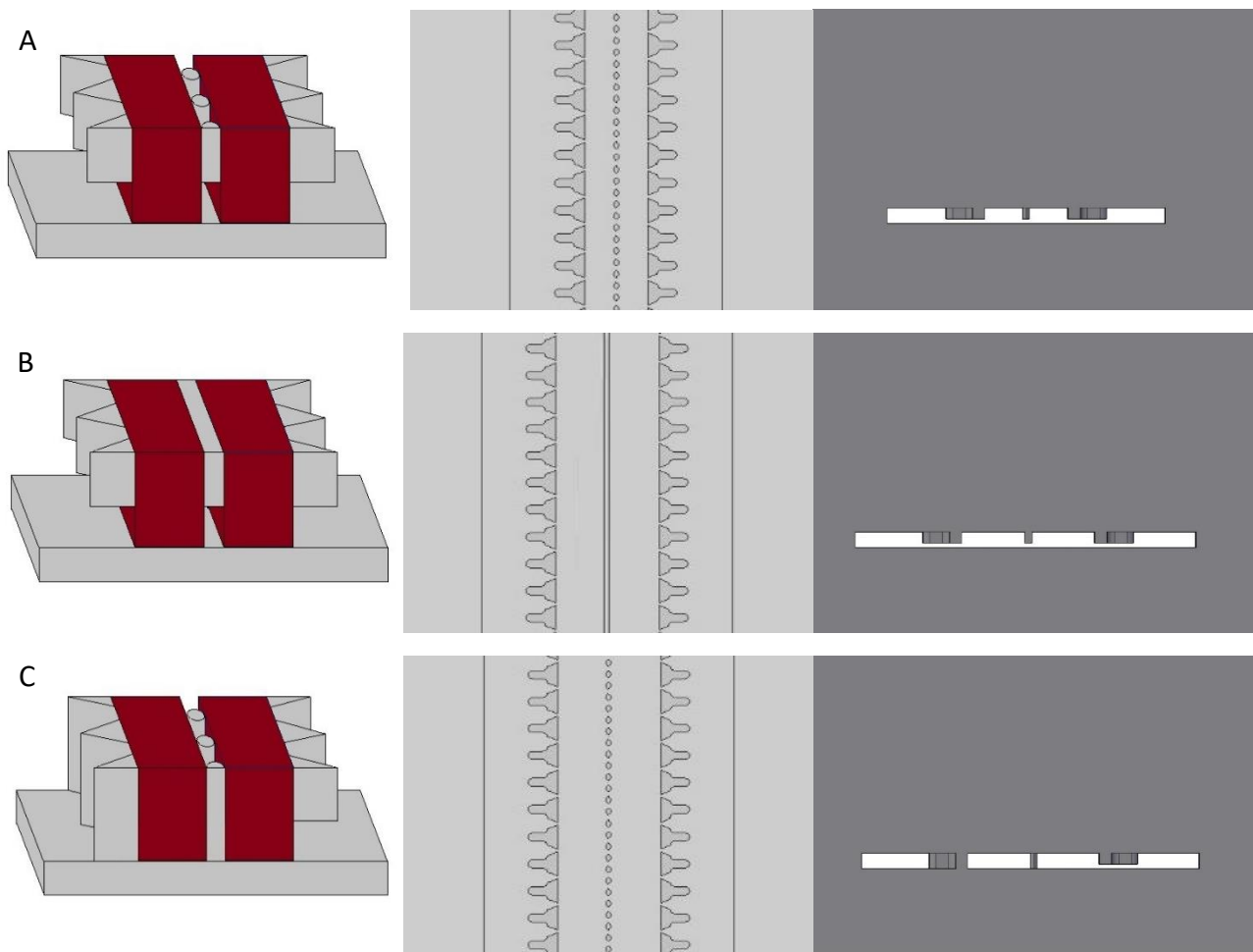
Fig. 2.1.2: *A) left: sketch of the culture chamber in the Pillar device. Cell constructs are represented in red; centre: top view of the Pillar device (detail); right: cross-section of the Pillar device (detail); B) left: sketch of the culture chamber in the Wall device; centre: top view of the Wall device (detail); right: cross-section of the Wall device (detail); C) left: sketch of the culture chamber in the UniLat device; centre: top view of the UniLat device (detail); right: cross-section of the UniLat device (detail).*

2.1.2 Channels width

The channels width was optimized to guarantee an adequate diffusion of solutes within the hydrogels. Ideally, the concentrations of both glucose, oxygen, and differentiation factors such as TGF-β should be evaluated, however no data are available in literature concerning cell uptake of differentiation factors. Therefore, only oxygen and glucose were considered during design optimization procedures. Moreover, since PDMS is permeable to oxygen and chondrocytes have a low basal oxygen uptake [100], glucose concentration was adopted as the most critical parameter for the dimensioning. The general diffusion-convection equation (equation 2.1.2) was used to evaluate the glucose concentration C within the construct:

$$\frac{\partial C}{\partial t} = D\nabla^2 C - V(C) + P(C) - (\boldsymbol{v} \cdot \nabla)C \qquad \textbf{\textit{2.1.2}}$$

where t is time, D is glucose diffusion coefficient in the medium, equal to 10^{-5} cm^2/s at 37°C [101], V(C) and P(C) are its volumetric consumption and production rates, respectively, and **v** is the velocity field. Some hypotheses were introduced to simplify the model:

- The presence of both the lateral pillars and the central wall/pillars was neglected.
- The culture chamber was modelled as a single parallelepiped with a width w_{tot} equal to the sum of the widths of the two gel channels (w_{gel}) and of the central wall/pillars (w_c = 50 µm):

$$w_{tot} = 2w_{gel} + w_c \qquad \textbf{\textit{2.1.3}}$$

- Glucose concentration was considered to vary only along the width of the culture chamber, while being homogeneous along its length and height.
- Glucose concentration in the medium was considered to be homogeneous in space and constant in time. Actually, the total amount of glucose in the medium should eventually decrease due to cell consumption, however this reduction was neglected since the volume of culture medium contained in the lateral channels and in the reservoirs was much larger than the volume of the cell constructs.
- Steady-state conditions were considered.
- Convection was neglected, i.e., the velocity of the medium was set equal to zero.
- The problem was considered as symmetric with respect to the vertical plane passing through the axis of the culture chamber.
- Glucose production by cells was set equal to zero.
- The volumetric glucose consumption was considered as constant, and equal to:

$$V(C) = R \cdot N \qquad \textbf{\textit{2.1.4}}$$

where R is the cellular glucose consumption rate and N is the cell density within the construct. N was $50*10^6$ cells/ml, while R was set equal to 0.126 µmol/(10^6 cells*h) [101], leading to a volumetric consumption of $1.75*10^{-3}$ µmol/(ml*s). No differences were expected between the hyaline cartilage construct and the calcified cartilage one.

Under these hypotheses, equation 2.1.2 became:

$$D\frac{\partial^2 C}{\partial x^2} = V(C)$$

2.1.5

which was solved analytically introducing the following boundary conditions:

$$J(x = 0) = 0$$

2.1.6

where J is the glucose flow, resulting from the symmetry of the problem with respect to x = 0, which corresponds to the mid-point of the culture chamber width, and:

$$C\left(x = \frac{w_{tot}}{2}\right) = C_0$$

2.1.7

where $w_{tot}/2$ corresponds to the lateral side of the gel and C_0 is the glucose concentration in the culture medium present in the lateral channels of the device, equal to 4.5 µmol/ml. The profile of glucose concentration within the hydrogel was obtained integrating equation 2.1.5 twice:

$$C(x) = C_0 + \frac{V}{2D}\left(x^2 - \frac{w_{tot}^2}{4}\right)$$

2.1.8

The minimal acceptable glucose concentration was set equal to 2.7 µmol/ml, value below which the metabolism of chondrocytes changes [100]. This value was imposed at the most critical position within the construct, i.e., x = 0. Solving for w_{tot}, equation 2.1.8 becomes:

$$w_{tot} = \sqrt{\frac{8D}{V}(C_0 - C(0))}$$

2.1.9

which sets the maximum acceptable value for w_{tot} to 2868 µm. Introducing this value in equation 2.1.3, the maximum gel channel width w_{gel} results equal to 1409 µm.

This value, obtained considering ideal conditions, was reduced by a safety coefficient. Further considerations were made to set the final channel width: a lower value would reduce the number of cells needed for the tests (by reducing the total volume of the gel channel) and would result in a higher surface-to-volume ratio; on the other hand, it would also produce a higher unwanted lateral strain within the cell constructs [102]. According to these considerations, two different gel channel widths were used, namely 500 µm and 300 µm. A width of 765 µm was adopted for the lateral channels, instead.

2.1.3   Culture chamber and gap height

The height of the pillars was set equal to 100 μm, while the height of the gap was set equal to 43 μm, leading to a total culture chamber height of 143 μm. These values, already optimized in a previous work [94], correspond to a nominal strain level of -30%, calculated through equation 2.1.1.

Other than the compression level, the height of the culture chamber also influences the aspect ratio of the central channels. This parameter, defined as the ratio between the height and the width of the channels, is proportional to the median lateral strain within the hydrogel [102]. In order to minimize the lateral strain and to obtain a confined compression, the aspect ratio should be as low as possible. A total culture chamber height of 143 μm allows to have an aspect ratio lower than 1, and can therefore be considered an acceptable value.

2.1.4   Lateral pillars design

The design of lateral pillars was optimized in order to limit the lateral displacement of the cell constructs and to achieve a confined compression. For this purpose, the pillars should be as thick as possible. On the other hand, thick pillars would increase the chance of air entrapment within the device upon the first medium injection into the lateral channels, which would lead to an impaired interface between the medium and the cell constructs and thus to a lack of nutrients. A T-shaped cross-section, thanks to its high area moment of inertia, was shown to be the ideal choice to limit the lateral displacement of the hydrogel without increasing too much the thickness of the pillars [94]. The cross-section and the dimensions of the lateral pillars are shown in Fig. 2.1.3. An angle equal to 63° was imposed between the lateral edge of the pillar (BC in Fig. 2.1.3) and the edge in contact with the hydrogel (AB in Fig. 2.1.3). In this way, the leakage probability during the hydrogel injection was reduced, by minimizing the contact angle between the advancing hydrogel and the lateral edge of the pillar according to the modified capillary burst valve model proposed by Huang *et al.* [88] (see section 1.5.1).
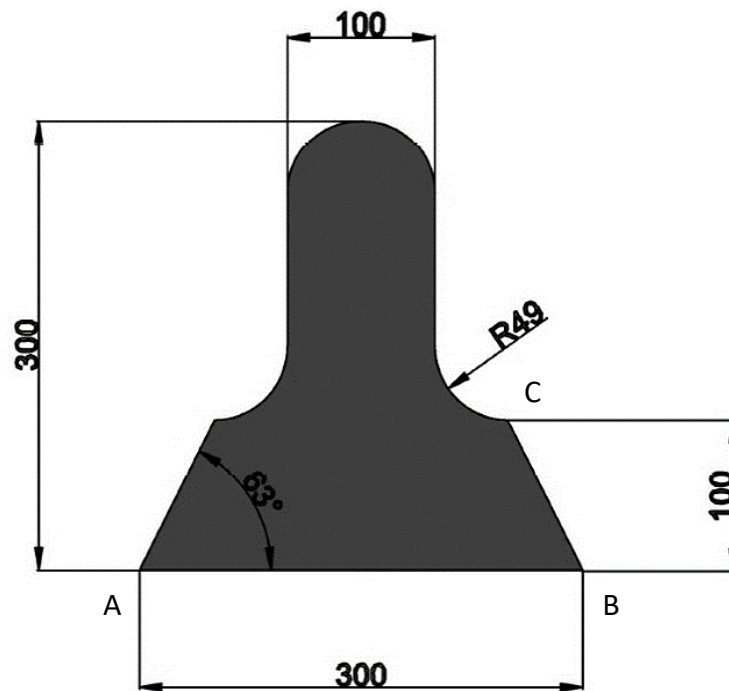
Fig. 2.1.3: *cross-section and dimensions of the lateral pillars. The measures are expressed in microns.*

The distance between two subsequent pillars was chosen based on the following considerations: wider spacings can impair a perfectly confined compression, and increase the chance of gel leakage into adjacent channels during the injection phase [88]; however, they are necessary to increase the interface between the cell constructs and the culture medium, and to allow the outflow of the fluid from the hydrogel during compression. Huang *et al.* [88] showed that the leakage probability was minimal for spacings up to 50 μm. Some devices similar to those used in the present work had already been tested in a previous study [94], and spacings of 30 μm between pillars were shown to represent the optimal trade-off between a confined compression and an adequate cell-medium interface. A final distance of 30 μm was therefore adopted. To verify the adequateness of the strain field within the hydrogel with this configuration, further analyses were conducted using a finite element method (see section 2.2).

2.2   Computational analysis

A computational analysis was performed, to assess the strain field in the device. Finite element modelling of the device was carried out using the software Abaqus/CAE 6.14 (SIMULIA™, Dassault Systèmes®).

A three-dimensional finite element model of the microfluidic device was developed to evaluate the strain field within the cell constructs. Both the symmetric and the asymmetric configurations of the device were considered. In order to reduce the computational cost of the

simulations, only a small region of the device was modelled, exploiting symmetries present in its geometry. The region of interest (ROI) considered in the model is shown in Fig. 2.2.1.
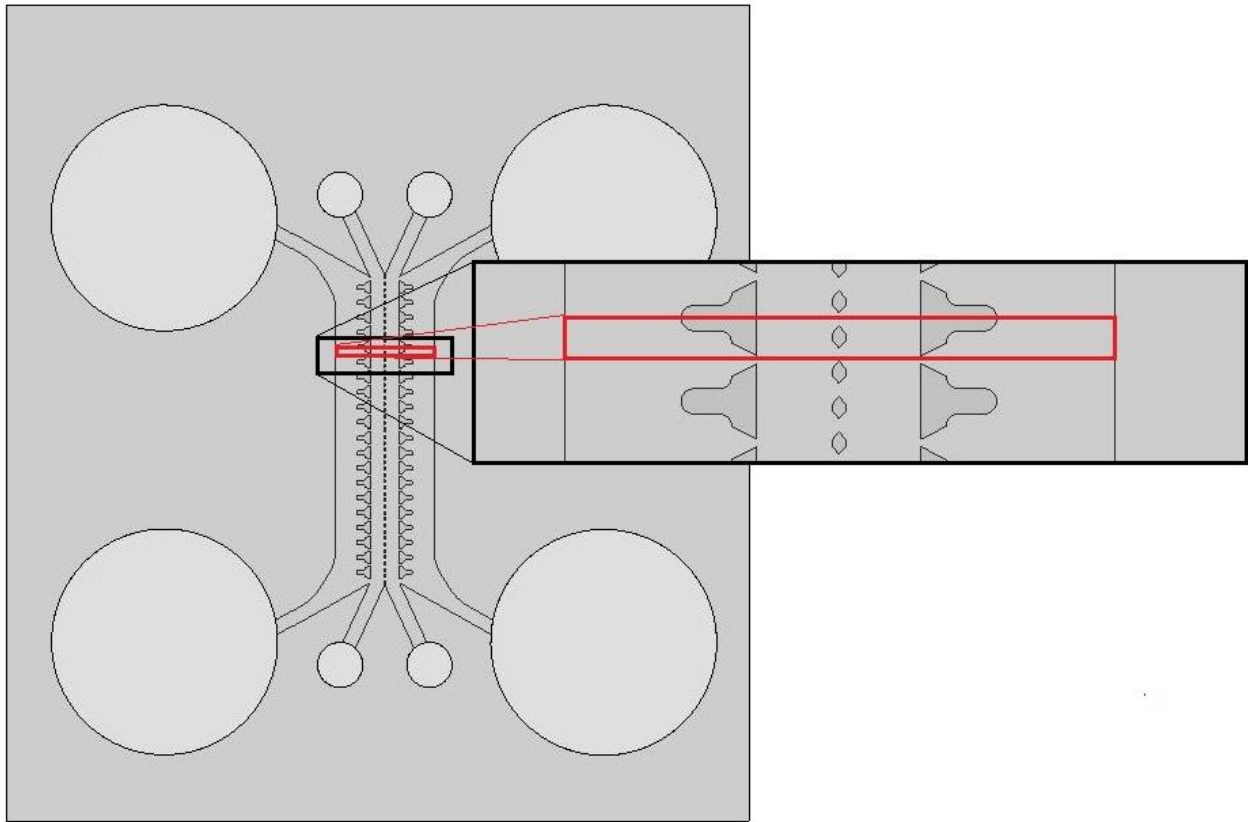
Fig. 2.2.1: *top view of the device, with detail of the region of interest considered in the model (in red).*

In detail, symmetry planes were introduced to cut in half the lateral pillars and the gaps between contiguous pillars. The hydrogels and the membranes were cut along the same planes. The final ROI had a thickness of 165 μm. The two hydrogels were modelled as a single 1050 μm wide, 143 μm high and 165 μm thick parallelepiped, with a hole in correspondence of the central pillar. A partition was created to allow the application of different mechanical properties to the hyaline cartilage and calcified cartilage compartments. The central pillar was modelled as an elliptic cylinder, with a minor axis of 50 μm along the X direction and a major axis of 90 μm along the Y direction. Only half of the T-shaped section of the lateral pillars was modelled, resulting in a L-shaped geometry. The shorter side of the L was 150 μm long and 100 μm thick, while the longer side was 300 μm long and 50 μm thick. The height of the pillars was either 100 μm or 143 μm, depending on the device configuration. The edges of the pillars in contact with the hydrogel were smoothed with a 10 μm radius to reduce geometric discontinuities. The membrane was modelled as a 2575 μm wide, 500 μm high and 165 μm thick parallelepiped. The geometries of the two device versions are shown in Fig. 2.2.2 and Fig. 2.2.3.
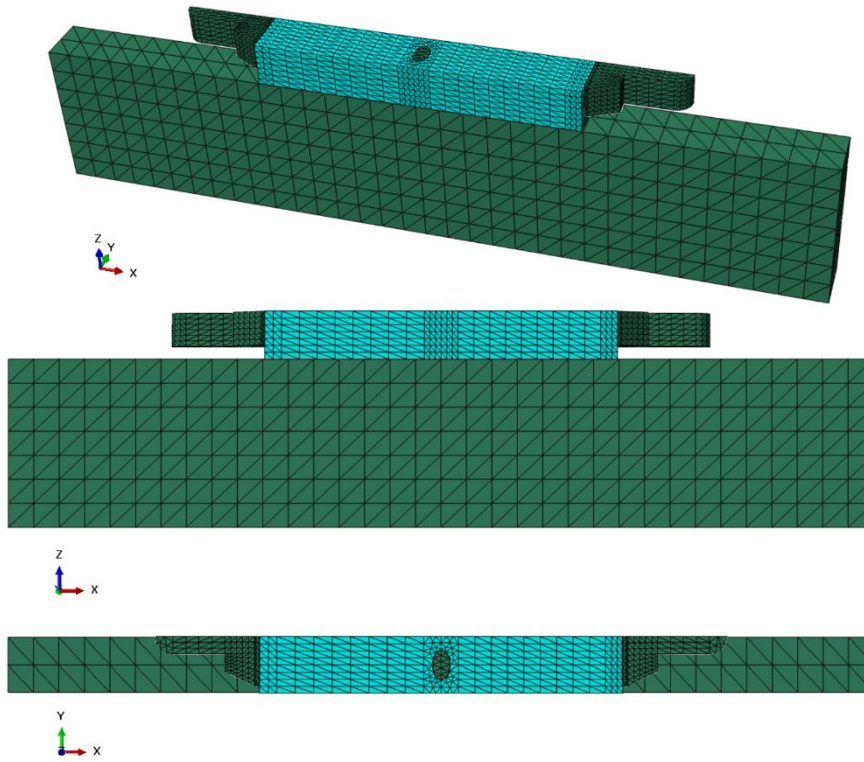
Fig. 2.2.2: *representative views of the ROI of the symmetric device. The pillars and the membrane are coloured in green, the hydrogels in blue.*
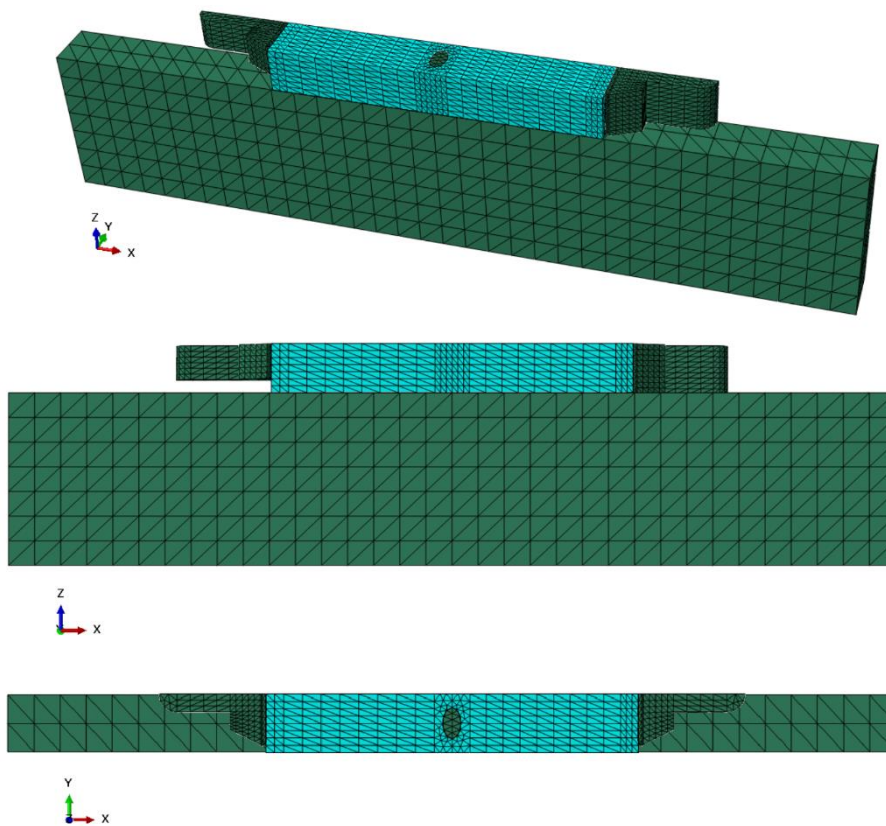
Fig. 2.2.3: *representative views of the ROI of the asymmetric device. The pillars and the membrane are coloured in green, the hydrogels in blue.*

MATERIALS AND METHODS

The PEG-based hydrogels were meshed using linear, coupled pore fluid/stress tetrahedral elements (C3D4P), while the pillars and the membrane were meshed using linear, hybrid, 3D stress tetrahedral elements (C3D4H). Hybrid elements are indicated in the Abaqus documentation for incompressible and quasi-incompressible materials, while coupled elements are needed to account for the poroelastic behaviour. An average element size of 20 μm was used for the hydrogels and the pillars, and it was increased to 50 μm in the regions far from the boundaries. The membrane was meshed using an element size of 75 μm, instead. A total of 23531 and 24926 elements were generated for the symmetric and the asymmetric device, respectively. A contact establishing step was introduced to initialize the contact and a pressure of 60 kPa was applied through a ramp at a 50 kPa/s loading rate. The loading step was modelled as a soil transient consolidation. A variable time step was used, with a minimum value of 10^{-9} s.

PDMS was described as a hyperelastic material; the general stress-strain relation for hyperelastic materials is:

$$S = 2\left(\frac{\partial W}{\partial I_1}I + \frac{\partial W}{\partial I_2}(I_1 I - C) + \frac{\partial W}{\partial I_3}I_3 C^{-1}\right) \qquad \textbf{\textit{2.2.1}}$$

where S is the Second Piola-Kirchhoff Stress, C is the Cauchy Tensor for strain, I is the identity matrix, W is the elastic energy and I_1, I_2 and I_3 are the first, second and third invariants of C respectively. The Mooney-Rivlin model, often used for rubber-like materials such as silicone, was adopted to describe the elastic energy function:

$$W = c_{01}(I_2 - 3) + c_{10}(I_1 - 3) + D(J - 1)^2 \qquad \textbf{\textit{2.2.2}}$$

where J is the Jacobian and c_{01}, c_{10} and D are material parameters. The values of c_{01}, c_{10} and D for PDMS were obtained from literature [103]: c_{10} was set equal to 254 kPa, c_{01} to 146 kPa while D was assumed equal to zero due to the material incompressibility.

The PEG-based gel was modelled as a Biphasic Poroelastic (BPE) material [104]. PEG-based hydrogels can display a wide range of mechanical properties. In particular, gels with a low polymer percentage, like the ones used in this work, have a Young modulus in the range between 1 and 100 kPa [105]. In order to consider the most potentially critical condition, the Young modulus was set equal to 100 kPa [95]: this is the worst case scenario, because the more the material is stiff, the more difficult it is for the membrane to reach the pillars and compress the hydrogels adequately. Poisson's ratio was set to 0.33 [95], [106]. The initial void ratio, defined as the ratio between the volume of voids and the volume of the solid part, was set equal to 55, considering a 2% w/v gel formulation (which corresponds to a 1.79% v/v formulation). The specific weight for the pore fluid was set to

9741 N/m^3. The permeability for 2% PEG was not found in literature, so a value of 10^{-14} m^2 was assumed, consistent with the one experimentally found by Offeddu *et al*. [107] for a 5% w/v PEG hydrogel. A lower polymer concentration should determine a slightly higher permeability. To assess the effect of this variation, a simulation was carried out doubling the permeability value (i.e., setting it to $2*10^{-14}$ m^2) while keeping all the other parameters constant. Once verified that the effects of this approximation were negligible, a value of 10^{-14} m^2 was adopted for all the following simulations. Instead of the permeability, Abaqus uses the hydraulic conductivity K to describe materials. To obtain a value for this parameter, the permeability was multiplied by the gravitational acceleration and divided by the cinematic viscosity of water, leading to the result K = $1.4*10^{-7}$ m/s.

The calcified cartilage construct was described using the same model adopted for the hyaline cartilage one. Only the Young modulus was changed, while keeping all the other parameters constant. Preliminary tests suggested that the calcified cartilage construct was nearly twice as stiff as the hyaline cartilage one, so the Young modulus E was set equal to 200 kPa. To evaluate the dependence of the strain on the mechanical properties of the hydrogel, simulations were also performed setting E equal to 150 and 100 kPa.

The contact between all the surfaces was modelled as frictionless, to represent perfect lubrication. The following boundary conditions were imposed: the vertical displacement of the top of the two hydrogels was set equal to zero; the top of the pillars and the lateral edges of the membrane were modelled as encastered; a zero pore pressure was imposed on the portions of the lateral edges of the hydrogels which were not in contact with the pillars; finally, a symmetry along the Y axis was imposed at the planes previously introduced to cut the device and reduce the ROI.

A mesh sensitivity analysis was conducted on the symmetric configuration of the device, in order to ensure the congruence of the solution. The data, shown in Fig. 2.2.4, refer to the displacement along the X direction of the bottom edge of the face of the hyaline cartilage construct in contact with the lateral pillar.
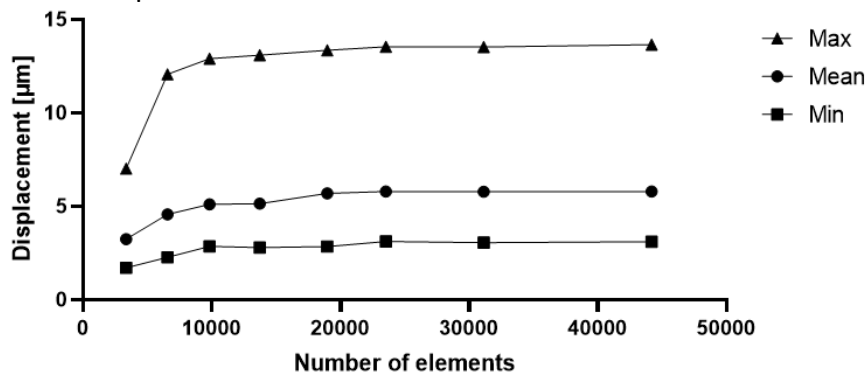
Fig. 2.2.4: *mesh sensitivity analysis. Mean, minimum and maximum displacement levels of the nodes of the bottom lateral edge of the hyaline cartilage construct are reported.*

2.3 Device production

Devices were realized through soft lithography techniques. Master molds were realized through photolithography, and replica molding was subsequently used to produce PDMS devices.

2.3.1 Master molds fabrication

The features of the devices, as optimized in section 2.1, were translated into masks for soft lithography (Fig. 2.3.1). Full size drawings of the culture chambers and the actuation chambers were realized using AutoCAD 2020 (Autodesk). Two separate drawings were made for the culture chamber, one for the pillar layer and one for the underlying gap. A total of three photomasks were produced, corresponding to pillars, gap, and actuation chamber, respectively. Drawings were printed at full size and high resolution (64000 dpi) on Mylar® Polyester Film, using a laser printer (MicroLithography Services Ltd., Essex, UK). No masks were needed for the bottom layer of the device, being its surface unpatterned. Nine culture chambers (three for each device version) were fitted into a single photomask. A single actuation chamber with three compartments connected to a single inlet was used for the three culture chambers of the same type, allowing the stimulation of three biologically independent samples in parallel, and minimizing the requirement of tubings and connections.

Master mold fabrication was performed by photolithography in the clean room at PoliFab, the micro- and nanotechnology centre of Politecnico di Milano, in an environment with a controlled number and size of polluting particles. SU-8 epoxy-based negative photoresist (Microchem, Newton, MA) was spin-coated onto 4-inch, polished silicon wafers. The features corresponding to the pillars and the gap were realized in the same wafer through multilayer photolithography, avoiding the necessity of aligning the layers during the production of each culture chamber, and increasing the accuracy of the whole process. First, the photoresist was spin-coated onto the wafer to match the desired height of the gap, namely 43 µm. The desired thickness of the photoresist layer was achieved by setting the spin rate of the wafer through previously made calibration curves. The gap mask was accurately put in soft contact with the wafer, to transfer the features onto the SU-8 coating. The photoresist was exposed to a collimated UV light beam through the photomask. The first mask was removed, and a second spin-coating of the photoresist was performed, obtaining a thickness corresponding to the desired pillar height (100 µm). The pillar mask was aligned with the gap layer, thanks to the specifically designed alignment signs. The SU-8 coating was again exposed to a collimated UV light beam through the photomask rendering. Regions of the negative

photoresist exposed to the UV light crosslinked and became insoluble. An organic solvent, called a developer, was used to dissolve the unexposed regions of the coating, leaving only the desired features on the surface of the wafer. An analogous procedure was used to realize the master mold for the actuation chamber.
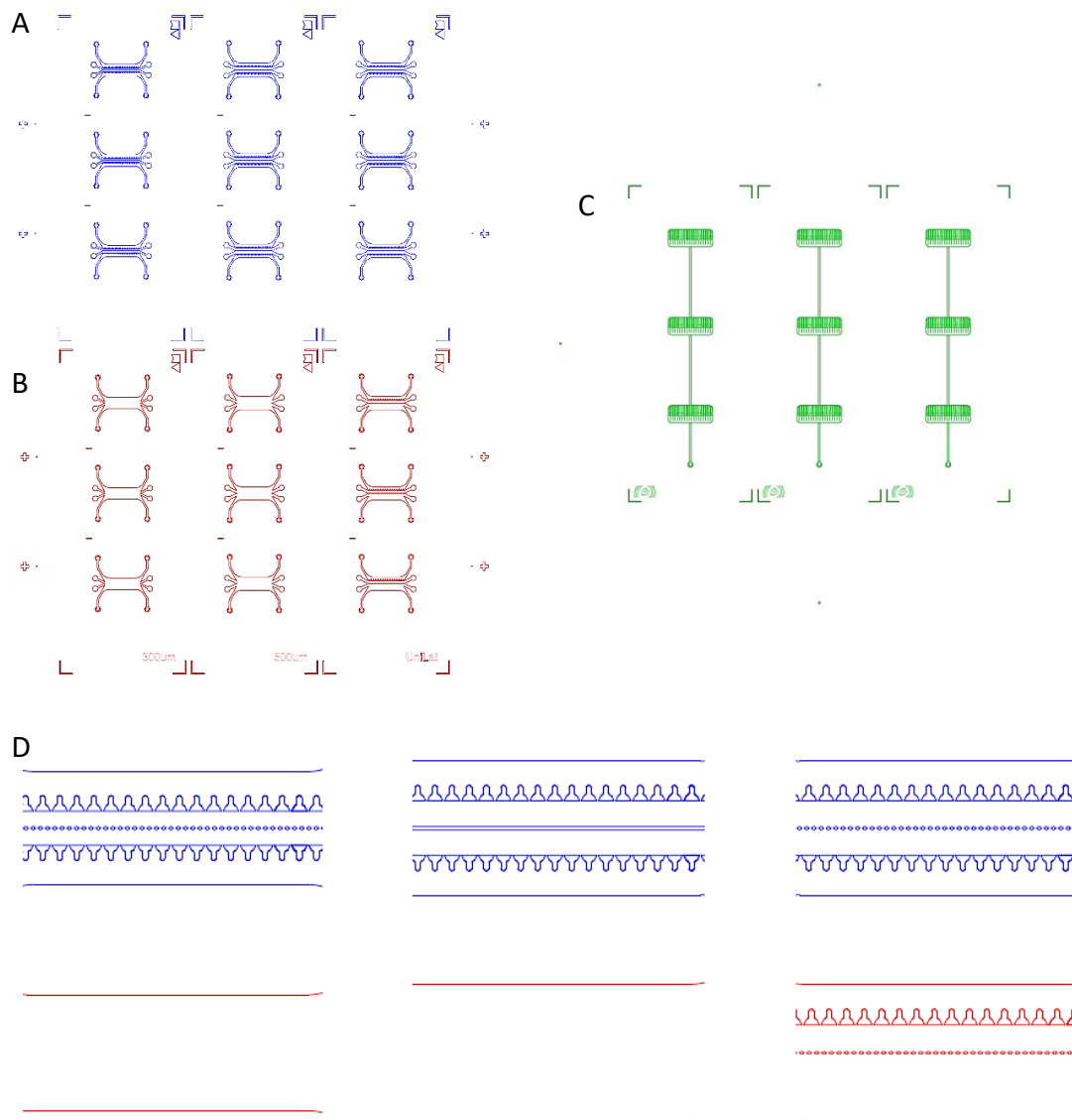
Fig. 2.3.1: *CAD drawings of the photomasks for the microfluidic devices. A) pillar layer; B) gap layer; C) actuation chamber. Alignment signs are visible on each layer; D) detail of the pillar layer (in blue) and the gap layer (in red) of the three different device versions (from left to right: Pillar, Wall, UniLat). In the UniLat version, the gap is present only on one side of the device, as previously discussed in section 2.1.1. Therefore, the lateral pillars on the other side and the central pillars had to be drawn also on the gap layer, in order for them to occupy the whole height of the culture chamber.*

2.3.2 Layers fabrication

The microfluidic device layers were fabricated in PDMS (SYLGARD® 184 SILICONE ELASTOMER KIT, Dow Corning, USA). The polymer was prepared by mixing the base and the curing agent at a w/w ratio of 10:1, as indicated by the producer. The two components were manually mixed with a spatula to obtain a homogeneous solution. The solution was degassed in a vacuum chamber at -0.8 bar for approximately 15 – 20 minutes, to remove air bubbles. After the degassing cycle, PDMS was poured onto the patterned master molds for the culture chamber (top layer) and the actuation chamber (middle layer), and onto a Petri dish for the floor of the device (bottom layer). To prevent PDMS from sticking to the master surface, a silanization treatment was performed before the first pouring phase. The master molds were exposed to trimethylchlorosilane gasses (TMCS, Sigma-Aldrich) for 30 minutes at room temperature. Operations were carried out under a chemical safety hood. Once PDMS had been poured on the master molds, another degassing cycle at -0.8 bar was performed. The polymer was allowed to reticulate on a levelled shelf at 65°C for two and a half hours. Afterwards, PDMS layers were carefully peeled off the molds. Each PDMS layer was cut and refined using a razor blade. The holes serving as reservoirs for culture medium and the inlets of the gel channels were realized in the top layer using biopsy punchers with a diameter of 5 mm and 1 mm, respectively. The top and middle layers were positioned on a glass Petri dish, with the patterned surface of the top layer and the unpatterned surface of the middle layer facing upwards. The Petri dish was inserted in a plasma cleaner (Harrick Plasma), where it was exposed to air plasma for 50 seconds. Following plasma activation, the top and the middle layers were carefully aligned and sealed together, enclosing the culture chamber. Afterwards, they were allowed to bond for 30 minutes at 65°C. The hole serving as an inlet for the actuation chamber was realized through both the top and the middle layer, using a biopsy puncher with a diameter of 0.5 mm. The bottom layer and the patterned surface of the middle layer were activated by plasma and sealed together, thus enclosing the actuation chamber. The device was left at 65°C for 30 minutes, to ensure water evaporation.

2.4 Device characterization

2.4.1 Geometrical characterization

A geometrical characterization of the devices was performed, verifying the correspondence between the actual dimensions of the features and the nominal ones. Three chambers were

measured for each version of the device. The culture chambers were cut with a razor blade, in order to obtain sections with a thickness of approximately 1 mm. Three sections were obtained from each culture chamber. Sections were observed through a compound microscope (AmScope T120C), and pictures at magnifications of 4x and 10x were taken using a camera (AmScope MU500) connected to the microscope. Fig. 2.4.1 shows a representative section.

Fig. 2.4.1: section of the top layer of the device. Scale bar 100 µm.

Pictures were analysed through the software ImageJ. The height of the pillars and gap was measured. Values in pixels were converted to microns using a calibration image. To reduce the operator-related errors, three measurements were taken for each picture, leading to a total of 27 measurements for each version of the device. The measures were averaged, and the standard deviation (SD) was calculated. The strain ε was calculated through equation 2.1.1, to verify that the devices were able to produce a compression close to the desired one. It should be noted that ε was calculated accounting only for the geometrical features of the devices, and not for material properties.

2.4.2 Determination of the optimal actuation pressure

The actuation pressure, i.e., the pressure required to make the actuation membrane abut against the pillars, was determined using a method previously described by Lemme and Conficconi [102]. A stainless-steel coupler with an internal diameter of 0.5 mm and an external diameter of 0.7 mm was inserted into a Tygon tube (Qosina) with an internal diameter of 0.5 mm and an external diameter of 1.5 mm. A 23 G hypodermic needle (Instech Laboratories, Inc) was inserted into the

other extremity of the tube. The hub of the hypodermic needle was connected to a 1 ml syringe (Terumo), and the syringe was used to aspirate nonsterile PBS into the tube. The tube was filled almost completely, but taking care to leave a visible interface between PBS and air. The coupler was connected to the actuation chamber through a hole specifically realized in the device. The needle hub was removed from the syringe and connected to a pressure regulator. A relative pressure of 300 millibars was applied to the actuation chamber for 30 – 45 minutes, in order to remove the air bubbles present in the chamber and to fill it completely with PBS. The filling procedure was monitored through a compound microscope with a 4x magnification.

Once all the bubbles were removed from the actuation chamber, the pressure was set to zero. A hydrophobic blue dye was injected in the culture chamber using a micropipette (WPI Eagle E100). Pressure was gradually increased from 0 to 500 millibars by steps of 50 millibars. At every increment, a picture of the culture chamber was taken through the camera-connected microscope.

Images were analysed through the software ImageJ. All the images referring to the same device were opened as a stack. For each picture, a rectangular area inside one pillar was manually selected and the mean grey value was measured. The mean grey value is a measure of the colour intensity: it adopts an 8-bit scale in which 0 corresponds to black and 255 corresponds to white. This parameter was correlated with the displacement of the actuation membrane: at rest condition, the dye filled the gap underneath the pillars, which therefore appeared blue (Fig. 2.4.2). As pressure increased, the gap tightened and the amount of dye below the pillars diminished. As a consequence, the colour intensity started increasing and the pillars appeared light blue (Fig. 2.4.3). When the membrane abutted against the pillars, no dye at all was present anymore below them, and therefore they appeared completely white (Fig. 2.4.4). A further increase in pressure did not produce an increase in colour intensity, which therefore reached a plateau.

The obtained mean grey level values were normalized, subtracting the colour intensity at 0 millibars and dividing by the intensity at 500 millibars. In this way, a 0 – 100 scale was created. Three Pillar and three UniLat devices were considered. The normalized grey values referring to the two device versions were averaged and plotted against pressure. The actuation pressure was defined as the one in correspondence of the beginning of the plateau.
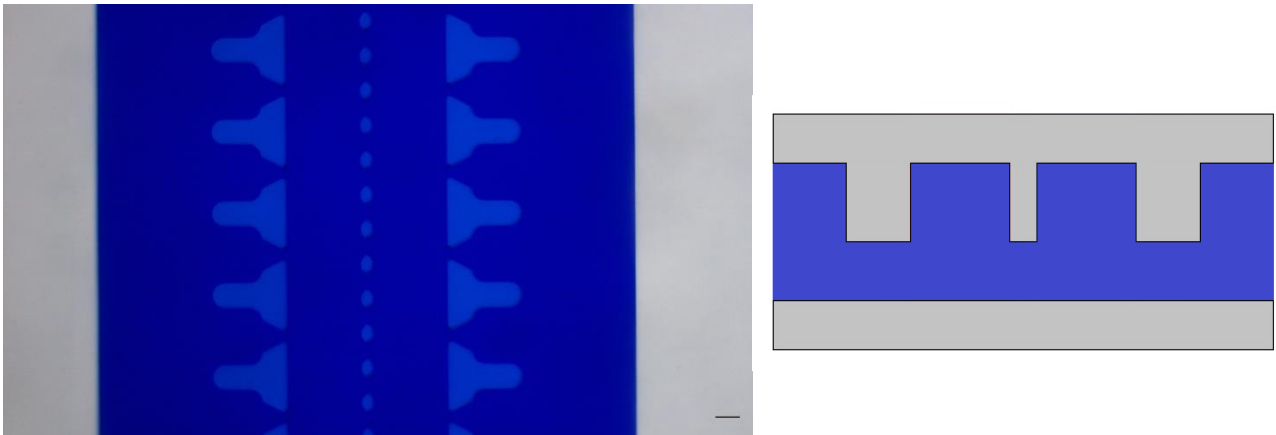
Fig. 2.4.2: *left: top view of the culture chamber filled with a blue dye, at a relative pressure of 0 millibars. The pillars appear blue due to the dye present in the gap underneath them. Scale bar 100 μm; right: scheme of the culture chamber cross section at rest.*
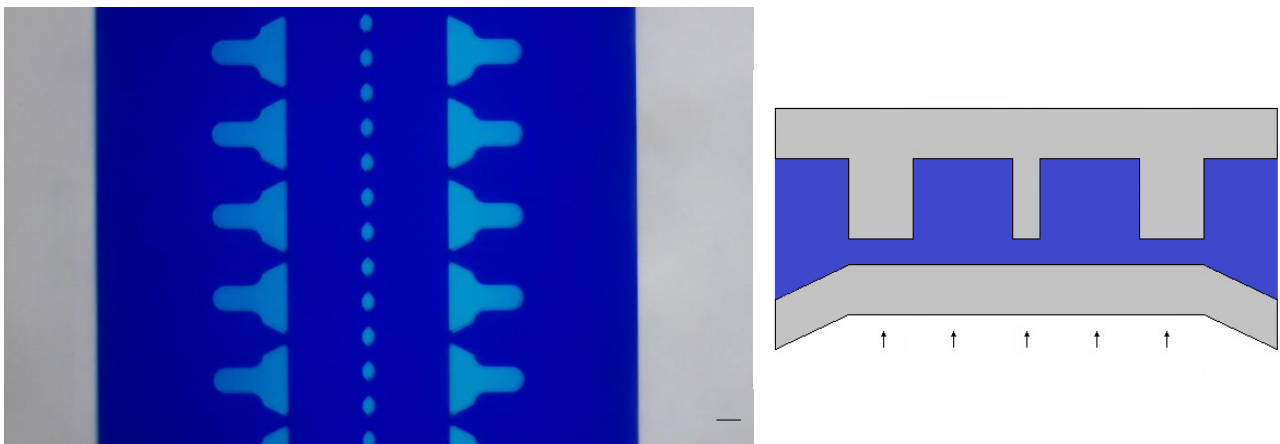
Fig. 2.4.3: *left: top view of the culture chamber filled with a blue dye, at a relative pressure of 150 millibars. The dimension of the gap diminishes, so the pillars appear lighter. Scale bar 100 μm; right: scheme of the culture chamber cross section at a relative pressure of 150 millibars.*
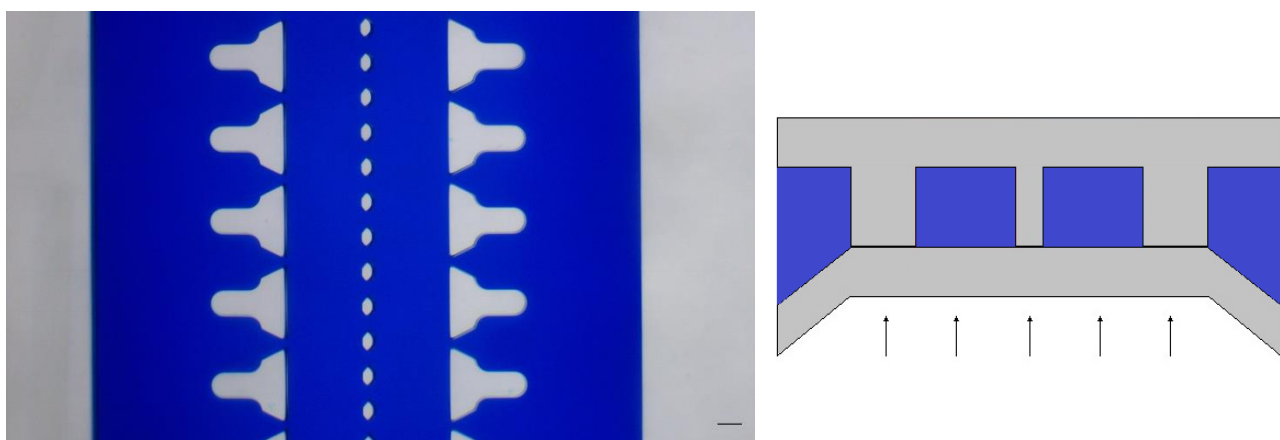
Fig. 2.4.4: *left: top view of the culture chamber filled with a blue dye, at a relative pressure of 500 millibars. There is no more dye below the pillars, so they appear white. Scale bar 100 μm; right: scheme of the culture chamber cross section at a relative pressure of 500 millibars.*

After all the measures had been taken, the devices were cut using a razor blade, to obtain sections with an approximate thickness of 1 mm. The blue dye was removed with a paper towel, and a picture of each section was taken through the camera-connected microscope, at a magnification of 4x. The pictures were then processed, measuring the thickness of the actuation membranes. The values in pixels were converted to microns using a calibration image. A previous study [94] on a device similar to the ones used in the present work showed that a minimum membrane thickness of 750 μm made the actuation pressure independent of the presence of the hydrogel inside the culture chamber. Therefore, since the membranes used in this work were thicker than that minimum value, the actuation pressure was only evaluated in the absence of the gel.

2.5 Biological validation

2.5.1 Sterilization and long-term sterility maintenance

A sterile environment is a fundamental requirement to maintain long term *in vitro* cell cultures without any contaminations. For this reason, microfluidic devices, instruments which could come in contact with cells, and components necessary for the mechanical actuation were sterilized prior to use. Microfluidic devices were placed in autoclave bags (ULTRA Pouch system, Amcor) and sterilized in an autoclave (SterilClave 24 B HD, COMINOX) at 121°C for 30 minutes. Autoclave sterilization was proven not to alter the gas permeability and the long-term hydrophobicity of PDMS, although it might produce a slight increase in its mechanical properties [75], [108]. After autoclavation, the bags containing the devices were stored at 65°C overnight to allow a complete restoral of their hydrophobicity. Before cell seeding, autoclave bags were opened in a biosafety cabinet, and the devices were moved into sterile Petri dishes. Petri dishes guarantee a long-term maintenance of the sterility of their content, thanks to the tortuous path present between the dish and its cover. All the operations requiring to open the Petri dishes and to have a direct contact with the microfluidic devices (e.g., culture medium change) were performed in a biosafety cabinet to avoid contaminations.

After use, all the plasticware that came in contact with biological material was disposed in specific containers for biohazardous waste. All the non-disposable tools (e.g., scissors, tweezers) were immersed overnight in a 1.5% solution of Sekusept™ PLUS (Ecolab) in distilled water, rinsed with sterile bi-distilled water (passed through a 0.2 μm pore filter) and sterilized via autoclave.

2.5.2 Cell expansion

HACs and MSCs at passage 2 – 3 were defrosted and expanded through the following procedure. Cryovials filled with cells suspended in dimethyl sulfoxide (DMSO) were extracted from liquid nitrogen tanks at -196 °C, and placed into a 37°C water bath for one minute to allow cell thawing. At room temperature, DMSO has a cytotoxic effect, therefore the cell suspensions had to be quickly diluted with pre-heated complete medium (CM). For HACs, the complete medium consisted in High Glucose Dulbecco's Modified Eagle Medium (DMEM, Gibco™, Thermo Fisher Scientific) supplemented with 10% Fetal Bovine Serum (FBS, Hyclone Laboratories, Inc.), 1% Sodium pyruvate 100 mM (Gibco™, Thermo Fisher Scientific), 1% 4-(2-hydroxyethyl)-1-piperazineethanesulfonic acid 1M (HEPES, Gibco™, Thermo Fisher Scientific) and 1% PSG (100 U/ml Penicillin, 100 μg/ml Streptomycin, 29.2 mg/ml L-glutamine in a 10 mM citrate buffer, Gibco™, Thermo Fisher Scientific). For MSCs, the complete medium consisted in Minimum Essential Medium α (MEM α, Gibco™, Thermo Fisher Scientific) supplemented with 10% FBS, 1% Sodium pyruvate 100 mM, 1% HEPES 1M and 1% PSG. After dilution, the cell suspensions were centrifuged at 1500 rpm for 3 minutes in a Heraeus™ Multifuge 3SR plus (Thermo Scientific). The medium was removed in order to eliminate the traces of DMSO, and cells were resuspended in CM supplemented with growth factors, namely 1 ng/ml TGF-β1 (R&D systems) and 5 ng/ml FGF-2 (R&D systems) for HACs, and 5 ng/ml FGF-2 for MSCs. Cells were plated in flasks at an initial density ranging from 5000 cells/cm^2 to 10000 cells/cm^2, and cultured at 37°C in a humidified atmosphere containing 5% CO$_2$. The culture medium was replaced every third day.

2.5.3 Device seeding

When cells reached 75% – 80% sub-confluency, they were detached from the flasks by trypsinization and seeded into the microfluidic devices. In detail, flasks were emptied of the culture medium and washed thoroughly with sterile PBS, in order to eliminate all the traces of FBS, which would inhibit trypsin activity. PBS was removed and each flask was added with 4 ml Trypsin-EDTA 0.05% (Gibco™, Thermo Fisher Scientific), before being incubated for 5 minutes at 37°C in a humidified atmosphere with 5% CO$_2$. Trypsin action was blocked by adding 8 ml of FBS-containing CM in each flask. Cell detachment was checked using an inverted microscope (Nikon Eclipse TS100), by verifying the shift from a spread to a round cell morphology. The cell suspension was transferred into a 50 ml Falcon® tube (Corning Inc.) and centrifuged for 3 minutes at 1500 rpm. The supernatant

was discarded, taking care to conserve the cell pellet at the bottom of the tube, which was resuspended in a known volume of CM (approximately 1 ml per million cells).

For cell counting, a volume of 10 µl was withdrawn from the cell suspension and diluted 1:1 in Trypan Blue (Sigma-Aldrich). The obtained suspension was loaded into a haemocytometer and the number of living cells was counted directly through the inverted microscope. Through a proportion, the total number of cells in suspension was estimated. Cells were laden into enzymatically crosslinkable and cleavable eight-arm PEG hydrogels [99]. In detail, aliquots of cell suspension containing $1.25*10^6$ cells each were prepared in 600 µl sterile Eppendorf tubes. The tubes were centrifuged for 3 minutes at 1500 rpm and the supernatant was carefully removed. In order to obtain the desired density of $50*10^6$ cells/ml, a volume of gel solution equal to 25 µl was added to each cell aliquot. The gel solution consisted in Tris buffered saline (TBS, 50 mM, pH 7.6), added with 2% w/v Polymer precursor (a stoichiometrically balanced mixture of n-PEG-Gln and n-PEG-MMP-Lys), 50 mmol/l of $CaCl_2$ and 10 U/ml of thrombin-activated factor XIIIa. Each reagent was added sequentially to the solution and, after each addition, cells were resuspended to limit their aggregation and avoid inhomogeneities. Factor XIIIa, responsible for the crosslinking of n-PEG-Gln with n-PEG-MMP-Lys, was the last reagent to be added; after its addition, the cell laden gel solution was injected into the microfluidic devices through the specifically designed inlets. Devices were incubated for 15 minutes at 37°C in a humidified atmosphere with 5% CO_2, to allow the complete polymerization of the gel. For the devices hosting two cell constructs, this procedure had to be performed separately for the two gel channels. In this case, the HACs laden solution was injected first in the proper channel. Devices were incubated for 15 minutes at 37°C, and finally the MSCs laden solution was injected into the proper channel. The components for the PEG gel preparation were kindly provided by the Ehrbar Laboratory of Universitätsspital Zürich, where they were produced as previously described by the same group [99]. All the reagents were kept in a box filled with ice prior to and during use.

2.5.4 Cell culture

After the seeding phase, cells were cultured in a 3D environment for different time intervals, namely 7, 14 and 21 days, to assess the maturation of the cell constructs and the effect of the mechanical stimulation. Serum-free osteochondral medium (OCM) was used both for HACs and MSCs in single culture, and for the coculture of the two cell types. This medium consisted in High Glucose DMEM (Thermo Fisher Scientific™) supplemented with 1% HEPES 1M (Gibco™, Thermo

Fisher Scientific), 1% Sodium pyruvate 100 mM (Gibco™, Thermo Fisher Scientific), 1% PSG (Gibco™, Thermo Fisher Scientific), 1% ITS+1 Liquid Media Supplement 100x (1.0 mg/ml bovine insulin, 0.55 mg/ml human transferrin, 0.5 µg/ml sodium selenite, 50 mg/ml bovine serum albumin and 470 µg/ml linoleic acid, Sigma-Aldrich), 1% Human Serum Albumin 100x (HSA). OCM was further added with differentiation factors, namely 10 ng/ml TGF-β3, Dexamethasone 10^{-7} M, β-Glycerophosphate 10 mM and ascorbic acid 0.1 mM. Chondrogenic medium (CHM) was used for some controls. This medium had the same composition of OCM, but without β-Glycerophosphate.

The lateral channels of the devices were filled with medium through the following procedure: first, a 1.25 ml micropipette filtered tip was cut through sterile scissors, in order to enlarge the point to a size that would fit the medium reservoirs present in the devices (5 mm in diameter). The tip was press-fitted into one reservoir and the medium was forced to fill the whole channel. The procedure was repeated for all the reservoirs on one side of the device, then the reservoirs on the other side were filled as well. The Petri dishes containing the microfluidic devices were wetted with a 0.25 µg/ml Fungizone (Amphotericin B from *Streptomyces* sp., Sigma-Aldrich) solution for the double purpose of avoiding excessive medium evaporation and preventing mycotic contaminations. Devices were incubated at 37°C in a humidified atmosphere containing 5% CO_2. Culture medium was changed every second day. Starting from day 14, the waste medium was collected and kept at -80°C for further analyses.

2.5.5　Mechanical stimulation

After 14 days of static culture, the devices requiring mechanical stimulation were moved into custom modified 4-wells rectangular dishes (Thermo Scientific Nunc™) using sterile tweezers. Tygon tubes connecting the devices to the pressurized air source, necessary for the actuation, would prevent the correct closure of the dishes, hindering the maintenance of sterility. To solve this problem, the side of each well of the dish was punched with a 23 G needle previously heated on a Bunsen Beak. Tygon tubes were forced into each hole, and the interfaces were sealed with PDMS gaskets. The Tygon tubes connecting the inside of the dishes with their outside were filled with sterile PBS using a 1 ml syringe, and coupled to the actuation chambers of the respective devices. The syringe was removed, and the outer extremity of each tube was connected to a 0.22 µm pore filter (Sarstedt Filtropur S 0.2), in turn coupled to a three-way stopcock. Four stopcocks were connected in a row, to allow the stimulation of up to four devices in parallel. Stopcocks were connected to a pressure regulator and a pressurized air source. The setup is shown in Fig. 2.5.1.
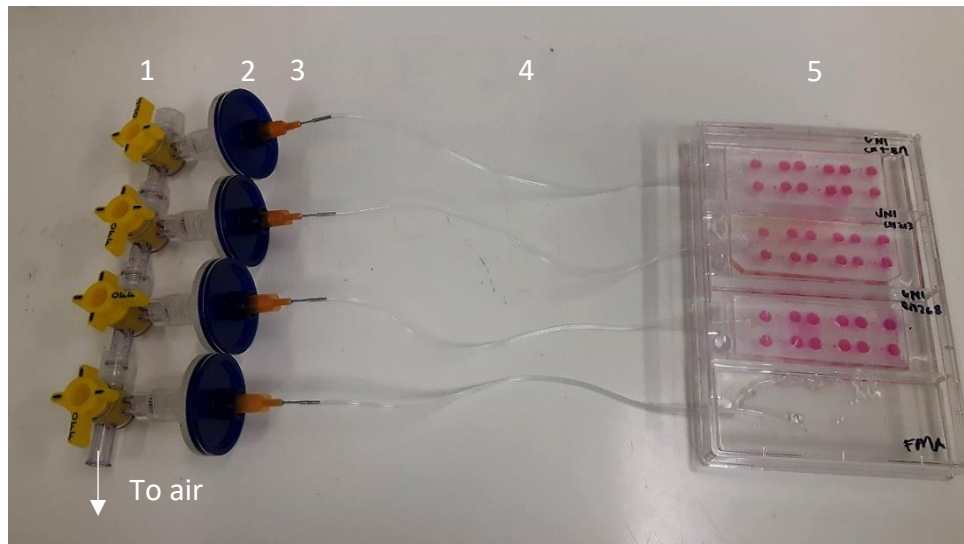
Fig. 2.5.1: *mechanical stimulation setup, designed to guarantee the maintenance of sterility. 1) three-way stopcocks; 2) filters; 3) hypodermic needles; 4) Tygon tubes; 5) microfluidic devices.*

A relative pressure of 300 millibars was applied for 45 minutes, in order to remove air from the actuation chambers of the devices and to fill them completely with PBS. During the filling phase, the devices were placed in an incubator at 37°C in a humidified atmosphere with 5% CO_2, to guarantee optimal conditions for cells. Once the filling phase was complete, the pressure was set to zero for 30 minutes, to avoid an excessive stress for cells. A previously developed automated controller [94] was inserted downstream the pressure regulator and upstream the three-way stopcock battery. The controller allowed to provide the devices with different actuation pressures, stimulation frequencies and regimens. In particular, the selected stimulation regimen, shown in Fig. 2.5.2, consisted in 2 hours of stimulation at 1 Hz, followed by 4 hours of pause, 2 further hours of stimulation and 16 further hours of pause. This regimen, resembling an average daily walking routine [95], was applied every day for a week. The adopted actuation pressure is discussed in section 3.4.2.

Fig. 2.5.2: *a complete cycle of the stimulation regimen adopted for mechanical compression.*

2.6 Maturation of a calcified cartilage construct

A characterization of calcified cartilage constructs in single culture was performed. The maturation of calcified cartilage constructs from MSCS was assessed. For this purpose, a pre-existing microfluidic platform [94] was used. The design and the functioning of this device, hereinafter referred to as "uKnee", were similar to the ones of the devices developed in the present work, with the difference that the uKnee had a single gel channel, and therefore was capable of hosting only one cell construct.

Bone marrow derived MSCs were laden in 2% w/v PEG gels at a concentration of $50*10^6$ cells/ml and seeded into the devices through the procedure described in section 2.5.3. Static culture was carried on for 0, 7 and 14 days in OCM (see section 2.5.4), to assess the capacity of bone marrow derived MSCs to differentiate into hypertrophic chondrocytes and to produce a mature calcified cartilage construct. Matrix deposition and gene expression were studied at the different time points. n = 9 biologically independent samples from N = 3 different donors were considered. The outline of the experiment is shown in Fig. 2.6.1.
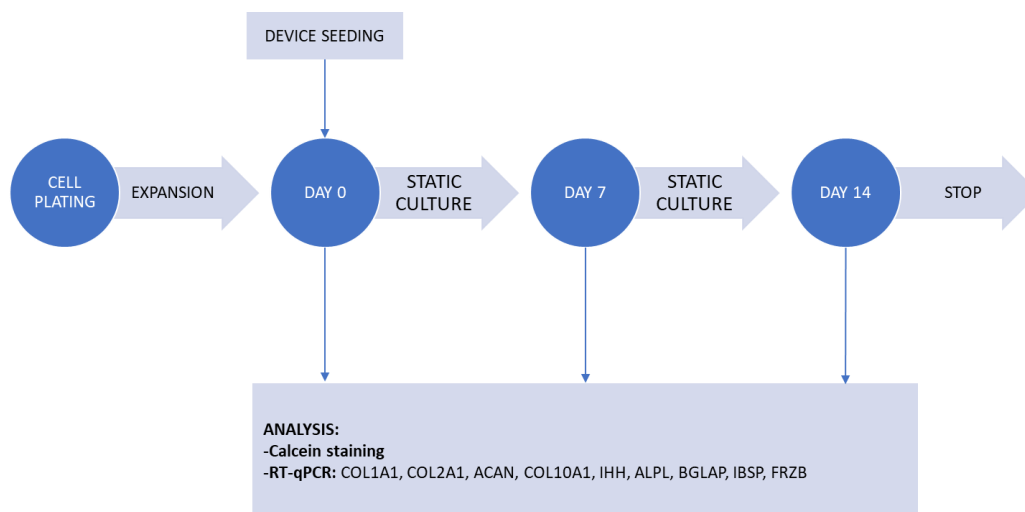
Fig. 2.6.1: *outline of the experiment performed to assess the development of a mature calcified cartilage construct.*

Phase contrast images of the devices were taken every second day as described in section 2.11.1, to assess tissue maturation and the overall cellular state. Deposition of calcium deposits was furthermore confirmed through Calcein staining, as described in section 2.11.2. MSCs cultured in CHM were used as negative controls. Gene expression at the different time points was analysed through quantitative reverse transcription-polymerase chain reaction (RT-qPCR), as described in section 2.11.3. The following genes were analysed to assess tissue maturation:

- COL1A1, encoding for Collagen type I alpha 1 chain, used as a marker of anabolism [95].

- COL2A1, encoding for Collagen type II alpha 1 chain, used as a marker of chondrogenesis and of chondrocyte-specific anabolism [95].

- ACAN, encoding for Aggrecan, a marker of chondrogenesis [95].

- COL10A1, encoding for Collagen type X alpha 1 chain, a protein expressed by hypertrophic chondrocytes [20].

- IHH, encoding for the Indian Hedgehog protein, a marker of chondrocyte hypertrophy [109].

- FRZB, encoding for the Frizzled related protein, a Wnt antagonist which inhibits chondrocyte hypertrophy [110].

- ALPL, encoding for the tissue-nonspecific Alkaline Phosphatase (ALP), a marker of mineralization and bone formation.

- BGLAP (Bone Gamma-Carboxyglutamate Protein), encoding for Osteocalcin, a marker of bone formation.

- IBSP (Integrin Binding Sialoprotein), encoding for Bone Sialoprotein 2, a marker of bone formation.

2.7 Effect of cyclic hyperphysiological compression on the calcified cartilage construct

The effect of cyclic hyperphysiological compression on calcified cartilage constructs was assessed. Bone marrow derived MSCs were laden in 2% w/v PEG gels at a concentration of $50*10^6$ cells/ml and seeded into uKnee devices through the procedure described in section 2.5.3. Static culture was carried on for 14 days in OCM (see section 2.5.4). Mechanical stimulation was started at day 14 as previously described in section 2.5.5, and dynamic culture was carried on for 7 days until day 21. Briefly, the stimulation regimen consisted in 2 hours of 30% compression at 1 Hz, followed by 4 hours of pause, 2 further hours of stimulation and 16 further hours of pause. Static controls were cultured for 21 days and their gene expression was compared to the one of cell constructs subjected to mechanical stimulation. n = 9 biologically independent samples from N = 3 different donors were considered.

The following pool of genes was analysed through RT-qPCR as described in section 2.11.3, to quantify the effect of cyclic hyperphysiological compression on cell constructs:

- COL1A1, as a marker of anabolism.

- COL2A1, as a marker of chondrogenesis.

- ACAN, as a marker of chondrogenesis.

- MMP13, encoding for matrix metalloproteinase 13, used as a marker of catabolism [95].

- CXCL8 (C-X-C Motif Chemokine Ligand 8), encoding for Interleukin-8, a marker of inflammation [95].

- COL10A1, as a marker of hypertrophy.

- IHH, as a marker of hypertrophy.

- GREM1, encoding for the protein Gremlin1, which inhibits chondrocyte hypertrophy and acts as a BMP antagonist in the TGF-β signaling pathway [110].

- DKK1, encoding for Dickkopf-related protein 1, a Wnt antagonist used as a marker of hypertrophy inhibition [110].

- FRZB, as a marker of hypertrophy inhibition.

- ALPL, as a marker of mineralization.

- BGLAP, as a marker of bone formation.

- IBSP, as a marker of bone formation.

- LECT1 (Leukocyte cell derived chemotaxin 1), encoding for Chondromodulin-1, an antiangiogenic factor which contributes to keep cartilage avascular [22].

Culture medium was changed every second day for the whole duration of the experiment, and phase contrast images of the devices were taken every second day as described in section 2.11.1. An outline of the experiment is shown in Fig. 2.7.1.
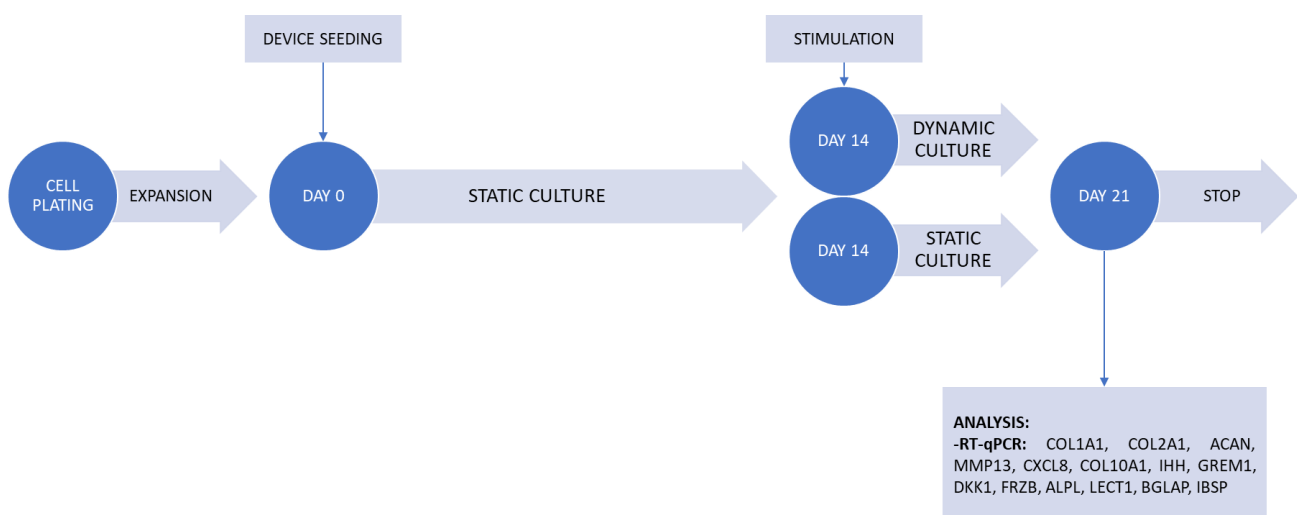
Fig. 2.7.1: *outline of the experiment performed to assess the effect of cyclic hyperphysiological compression on the calcified cartilage construct.*

2.8   Biological validation of the strain produced by the device

The strain produced by the newly developed devices was validated. Bone marrow derived MSCs were laden in 2% w/v PEG gels at a concentration of $50*10^6$ cells/ml, and seeded into a UniLat device, in the channel designed to host calcified cartilage. The other gel channel of the device, designed to host hyaline cartilage, was filled with a 2% w/v PEG gel without any cells. The injections were performed through the procedure described in section 2.5.3. Static culture was carried on for two weeks in OCM (see section 2.5.4). At day 14, mechanical stimulation was started as described in section 2.5.5, and protracted for one further week. Gene expression at day 21 was compared to the one of constructs cultured for three weeks in static conditions, to verify that the unwanted strain induced by the UniLat device in the calcified cartilage construct (discussed in section 3.2) did not induce phenotypical changes.

Another experiment was performed to validate the strain produced by the Pillar version of the device. HACs were laden in 2% w/v PEG gels at a concentration of $50*10^6$ cells/ml, and seeded into uKnee devices and in both gel channels of a Pillar device. The injections were performed through the procedure described in section 2.5.3. Static culture was carried on for two weeks in OCM (see section 2.5.4). At day 14, the Pillar device and the uKnee device were subjected to mechanical stimulation as described in section 2.5.5, and cultured in dynamic conditions for one additional week. Constructs cultured in static conditions up to day 21 were used as controls. Gene expression at day 21 was compared among the three experimental groups.
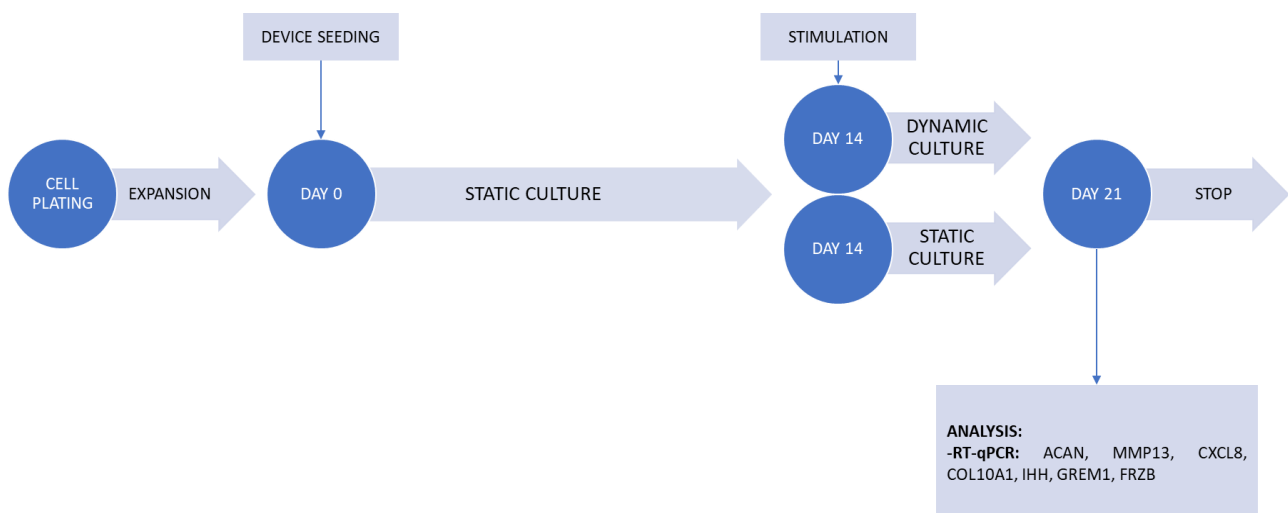

Fig. 2.8.1: *outline of the experiments performed to validate the compression levels produced by the devices.*

For both the experiments, ACAN, MMP13, CXCL8, COL10A1, IHH, GREM1, and FRZB were analysed through RT-qPCR, as described in section 2.11.3. n = 3 biological samples from N = 1 donor

were considered for each experimental condition. Culture medium was changed every second day for the whole culture period. An outline of the two experiments is shown in Fig. 2.8.1.

2.9   Development of a healthy osteochondral cell construct

The development of a mature healthy osteochondral cell construct was assessed in the newly developed devices. HACs and bone marrow derived MSCs were laden in 2% w/v PEG gels at a concentration of $50*10^6$ cells/ml and seeded into the devices through the procedure described in section 2.5.3. Wall and Pillar devices were used to generate the osteochondral constructs, in order to analyse which device version provided the best interface between hyaline and calcified cartilage. Single culture controls (i.e., seeded with MSCs only or HACs only) were considered to assess the effect of coculture. Static culture was carried on for 0, 7 or 14 days in OCM (see section 2.5.4). ECM composition and tissue maturation were analysed through immunofluorescence, as described in section 2.11.4.

Gene expression at day 0 and day 14 was analysed through RT-qPCR, as described in section 2.11.3. ACAN, COL10A1, ALPL, and IBSP were analysed. The constructs to be analysed by RT-qPCR were generated using HACs modified to express green fluorescent protein (GFP) as previously described [111], instead of normal HACs. Enzymatic digestion and fluorescence-activated cell sorting (FACS) were performed on the osteochondral constructs prior to RT-qPCR, to separate HACs and MSCs-derived hypertrophic chondrocytes. In detail, devices were emptied from culture medium at the end of the culture period and washed with sterile PBS. The bottom layer and the actuation membrane were peeled off, exposing the cell constructs. A 1.5% solution of Collagenase II (Worthington Biochemical Corporation) in DMEM (50% DMEM only + 50% CM, composed as described in section 2.5.2) was preheated at 37°C. Constructs were scraped using a micropipette tip and dissolved in 300 µl of the solution. Samples were left for 90 minutes at 37°C on an orbital shaker (Labnet GyroTwister), and vortexed vigorously every 15 minutes. After the digestion, 600 µl of CM were added to the samples to neutralize Collagenase. Samples were centrifuged at 1500 rpm for 3 minutes, and washed with 300 µl of FACS buffer, composed of 1mM EDTA (Sigma-Aldrich) and 2% FBS in PBS. Another centrifugation (1500 rpm for 3 minutes) was performed, then the samples were incubated with 300 µl of Trypsin-EDTA 0.05% for 2 minutes. Two more washing steps with FACS buffer were performed, and samples were centrifuged at 1500 rpm for 3 minutes after each step. Samples were moved into FACS tubes (Falcon® 5ml polypropylene round-bottom tubes, Corning Inc.), and sorted based on GFP expression using a BD FACSAria™ III SORP. 8 µl of MSCs laden

hydrogel were subjected to the same procedure and used to define the GFP-negative population during sorting.

Culture medium was changed every second day for the whole duration of the experiment, and phase contrast images of the devices were taken every second day as described in section 2.11.1. n = 6 biologically independent samples from N = 2 MSCs donors and n = 6 biologically independent samples from N = 1 HACs donor were considered for gene expression analysis. An outline of the experiment is shown in Fig. 2.9.1.
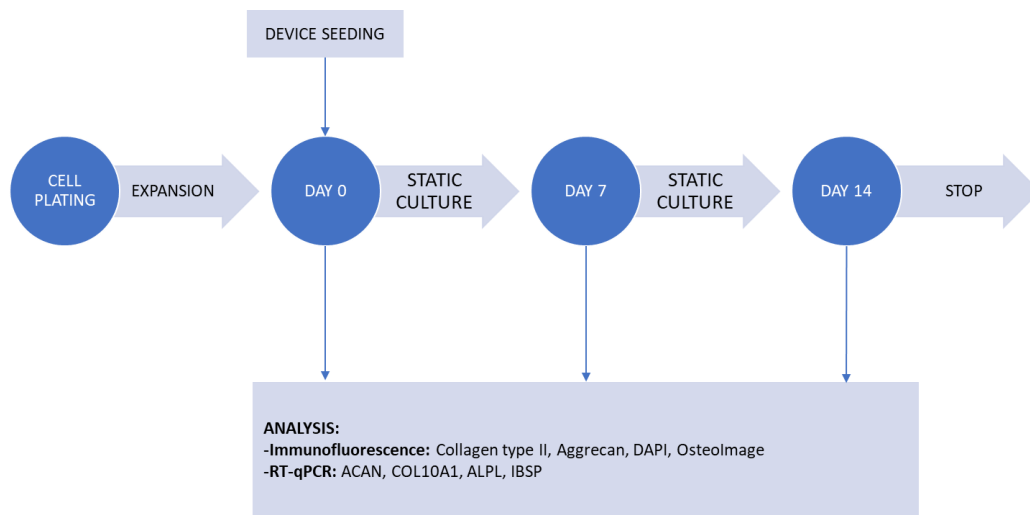
Fig. 2.9.1: *outline of the experiment performed to assess the development of a healthy osteochondral cell construct.*

2.10 Effect of cyclic hyperphysiological compression on the osteochondral construct

The effect of cyclic hyperphysiological compression on osteochondral cell constructs was assessed. GFP-expressing HACs and bone marrow derived MSCs were laden in 2% w/v PEG gels at a concentration of $50*10^6$ cells/ml and seeded into the devices through the procedure described in section 2.5.3. UniLat and Pillar devices were used to generate the osteochondral constructs. uKnee devices were seeded either with MSCs or HACs and used as single culture controls. Static culture was carried on for two weeks in OCM (see section 2.5.4). Mechanical stimulation was started at day 14 as previously described in section 2.5.5, and protracted until day 21. Static controls were cultured for 21 days and their gene expression was compared to the one of cell constructs subjected to mechanical stimulation. Culture medium was changed every second day, and phase contrast images of the devices were taken every second day as described in section 2.11.1. Gene expression for the different experimental conditions was analysed through RT-qPCR, as described in section 2.11.3.

Osteochondral constructs were subjected to enzymatic digestion FACS prior to RT-qPCR, as described in section 2.9. FRZB, MMP13 and CXCL8 were analysed for the hyaline cartilage compartment, while FRZB, BGLAP and ALPL were considered for the calcified cartilage compartment. Gene expression of constructs subjected to mechanical stimulation was normalized to the one of constructs belonging to the same experimental group (i.e., coculture or single culture) but cultured in static conditions. n = 6 biologically independent samples from N = 2 MSCs donors and n = 6 biologically independent samples from N = 1 HACs donor were analysed. Fig. 2.10.1 shows an outline of the experiment.
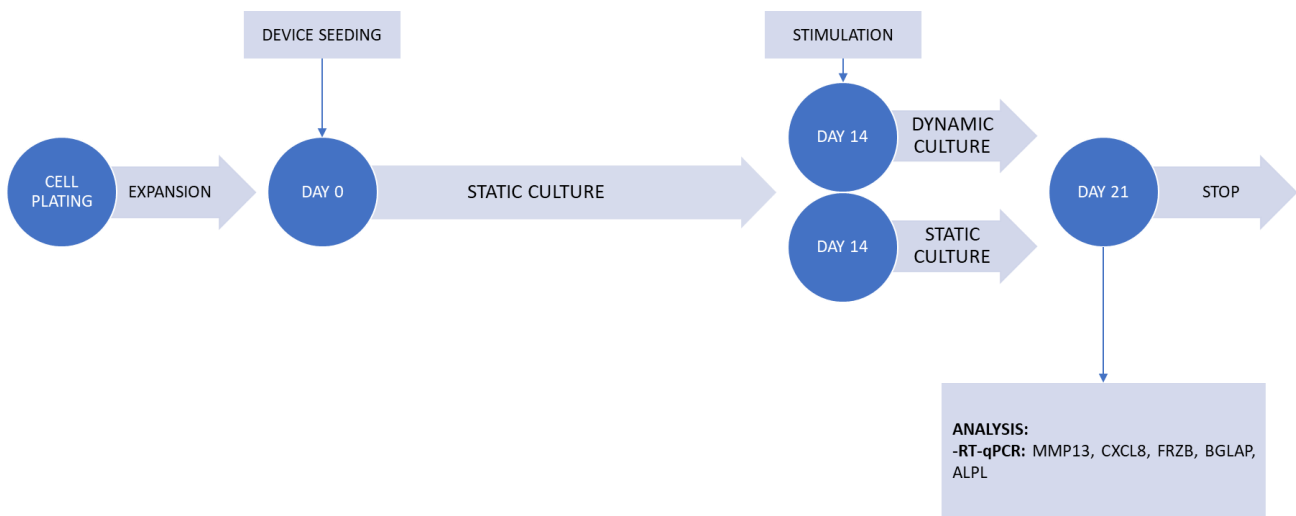
Fig. 2.10.1: *outline of the experiment performed to assess the effect of cyclic hyperphysiological compression on the osteochondral construct.*

2.11 Biological analysis

2.11.1 Phase contrast microscopy

Phase contrast images of the microfluidic devices were taken every second day during culture, to assess tissue maturation and the overall cellular state. The Petri dishes containing the microfluidic devices were extracted from the incubator, and pictures of the constructs at a 4x magnification were acquired through a camera connected to a phase contrast microscope (EVOS XL Core, Life Technologies).

2.11.2 Calcein staining

Constructs cultured in OCM or CHM were stained with Calcein, to assess the formation of calcium deposits in the ECM. 1 μg/ml of Calcein (Sigma-Aldrich) was added to the culture medium at day 5, 8 and 12 of static culture. Devices were incubated with Calcein-containing medium for two days. At day 7, 10 and 14 the medium was removed, and devices were rinsed with fresh Calcein-

free medium. 4x and 10x images of the devices were taken using a Nikon Eclipse Ti2 microscope and the Nikon NIS-Elements acquisition software. A 488 nm wavelength was adopted to excite Calcein. The fluorescent signal was detected and superimposed on a brightfield image of the cell construct. The same exposure time was used for samples cultured in OCM and CHM, and the intensity of the fluorescent signal was compared between the two experimental groups.

2.11.3 Gene expression analysis

RT-qPCR was used to quantify the changes in gene expression induced by tissue maturation and mechanical stimulation. At least n = 3 biologically independent samples were considered for each donor and experimental condition (i.e., different time points and stimulation conditions). The whole process consisted in three distinct phases, namely RNA isolation, reverse transcription, and the proper qPCR analysis.

i. RNA isolation: at the end of the culture period, the devices were emptied from the culture medium and washed with sterile PBS. In detail, the culture medium was removed from each reservoir using a micropipette. The reservoir at one extremity of each medium channel was filled with PBS, while the reservoir at the other extremity was left empty. PBS, driven by the hydraulic head, filled the whole channel, washing away the residual culture medium. After one minute, PBS was completely aspirated with a micropipette. The bottom layer and the actuation membrane of each device were peeled off, exposing the cell constructs. A 1.5 ml Eppendorf Safe-Lock tube containing 400 µl of Trizol (TRI Reagent®, Sigma-Aldrich) was prepared for each sample. 10 µl of Trizol were pipetted from the tube onto the central channel of the device, and cell constructs were mechanically disrupted using the tip of the pipette. The obtained cell homogenate was transferred back to the Eppendorf tube. The procedure was repeated on the membrane side of the actuation chamber, to retain possible cell construct residues. The tubes containing the samples were vortexed for 15 seconds using a Vortex-Genie 2 (Scientific Industries, Inc.), and centrifuged for 10 minutes at 12000g and 4°C in a Heraeus™ Biofuge Fresco (Thermo Scientific™). Samples were left at room temperature for 5 minutes, then 100 µl of chloroform (Sigma-Aldrich) were added to each tube. The tubes were shaken for 15 seconds before undergoing a resting period of 3 minutes at room temperature. Another centrifugation step, 12000g at 4°C for 15 minutes, determined the separation of the solution into three distinct phases: an organic phase at the bottom of the tube, containing proteins and lipids; a thin interphase, rich in DNA; an aqueous

phase at the top, containing RNA. The latter was carefully aspirated through a micropipette, and transferred to a new PCR-clean Eppendorf Safe-Lock tube. 200 µl of isopropanol (Merck EMSURE®) and 1 µl of glycogen (Roche Diagnostics GmbH) were added to each sample, to induce RNA precipitation. The tubes were shaken for 15 seconds, before undergoing a resting period of 10 minutes at room temperature. Another centrifugation step was performed, at 12000g and 4°C for 10 minutes. A pellet was visible at the bottom of each tube at the end of this process. The supernatant was discarded, taking care to conserve the pellet. The pellet was washed with 1 ml of 70% ethanol in Milli-Q water, and the solution was centrifuged at 12000g and 4°C for 5 minutes. The washing procedure was repeated twice, then the supernatant was removed and the cell pellet was resuspended in 20 µl of DNase/RNase-free water (Zymo Research). 1 µl of the solution was withdrawn and analysed through a Nanodrop One spectrophotometer (Thermo Scientific™). The spectrophotometer quantified the concentration of nucleic acids in the samples, as well the presence of protein and phenol contaminations. All the samples with an RNA concentration above 20 ng/µl were diluted with DNase/RNase-free water, to achieve a final concentration of 20 ng/µl.

ii. Reverse transcription: the SuperScript III Reverse Transcriptase Kit (Invitrogen) was adopted to retrotranscribe RNA into complementary deoxyribonucleic acid (cDNA). In detail, a 0.2 ml PCR Performance Tested tube (Sarstedt, Inc.) was prepared for each sample, and 1 µl of random primers was pipetted into each tube. 19 µl of RNA solution were withdrawn from each sample and added to the respective tube (in case the samples were not previously diluted, this value represented the whole volume of the solution). Samples were incubated with primers at 70°C for 10 minutes to straighten RNA, and they were put on ice immediately after to prevent refolding. During the incubation time, the Master Mix for the Reverse Transcriptase Reaction was prepared. This mix consisted in 0.5 µl of Reverse transcriptase (Superscript III 200 U/µl, Invitrogen), 0.5 µl of DNase/RNase-free water (Zymo Research), 2 µl of dNTP (deoxynucleotide triphosphates) mix 10mM, 6 µl of First-Strand Buffer 5x (present in the kit) and 1 µl of DTT (Dithiothreitol, present in the kit), for a total volume of 10 µl per sample. The Master Mix was added to the samples, and reverse transcription was performed through a Veriti 96-well Thermal Cycler (Applied Biosystems). Samples were subjected to a thermal program consisting in 10 minutes at 25°C, 60 minutes at 50°C and 15 minutes at 70°C. The obtained cDNA was stored at -20 °C or used immediately for qPCR.

iii. Quantitative real-time PCR: assays for gene expression quantification were prepared in a 96-well PCR plate (Sarstedt, Inc.). In detail, 5 μl of Taqman Gene Expression Master Mix (Thermo Fisher Scientific), 2.5 μl of DNase/RNase-free water and 0.5 μl of Assay on demand (a pre-formulated mixture of primers and fluorescent probes, specific for each gene of interest) were pipetted into each well. 2 μl of cDNA were added immediately before the analysis. The plate was sealed with a plastic cover, centrifuged at 2000 rpm for 1 minute and placed into a 7500 Fast Real-Time PCR System (Applied Biosystems), where it was subjected to 40 thermal cycles of 15 seconds at 95°C and 60 seconds at 60°C. A threshold level for fluorescence was imposed, and the threshold cycle (i.e., the thermal cycle at which the fluorescent signal reached the threshold level) was measured for each well. Expression levels of the genes of interest were normalized to the housekeeping gene glyceraldehyde-3-phosphate dehydrogenase (GAPDH). The relative gene expression was calculated as:

$$x = 2^{Ct_{GAPDH} - Ct_x}$$ ***2.11.1***

where Ct_{GAPDH} is the threshold cycle for GAPDH and Ct_x is the threshold cycle for the gene of interest. Two wells were considered for each sample, and the results were averaged. Excel 2019 (Microsoft Corporation) and GraphPad Prism 8 (GraphPad Software) were used for data analysis.

2.11.4 Immunofluorescence

Immunofluorescence was used to assess the maturation of the cell constructs. At the end of the culture period, the culture medium was removed from each reservoir of the considered devices using a micropipette. The reservoir at one extremity of each medium channel was filled with PBS, while the reservoir at the other extremity was left empty. PBS, driven by the hydraulic head, filled the whole channel, washing away the residual culture medium. After one minute, all the reservoirs were completely emptied, and the samples underwent fixation. A 4% solution of buffered formalin (Formafix Switzerland AG) was injected into the reservoir at one extremity of each medium channel. due to the hydraulic head, formalin filled the whole channel washing away the residual PBS. After one minute, the reservoirs were completely emptied and filled again with clean formalin. Devices were placed at 4°C overnight to allow the proper fixation of cell constructs. The following day, medium channels were washed with PBS, through the same procedure previously used to wash away culture medium. After the washing step, the bottom layer and the actuation membrane of the devices were peeled off, directly exposing the cell constructs to the staining solutions.

MATERIALS AND METHODS

Constructs underwent a permeabilization procedure. A 0.5% v/v solution of Triton™ X-100 for molecular biology (Sigma-Aldrich) in PBS was pipetted onto the samples and left there for 10 minutes. A blocking solution, consisting in PBS added with 0.3% v/v Tween® 20 for molecular biology (Sigma-Aldrich) and 3% v/v goat serum, was prepared. The solution was vortexed prior to use, to allow the complete solubilization of the components. The blocking solution was pipetted onto the samples and left there for 45 minutes at room temperature. The monoclonal antibodies mouse anti-human Collagen II IgG2a (Abcam, ab185430) and mouse anti-human Aggrecan IgG1 (Abcam, ab3778) were diluted in the blocking solution at a concentration of 1 µg/ml. The primary antibody solution was pipetted onto the samples, which were placed at 4°C overnight. The following day, samples underwent two washing steps with the blocking solution, each one lasting 10 minutes. A secondary antibody solution was prepared, adding the blocking solution with Alexa Fluor 546 goat anti-mouse IgG1 (Invitrogen, Thermo Fisher Scientific) and Alexa Fluor 647 goat anti-mouse IgG2a (Invitrogen, Thermo Fisher Scientific), at a concentration of 10 µg/ml. Samples were incubated with the secondary antibodies for 60 minutes at room temperature, and covered with an aluminium foil to prevent fluorophore bleaching. After the incubation, a 10 minutes long washing step with the blocking solution was performed. A 300 nmol/l DAPI (4',6-diamidino-2-phenylindole, Sigma-Aldrich) solution in PBS was added to the samples, and left there for 30 minutes, to stain cell nuclei. Subsequently, the constructs were stained with OsteoImage™ Mineralization Assay (Lonza), to assess the deposition of hydroxyapatite crystals. A washing solution (1:10 v/v solution of OsteoImage™ Wash Buffer in Milli-Q water), and a staining solution (1:100 v/v solution of OsteoImage™ Staining Reagent in OsteoImage™ Dilution Buffer) were prepared. Two washing steps with the washing solution were performed, each one lasting 5 minutes. Afterwards, the samples were incubated with the staining solution for 30 minutes at room temperature. Three more washing steps were performed, then the washing solution was removed, and the samples were conserved in PBS.

Confocal laser scanning microscopy (CLSM) was used to detect the fluorescence throughout the thickness of the constructs. Samples were posed on a microscopy glass slide and placed under a confocal microscope (Nikon A1R). Proper excitation wavelengths were adopted according to the employed fluorophores. Images at 20x magnification were taken using the Nikon NIS-Elements acquisition software.

2.12 Statistical analysis

Distribution normality was tested for each data group using Shapiro-Wilk test and Kolmogorov-Smirnov test. Data were considered as normal only if they passed both tests. Unpaired t-tests were performed to compare two data groups (i.e., two experimental conditions) in case of normal distributions, while Mann-Whitney tests were performed in case of non-normal distributions. An ordinary one-way ANOVA test with multiple comparisons was performed to compare three or more data groups with normal distributions, while Kruskal-Wallis tests and Dunn's multiple comparisons tests were used to compare three or more non-normal data groups. The significance level for all tests was $p < 0.05$. All the analyses were performed using the software GraphPad Prism 8.

3 RESULTS

Results of the design process, the computational analysis, the production and characterization of the devices, and their biological validation are presented. First, the device design was optimized, and a finite element model was adopted to evaluate the strain field within cell constructs. Secondly, the devices were produced and characterized, to guarantee their proper functioning and verify the accuracy of the fabrication process. Finally, the devices were used to generate mature osteochondral cell constructs and to assess the effect of cyclic hyperphysiological compression on the constructs.

3.1 Design of the microfluidic device

The final design of the device is shown in Fig. 3.1.1.
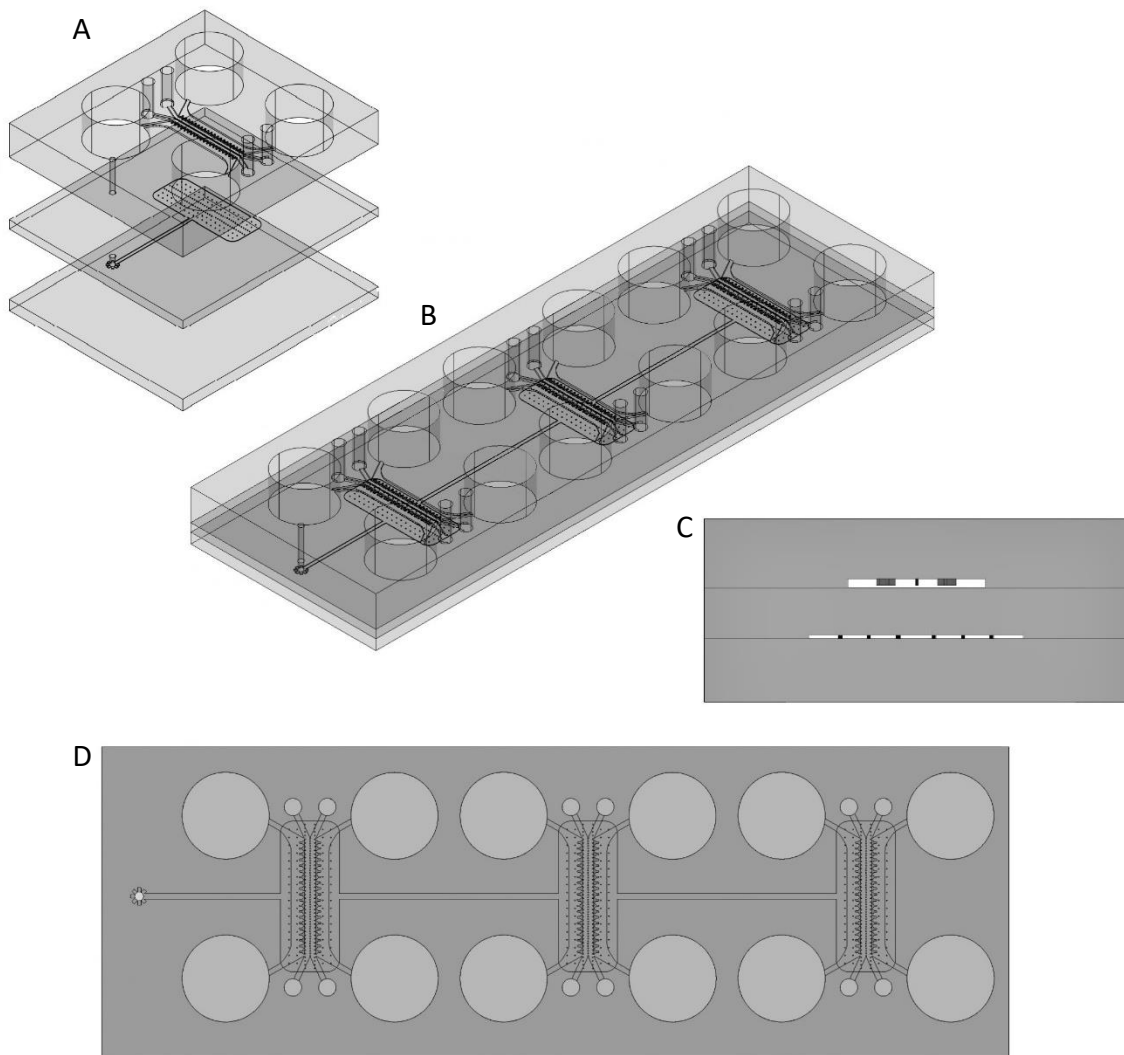
Fig. 3.1.1: *A) exploded view of the three layers composing the device (detail of a single functional unit, composed of a culture chamber and an actuation chamber); B) 3D view of the assembled device, comprising three flanked functional units; C) detail of the section of the culture chamber and the actuation chamber; D) top view of the assembled device.*

3.2 Computational analysis

The implemented finite element models of the device provided an evaluation of the strain field within the cell constructs.

Fig. 3.2.1 shows the results of the simulation for the symmetric device in terms of nominal strains. In the calcified cartilage construct, the strain along the Z direction (NE33) had a median value of -27.5%. The strain was homogeneously distributed in the whole region, as testified by a 75th percentile value of -28.4% and a 25th percentile value of -26.8%. The hyaline cartilage construct was slightly more compressed, being subjected to a median strain of -31.3%. Here too, the deformation was homogeneous (75th percentile value of -31.6%, 25th percentile value of -30.1%). As regards the strain along the X direction (NE11), peaks with a maximum value of 22.1% were found in the regions close to the openings between subsequent pillars, indicating an unwanted lateral expansion of the hydrogels. However, NE11 was low in most of the bulk volume: its median value was -0.8% in the hyaline cartilage construct and 1.7% in the calcified cartilage one, and the interquartile range (IQR, defined as the difference between the 75th and the 25th percentile) was 2.0% and 2.4% in the two compartments, respectively. The strain along the Y direction (NE22) was negligible within both the constructs, with a median value of 0.1% and an IQR of 0.6%.

A

B
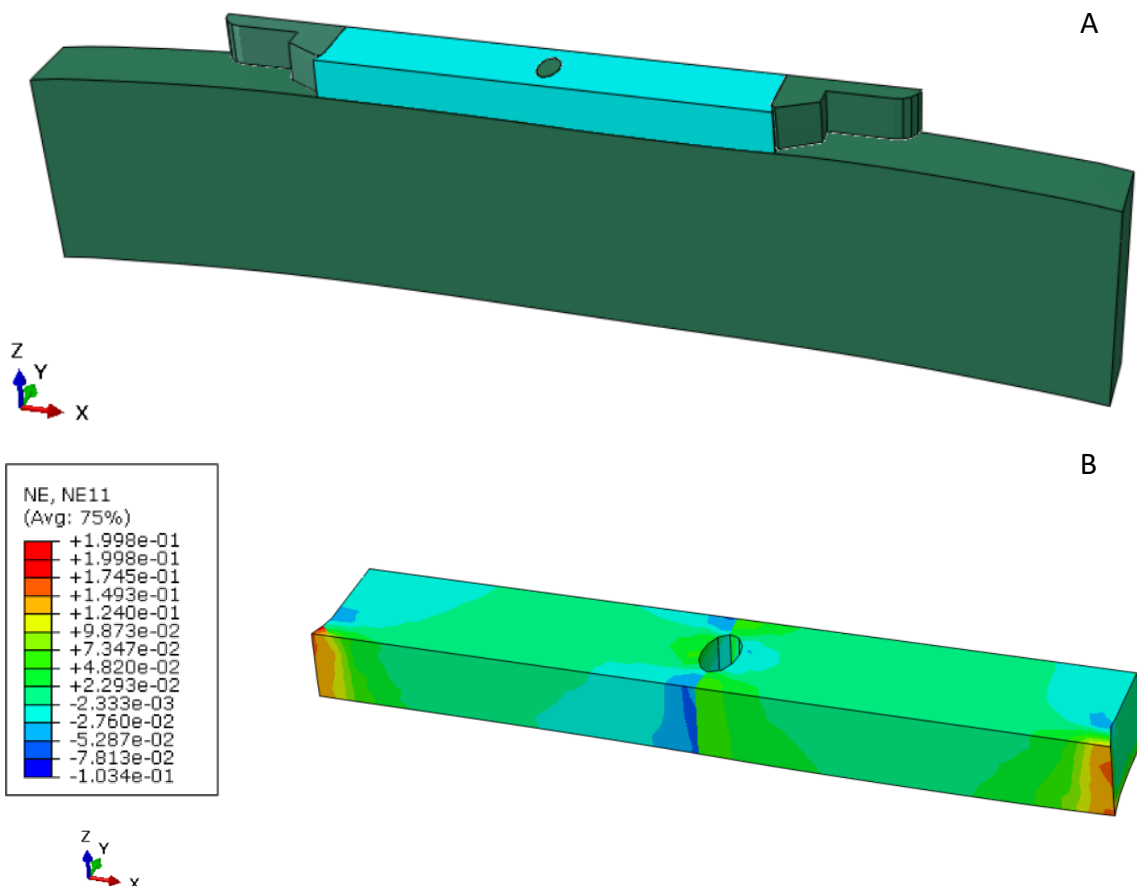
RESULTS
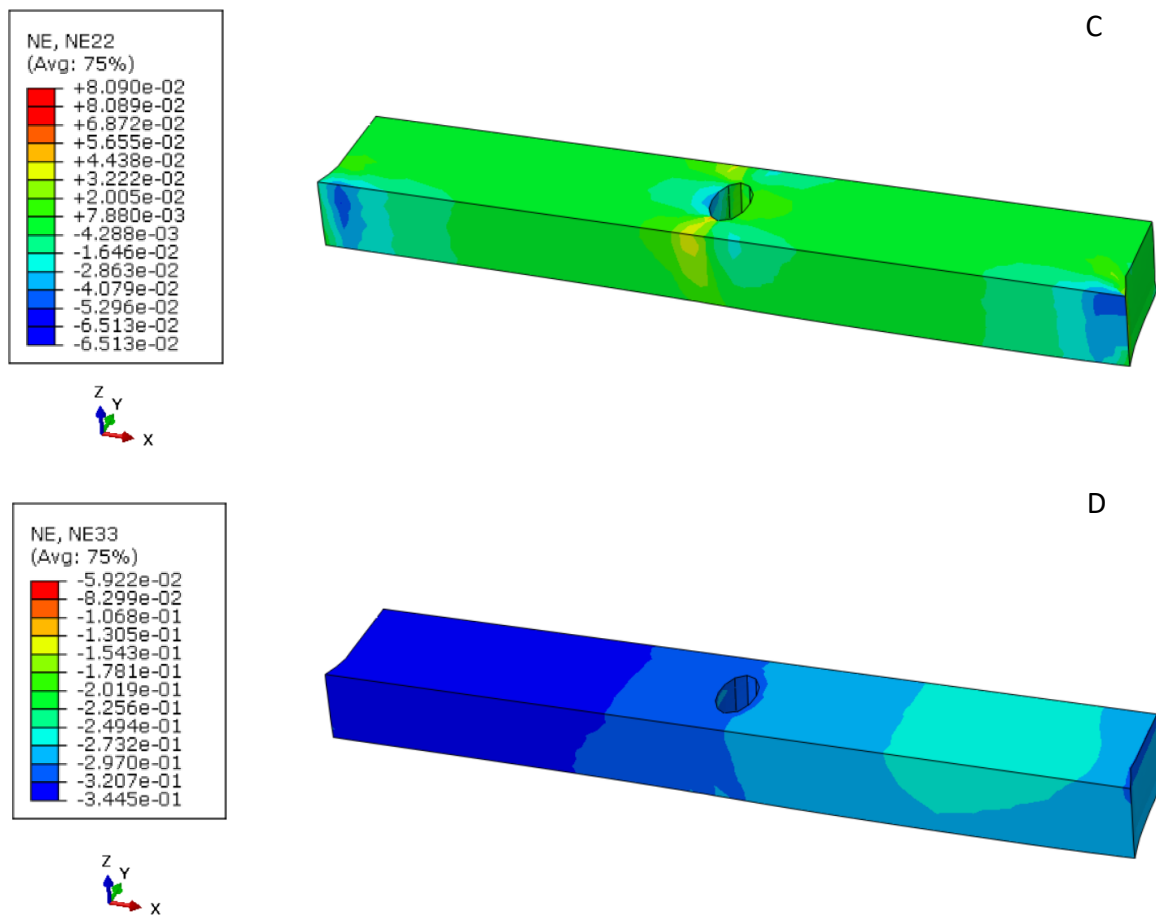
Fig. 3.2.1: *A) deformed configuration of the symmetric device. The pillars and the membrane are coloured in green, the hydrogels in blue. The calcified cartilage construct is on the right, the hyaline cartilage one on the left; B) contour plot of the strain along the X direction within the hydrogels; C) contour plot of the strain along the Y direction within the hydrogels; D) contour plot of the strain along the Z direction within the hydrogels.*

Fig. 3.2.2 shows the results for the asymmetric configuration of the device. In the hyaline cartilage construct, NE33 ranged from -24.6% in the region close to the central pillar, to -33.4% in the region in proximity of the lateral pillar. The median strain was -30.2%, the 25th percentile value was -26.7% and the 75th percentile value was -31.2%. The strain in the calcified cartilage construct was lower, with a median value of -17.4%. Here too, a gradient was present, with strains ranging from -4% to -25.9%. Ideally, the calcified cartilage construct should have been subjected to a zero strain along the Z direction. However, PDMS, although stiffer than the PEG hydrogel, is not infinitely rigid. Therefore, the mechanical stop provided by the pillars towards the membrane was different from the ideal one, and a certain amount of strain was found to be present in the calcified cartilage construct, too. The strain along the X direction had a median value of 0.4% for the hyaline cartilage construct. Peaks with a maximum value of 21.6% were found in the regions close to the openings between pillars, indicating an unwanted lateral expansion of the hydrogel. However, NE11 was low

in most of the region, as testified by a 75th percentile value of 1.4%. The calcified cartilage construct was almost perfectly confined by the pillars, being subjected to a strain along the X direction with a median value of 0.1% and an IQR of 7.4%. NE22 was found to be negligible within both the constructs, with a median value of 0.1%, a 25th percentile of -0.1% and a 75th percentile of 0.4%.

A

B

C
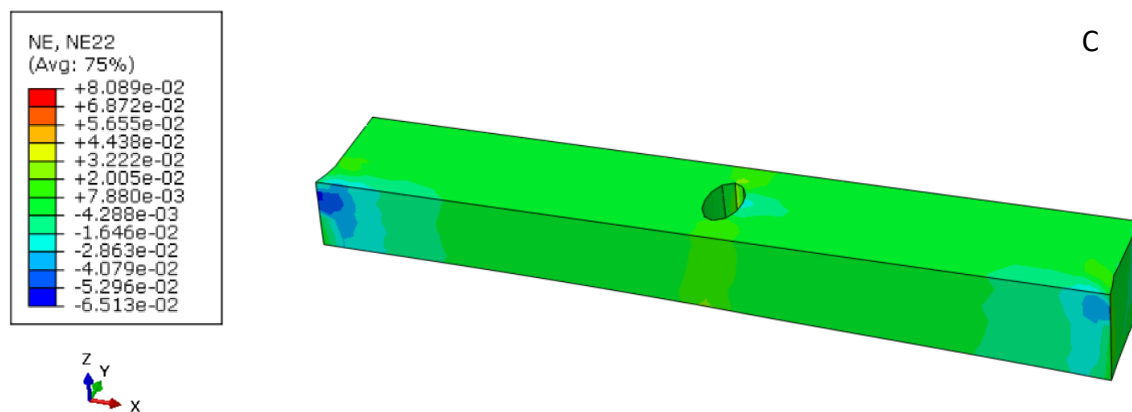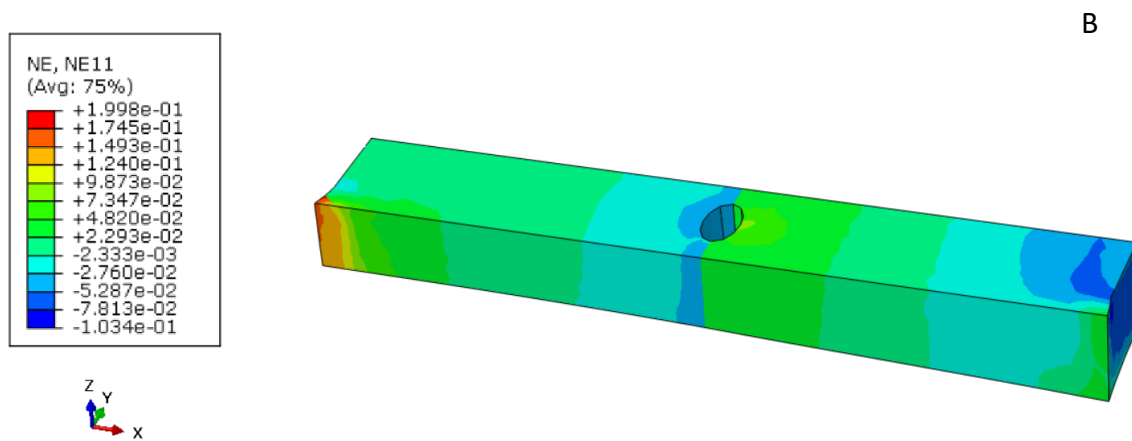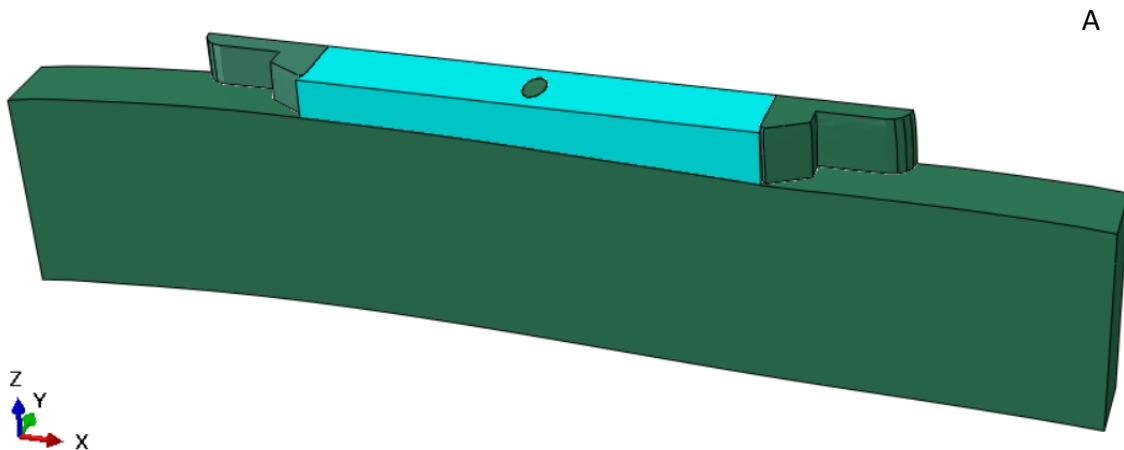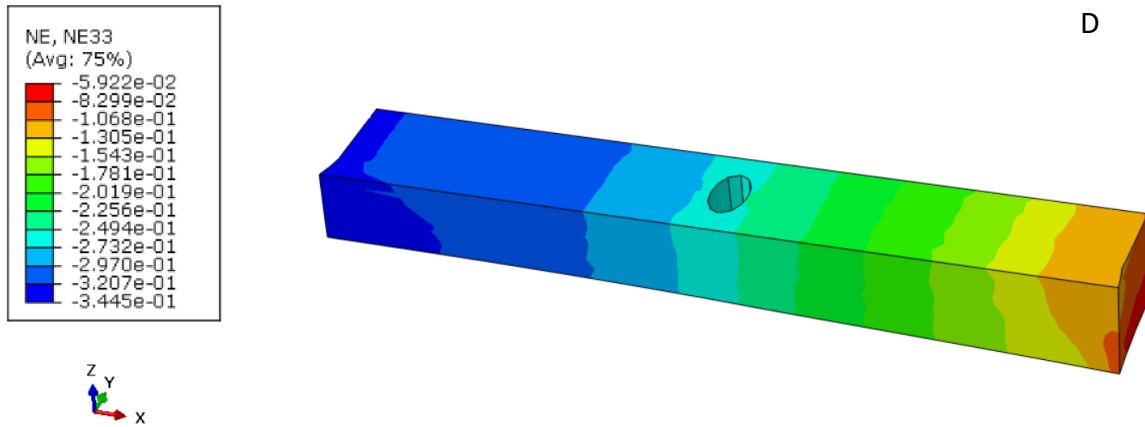
Fig. 3.2.2: *A) deformed configuration of the asymmetric device. The pillars and the membrane are coloured in green, the hydrogels in blue. The calcified cartilage construct is on the right, the hyaline cartilage one on the left; B) contour plot of the strain along the X direction within the hydrogels; C) contour plot of the strain along the Y direction within the hydrogels; D) contour plot of the strain along the Z direction within the hydrogels.*

Fig. 3.2.3 shows the median vertical displacement of the bottom surface of the hydrogels in the two device configurations. The left part of the graph refers to the hyaline cartilage construct, the right part to the calcified cartilage one. For the hyaline cartilage construct, the displacement of the bottom surface was 44.8 ± 2.1 μm in the symmetric device and 43.2 ± 6.4 μm in the asymmetric device (median ± IQR). There was no difference between the two configurations in the region close to the lateral pillars, while in the central region the median displacement in the symmetric configuration was 5.3 μm higher than that in the asymmetric configuration. For the calcified cartilage construct, the displacement of the bottom surface was 39.0 ± 2.5 μm in the symmetric device and 25.0 ± 14.9 μm in the asymmetric device. The median displacement in the symmetric configuration was 5.9 μm higher than that in the asymmetric configuration in the central region, and 28.2 μm higher in the region close to the lateral pillars.
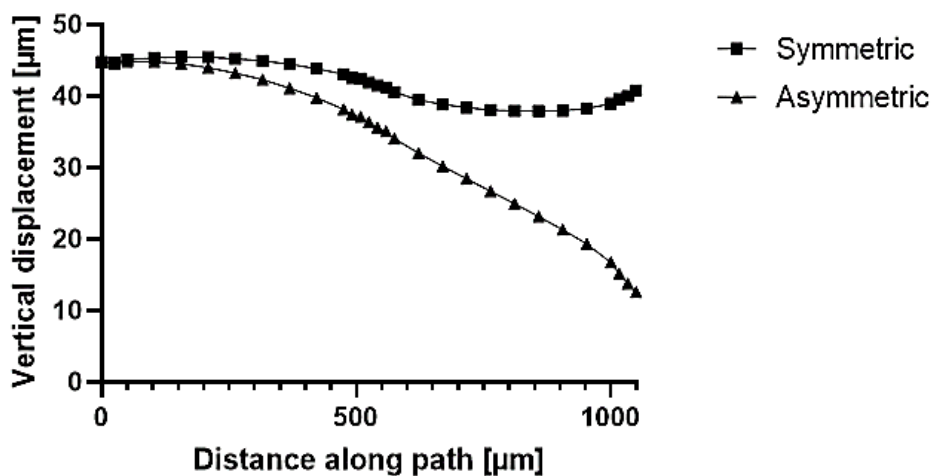
Fig. 3.2.3: *median vertical displacement of the bottom surface of the hydrogels in the symmetric and asymmetric configuration of the device. The left part of the graph refers to the hyaline cartilage construct, the right part to the calcified cartilage one.*

The results of the simulations performed varying the Young modulus of the calcified cartilage construct are shown in Fig. 3.2.4 and Fig. 3.2.5. The variations only affected the strain within the calcified cartilage construct, while the deformation field within the hyaline cartilage one remained almost unchanged. A reduction in the Young modulus produced an increase in the vertical displacement of the bottom surface of the calcified cartilage construct. For the symmetric device, the displacement went from 39.0 ± 2.5 μm for E = 200 kPa to 48.5 ± 2.3 μm for E = 100 kPa (median ± IQR). For the asymmetric device, the displacement went from 25.0 ± 14.9 μm for E = 200 kPa to 34.6 ± 14.9 μm for E = 100 kPa.
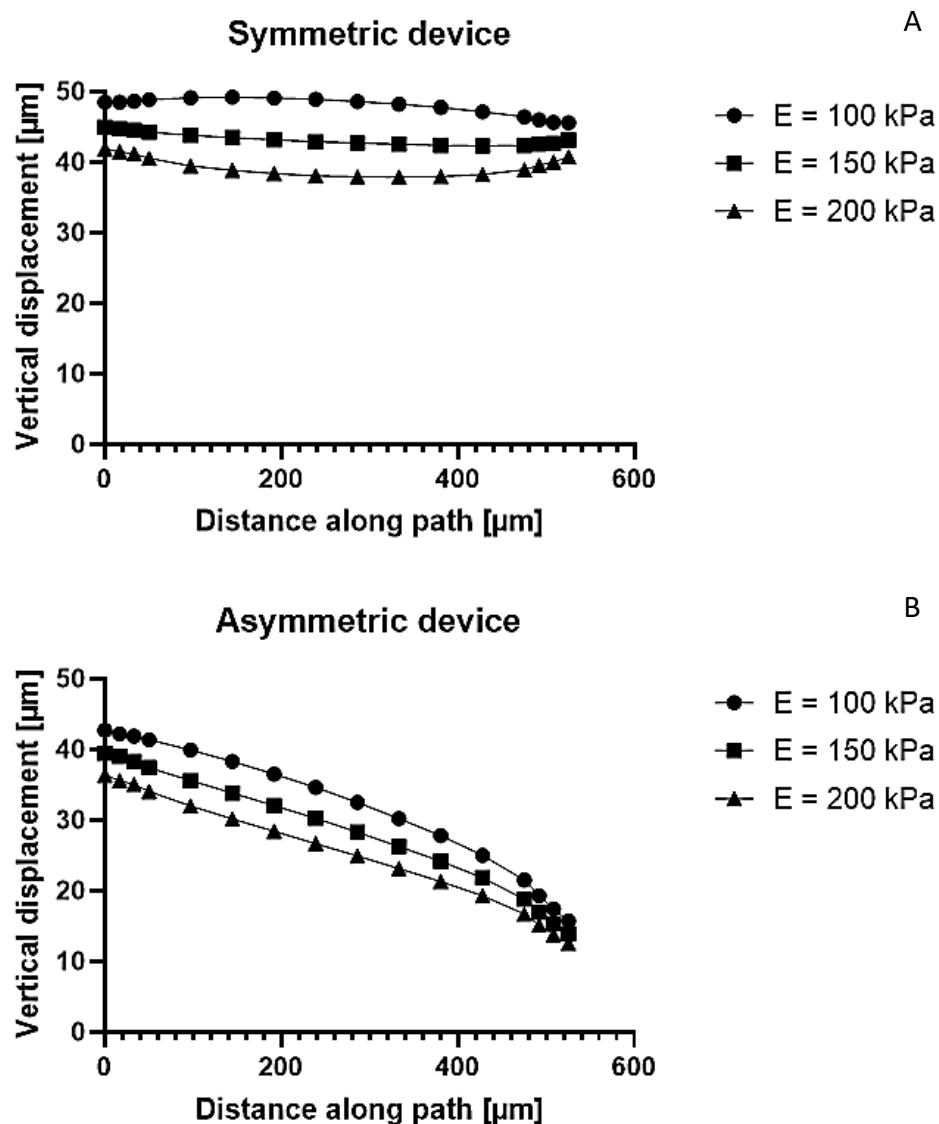
Fig. 3.2.4: *median vertical displacement of the bottom surface of the calcified cartilage construct in the symmetric (A) and asymmetric (B) configuration of the device, obtained by varying the Young modulus of the material.*

RESULTS

A higher displacement determined an increase in the absolute value of NE33. For the symmetric configuration of the device, the median strain was -27.5% for E = 200 kPa, -30.1% for E = 150 kPa, -33.8% for E = 100 kPa. The 25th percentile values were -26.8%, -29.8% and -32.6%, respectively, while the 75th percentile values were -28.4%, -30.9% and -34.2%, respectively. For the asymmetric configuration of the device, the median value was -17.4% for E = 200 kPa, -19.8% for E = 150 kPa, -22.7% for E = 100 kPa. The 25th percentile values were -11.6%, -13% and -14.9%, respectively, while the 75th percentile values were -23.5%, -25.9% and -28.6%, respectively. NE11 and NE22 were almost unaffected by the changes in the Young modulus (data not shown). Overall, a 100% increase in the stiffness resulted in a 18.6% decrease in the mean strain for the symmetric device and a 23.3% decrease for the asymmetric one.
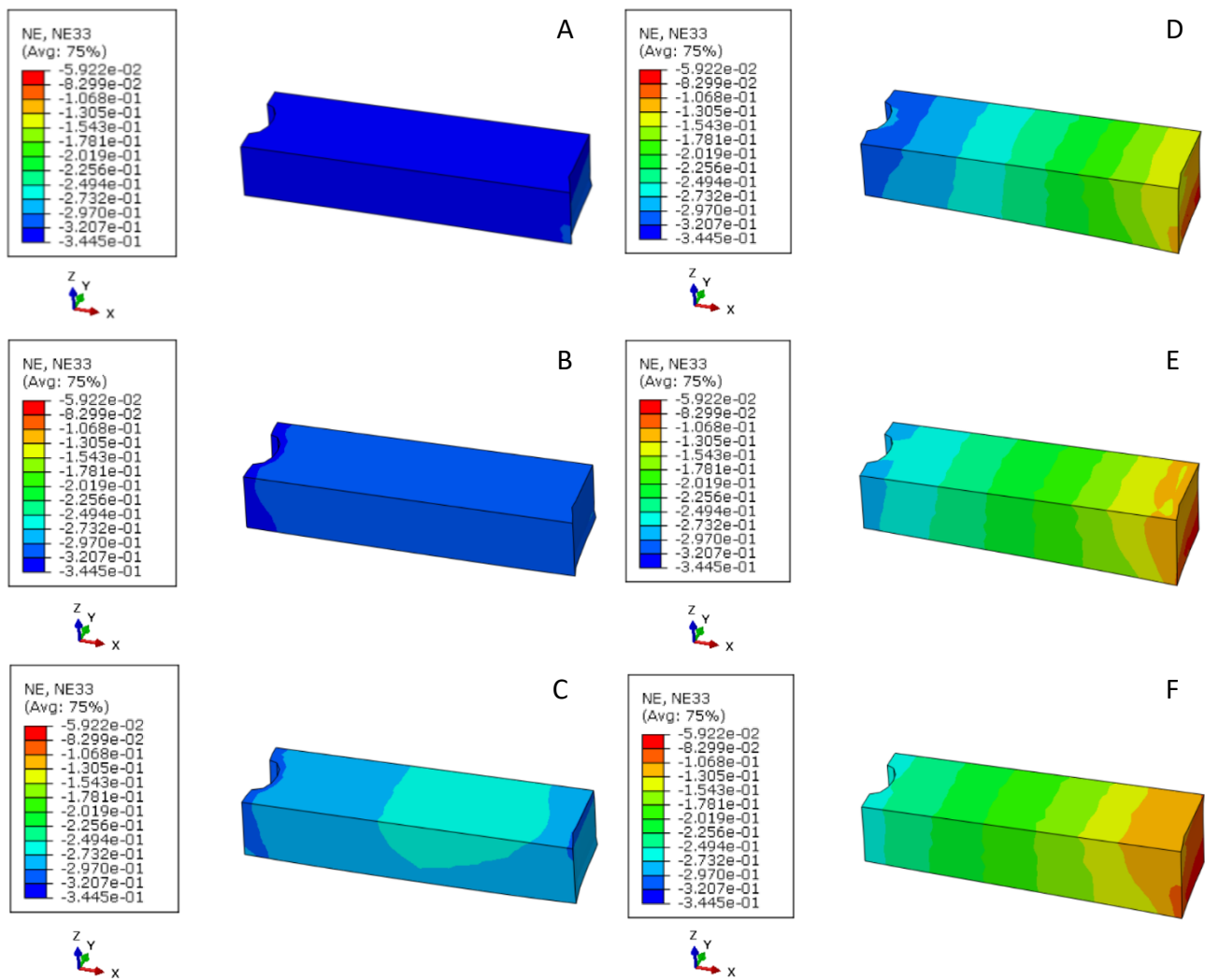
Fig. 3.2.5: *contour plots of the strain along the Z direction within the calcified cartilage construct, obtained by varying the Young modulus of the material. A) Symmetric device, E = 100 kPa; B) Symmetric device, E = 150 kPa; C) Symmetric device, E = 200 kPa; D) Asymmetric device, E = 100 kPa; E) Asymmetric device, E = 150 kPa; F) Asymmetric device, E = 200 kPa.*

3.3   Device production

Fig. 3.3.1 shows a picture of a representative microfluidic device, comprising three biologically independent culture chambers and a single actuation chamber with three compartments. Inlets for the gel channels and the actuation chamber are highlighted in red and yellow, respectively, and reservoirs for culture medium in blue.
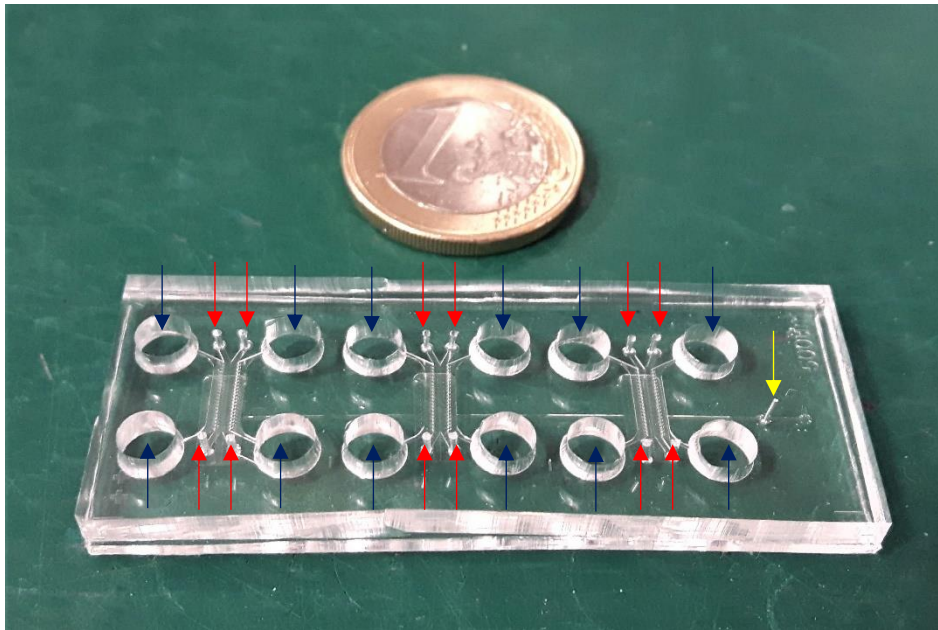
Fig. 3.3.1: *picture of a representative microfluidic device. Red arrows indicate inlets for gel channels, blue arrows indicate culture medium reservoirs, and the yellow arrow indicates the access to the actuation chamber.*

3.4   Device characterization

3.4.1   Geometrical characterization

Sections of the devices were cut and analysed to verify the correspondence between the actual dimensions of the microfeatures and the nominal ones. The height of the pillars and the gap was measured, and used to calculate the compression level produced by the devices. Results for the three different versions of the device are reported in Fig. 3.4.1. Compression levels were equal to 30.3% ± 2.2%, 29.7% ± 2.8% and 31.3% ± 2.2% for Pillar, Wall and UniLat devices, respectively. In the latter case, only the hyaline cartilage compartment was considered, since there were no gaps underneath the pillars in the calcified cartilage compartment. None of these values was significantly different from the target compression level, set to 30%.
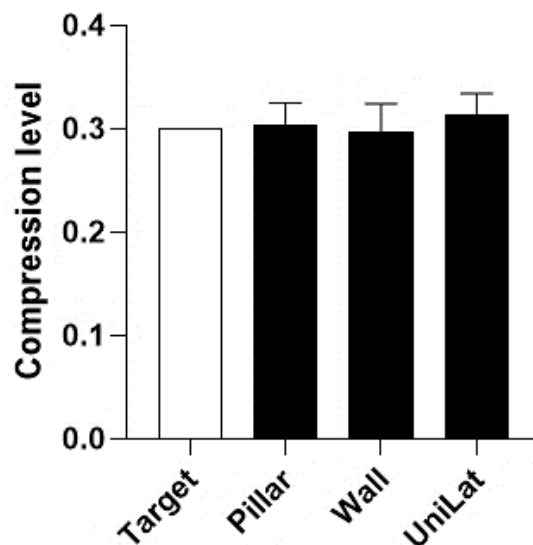
Fig. 3.4.1: *compression levels produced by the three different versions of the microfluidic device, compared to the target value; n = 9 sections from N = 3 devices were considered for each version. Mean and SD are reported. Statistical significance was determined by ordinary one-way ANOVA test and Dunnett's multiple comparisons test (normal distributions). The significance level was p < 0.05.*

3.4.2 Determination of the optimal actuation pressure

The optimal actuation pressure was obtained experimentally, correlating the displacement of the actuation membrane and the colour intensity of a dye filling the culture chamber of the devices. The results, reported in Fig. 3.4.2, refer to n = 3 Pillar devices and n = 3 UniLat devices, with a membrane thickness of 976 ± 133 μm. Such thickness guaranteed the actuation pressure to be rather independent of the presence of the hydrogel within the culture chamber. The optimal actuation pressure was defined as the one corresponding to the beginning of the plateau in colour intensity, i.e., the lowest possible pressure resulting in a mean normalized grey level above 99/100. Values of 300 and 400 millibars were found for Pillar and UniLat devices, respectively. An actuation pressure of 400 millibars was therefore adopted for all subsequent experiments.
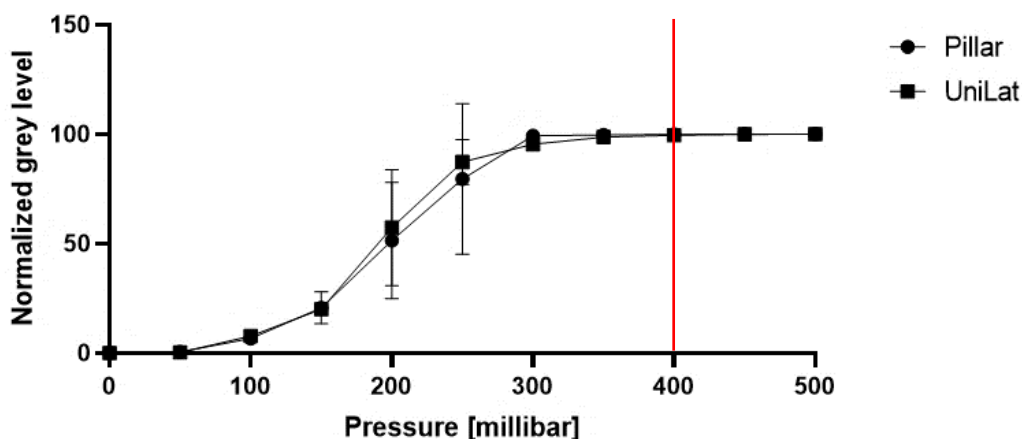
Fig. 3.4.2: *relation between the applied pressure and the normalized grey level for Pillar and UniLat devices; n = 3 devices were considered for each version. Mean and SD are reported. The optimal actuation pressure (red line) was defined as the one corresponding to the beginning of the plateau in the normalized grey level.*

3.5 Maturation of a calcified cartilage construct

The development of MSCs-derived calcified cartilage constructs was assessed. Bone marrow derived MSCs were cultured up to 14 days in static conditions in uKnee devices, and their capacity to differentiate into hypertrophic chondrocytes and produce a mature construct was evaluated.
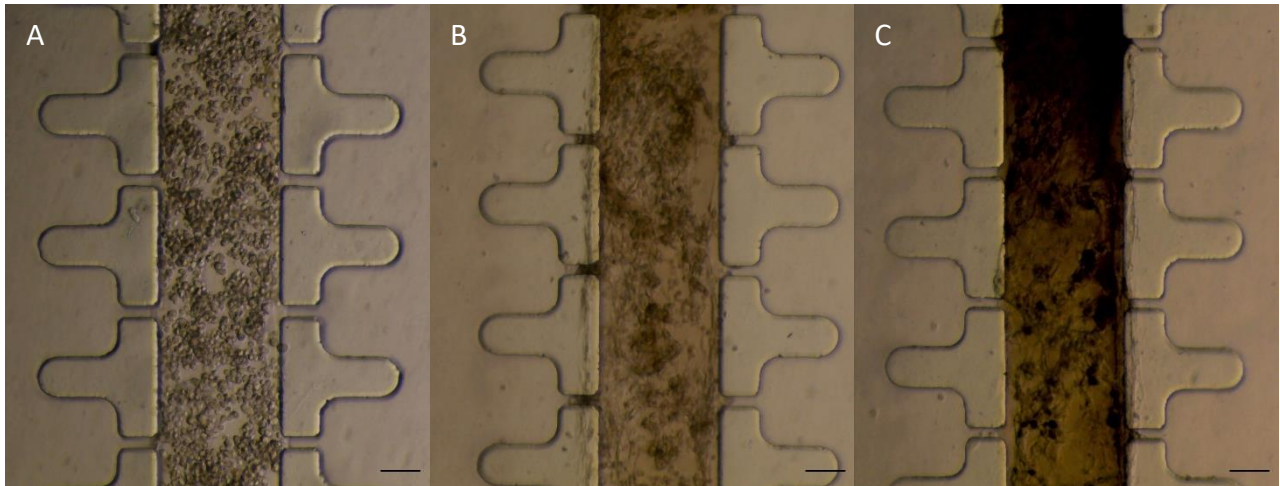
Fig. 3.5.1: *phase contrast images of the cell constructs at different time points: A) day 0; B) day 7; C) day 14. Scale bar 100 μm.*
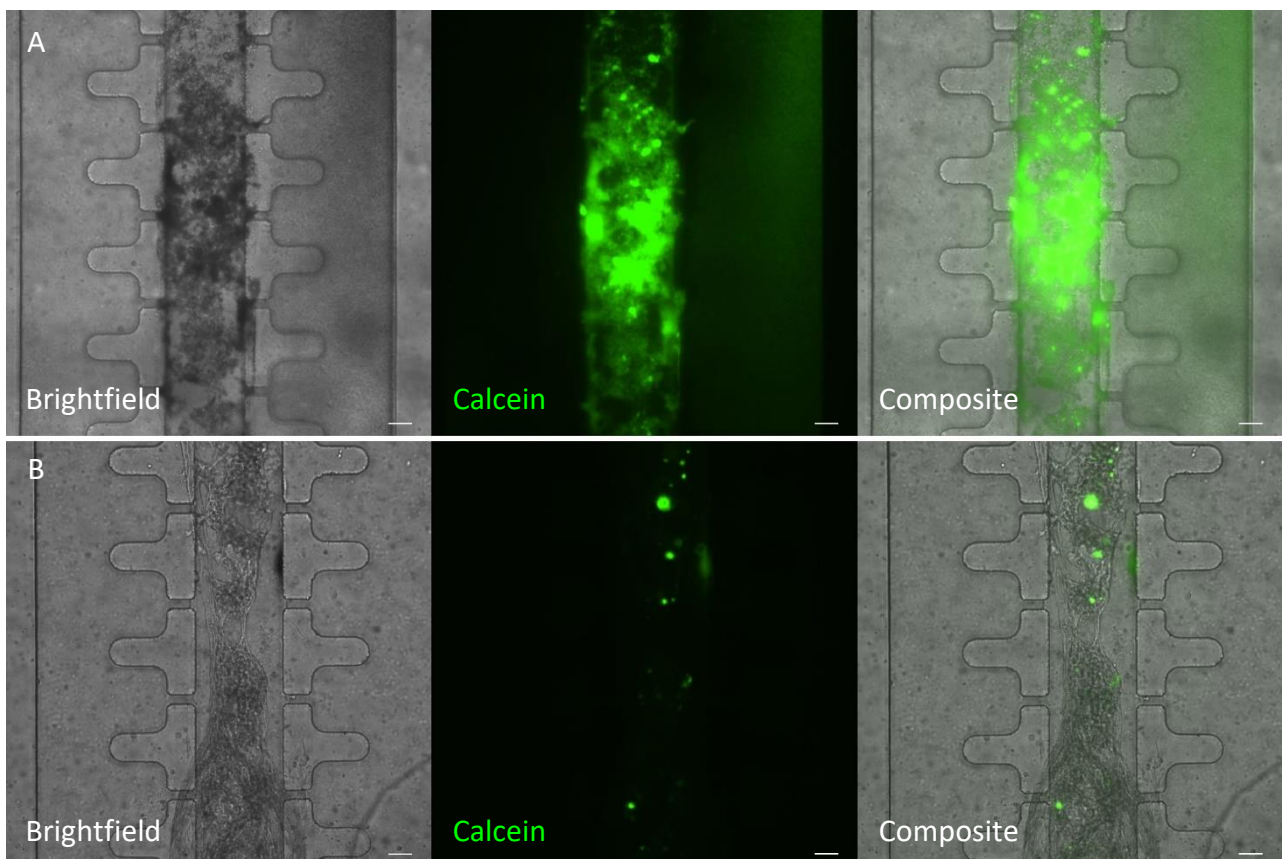
Fig. 3.5.2: *brightfield images and Calcein staining of constructs cultured in OCM (A) and CHM (B). Pictures were taken at day 14. Scale bar 100 μm.*

RESULTS

Fig. 3.5.1 shows three representative phase contrast images of the cell constructs at different time points, namely day 0, day 7 and day 14 after seeding. At day 0, cells exhibited a round morphology, which became more elongated at day 7 and day 14. ECM was totally absent at day 0, while it was visible at later time points. At day 14, phase contrast images of the cell constructs displayed dark spots and homogeneous dark areas, although their extent had a certain inter- and intra-donor variability. These areas resulted positive for Calcein (Fig. 3.5.2 A), demonstrating that MSCs cultured in osteochondral medium were able to produce a calcified matrix. On the contrary, Calcein staining was negative for the sample cultured in chondrogenic medium, apart from some impurities (Fig. 3.5.2 B).
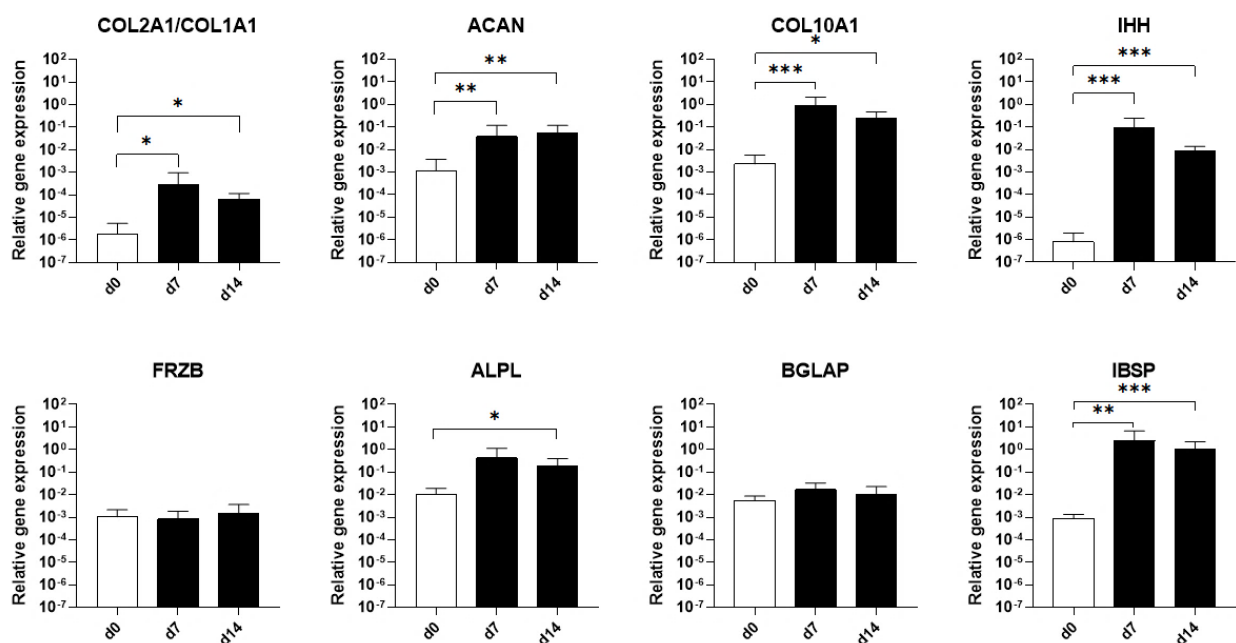
Fig. 3.5.3: *expression levels of relevant genes at day 0, day 7 and day 14, relative to the expression of GAPDH; n = 9 biologically independent samples from N = 3 different donors were analysed. Mean and SD are reported. Statistical significance was determined by Kruskal-Wallis tests and Dunn's multiple comparisons tests (non-normal distributions). * p < 0.05, ** p < 0.01, *** p < 0.005.*

Assumption of a calcified cartilage phenotype was also assessed by gene expression analysis. Results, relative to n = 9 biologically independent samples from N = 3 different cell donors, are shown in Fig. 3.5.3. The expression of aggrecan and the ratio between the expressions of collagen type II and collagen type I were significantly higher at day 14 as compared to day 0, demonstrating the capacity of MSCs to differentiate into chondrocytes and produce cartilaginous constructs. Genes associated with chondrocyte hypertrophy, namely IHH and COL10A1, were also strongly upregulated. A slight downregulation of these genes was visible from day 7 to day 14, although not statistically significant. This downregulation was present in a single cell donor, while the expression of hypertrophic genes in the remaining two donors was monotonically increasing during the whole

maturation period. On the other hand, the expression of the hypertrophy inhibitor FRZB was not modulated, and remained close to the basal level both at day 7 and day 14 for all donors. ALPL, a marker of mineralization, was significantly higher at day 14 compared to day 0, confirming the results obtained by Calcein staining. Among bone markers, IBSP was strongly upregulated at day 7 and day 14 with respect to day 0, while BGLAP did not show any modulations. For all the considered genes, no significant changes were found between day 7 and day 14.

3.6   Effect of cyclic hyperphysiological compression on the calcified cartilage construct

Once verified the maturation of calcified cartilage constructs, the effect of hyperphysiological compression was assessed. Results in terms of gene expression are reported in Fig. 3.6.1. A highly donor-dependent behaviour was observed. The hypertrophy inhibitor FRZB was significantly downregulated (5.5-fold) in the constructs subjected to mechanical stimulation, as compared to static controls. The other considered hypertrophy inhibitors (GREM1 and DKK1), as well as the hypertrophy markers IHH and COL10A1, did not display significant modulations. The expression of hypertrophy inhibitors exhibited different trends in the different cell donors: in particular, the expression of GREM1 in constructs subjected to mechanical stimulation was two orders of magnitude lower than that in static controls for one cell donor, but did not show any modulations at all for the remaining two donors; for two donors, DKK1 was downregulated in constructs exposed to hyperphysiological compression (3.4-fold and 6.7-fold, respectively), but this trend was not observed in the third donor. Hyperphysiological compression determined a significant upregulation of BGLAP (2.8-fold), a marker of bone formation. However, IBSP, the other considered bone marker, was not differentially expressed in the two groups. Also in this case, a certain variability was observed among the different cell donors: for one donor, IBSP showed a relevant upregulation (54.8-fold) in constructs exposed to hyperphysiological compression, but the other two donors did not display any modulations. A statistically significant 3.7-fold decrease in the expression of the antiangiogenic factor LECT1 was detected in the constructs subjected to mechanical stimulation, although the expression level was low also in the static controls. The expression levels of ALPL, a marker of mineralization, and MMP13, a marker of catabolism, were almost constant in the two experimental groups. The expression of CXCL8, a marker of inflammation, was 2.1-fold higher in the mechanically stimulated group as compared to the static group, but the increase was not statistically significant. A 3.1-fold downregulation of ACAN and a 3.3-fold increase in the ratio between COL2A1

and COL1A1 were observed in the constructs subjected to mechanical stimulation, as compared to static controls. However, there was a high inter- and intra-donor variability in the expression of these genes, and neither of the alterations was statistically significant.
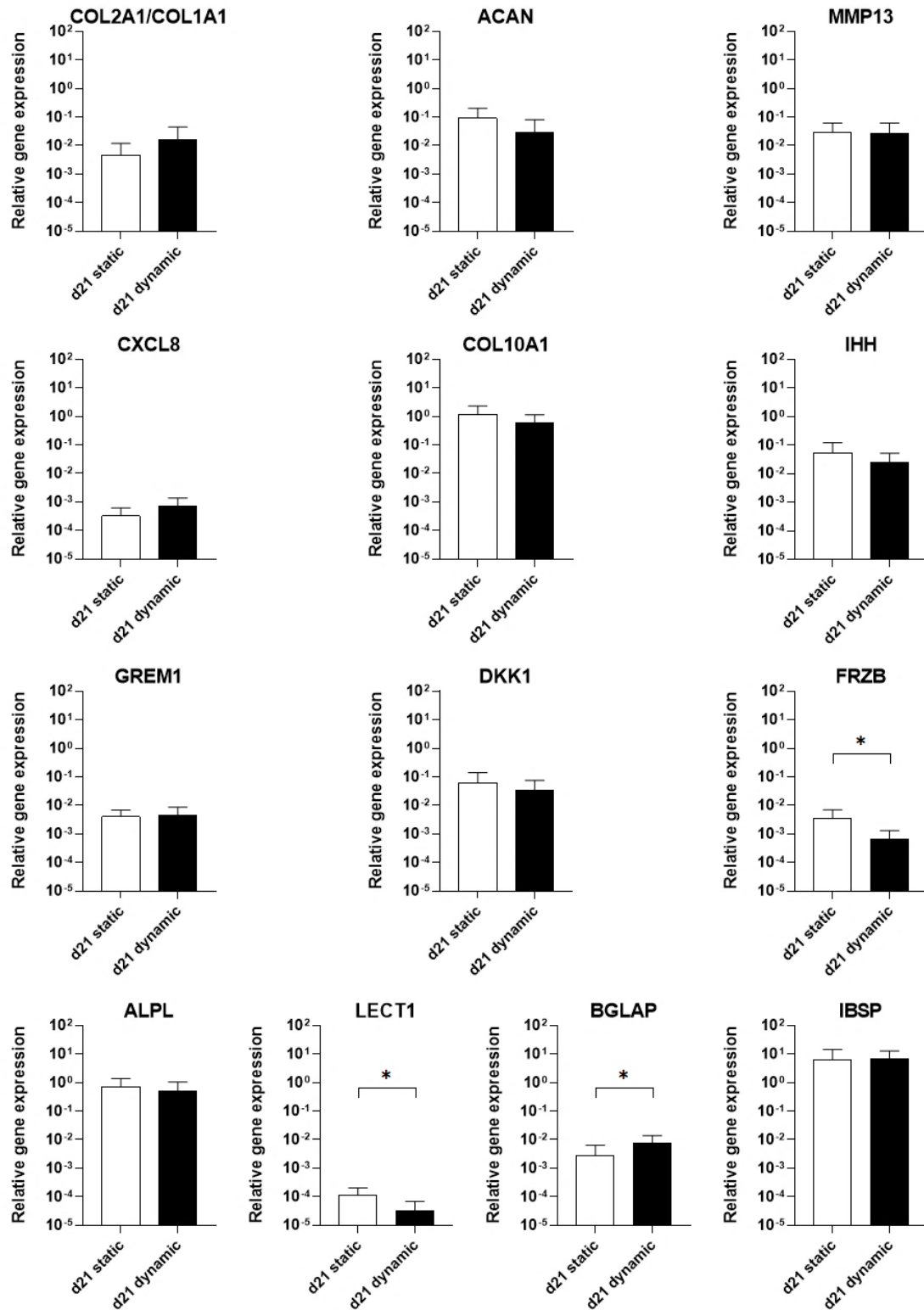
Fig. 3.6.1: *expression levels of relevant genes in cells cultured either in static or dynamic conditions, relative to the expression of GAPDH; n = 9 biologically independent samples from N = 3 cell donors were analysed. Mean and SD are reported. Statistical significance was determined by Mann-Whitney test. The significance level was p < 0.05.*

3.7 Biological validation of the strain produced by the device

A validation of the strain produced by the UniLat device was performed, to verify that the unwanted deformation induced in the calcified cartilage construct (discussed in section 3.2) did not induce phenotypical changes. Gene expression levels at day 21, reported in Fig. 3.7.1, refer to n = 3 biologically independent samples from a single cell donor, cultured either in static or dynamic conditions. Genes associated with chondrogenesis, catabolism, inflammation and hypertrophy were analysed. None of the considered genes was differentially expressed in the two experimental conditions.
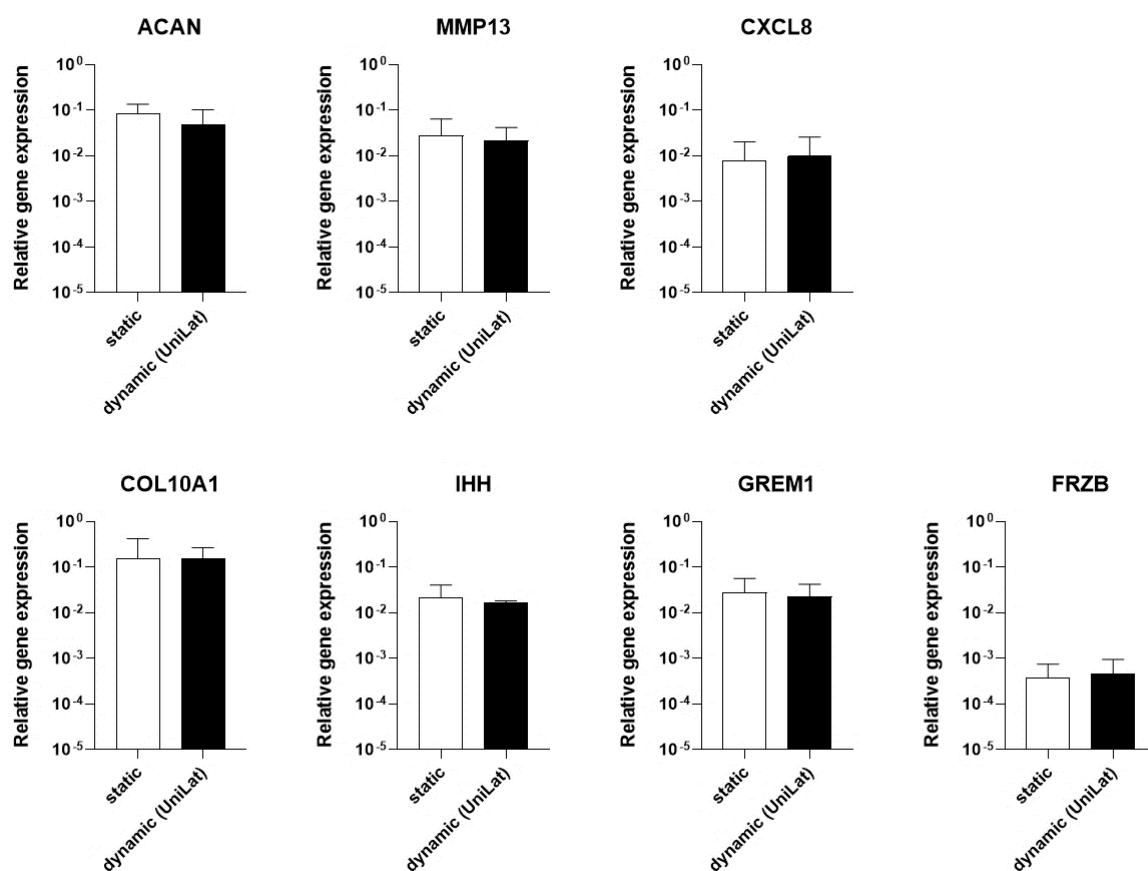
Fig. 3.7.1: *expression levels of relevant genes in cells either cultured in static conditions or subjected to mechanical stimulation in the UniLat device, relative to the expression of GAPDH; n = 3 biologically independent samples from N = 1 donor were analysed. Mean and SD are reported. Statistical significance was determined by Mann-Whitney test. The significance level was p < 0.05.*

Another experiment was performed to verify that the compression level obtained with Pillar devices had the same effect on cell constructs as the one obtained with uKnee devices. Gene expression levels at day 21 were compared among constructs cultured in static conditions or in dynamic conditions either in a Pillar or in a uKnee device. Results, reported in Fig. 3.7.2, refer to n = 3 biologically independent samples from a single cell donor. No relevant changes in the expression

of the considered genes were observed between the constructs subjected to mechanical simulation in the two different devices. Hyperphysiological compression determined a slight downregulation of the chondrogenic marker ACAN (2.1-fold and 1.4-fold in the uKnee and the Pillar device, respectively), an upregulation of the catabolic marker MMP13 (2.7-fold and 1.9-fold, respectively), a slight upregulation of the inflammation marker CXCL8 (1.1-fold and 1.4-fold, respectively), an upregulation of the hypertrophy markers COL10A1 (4.6-fold and 3.0-fold, respectively) and IHH (18.7-fold and 10.1-fold, respectively), and a downregulation of the hypertrophy inhibitors GREM1 (1.3-fold and 1.8-fold, respectively) and FRZB (2.1-fold and 2.0-fold, respectively). None of the reported modulations was statistically significant, probably due to the low numerosity of the considered data sets.
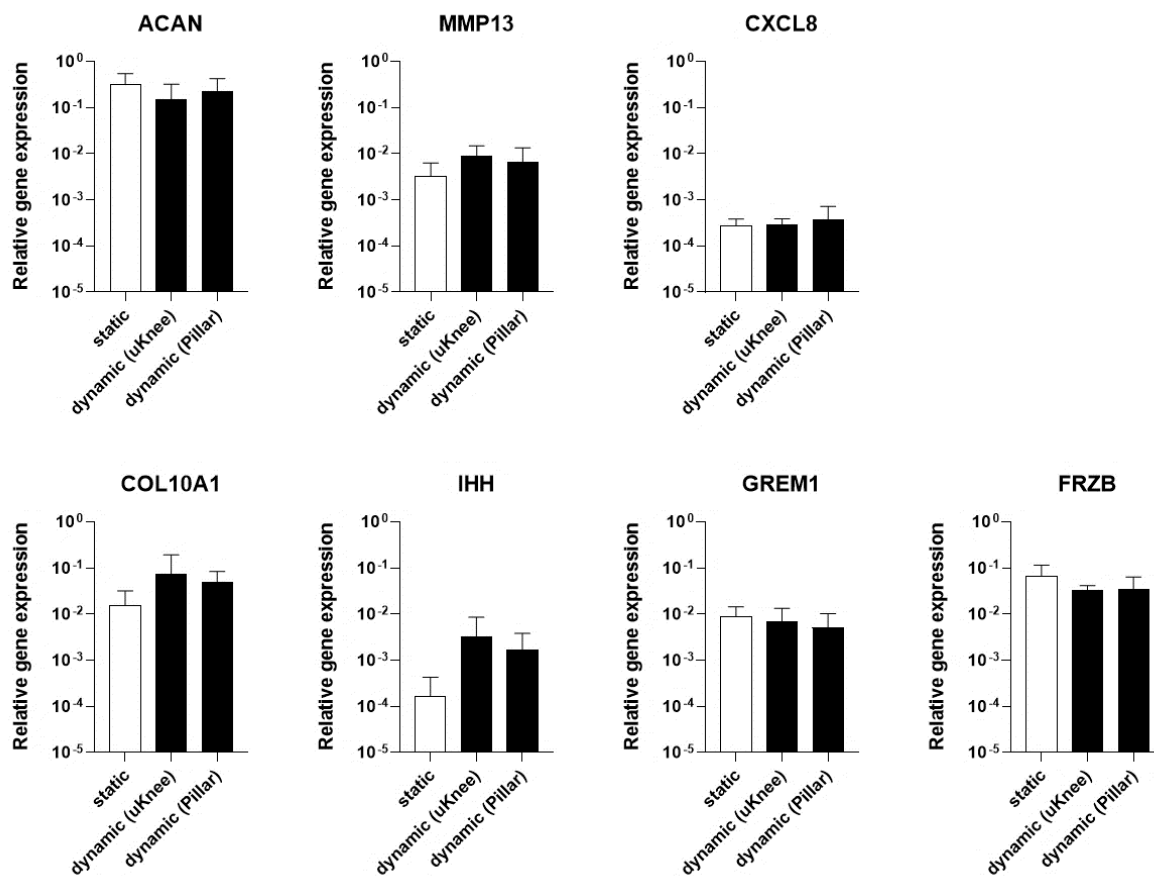
Fig. 3.7.2: *expression levels of relevant genes in HACs cultured in static conditions or subjected to mechanical stimulation either in Pillar or uKnee devices, relative to the expression of GAPDH; n = 3 biologically independent samples from N = 1 donor were analysed. Mean and SD are reported. Statistical significance was determined by Kruskal-Wallis tests and Dunn's multiple comparisons tests (non-normal distributions). The significance level was p < 0.05.*

3.8 Development of a healthy osteochondral cell construct

The capacity of HACs and MSCs to retain their differentiative potential upon coculture, forming a healthy osteochondral construct composed of a hyaline cartilage compartment and a calcified cartilage one, was assessed. HACs and MSCs were seeded into Pillar and Wall devices and cultured for two weeks in static conditions. uKnee devices were used as single culture controls.

Representative phase contrast images of the constructs at different time points are shown in Fig. 3.8.1. Mineralization of the calcified construct was clearly visible at day 14 in both versions of the device (Fig. 3.8.1 C, F). The hyaline cartilage construct remained uncalcified in both the device versions. No clear differences were visible between the two versions in terms of interface shape.
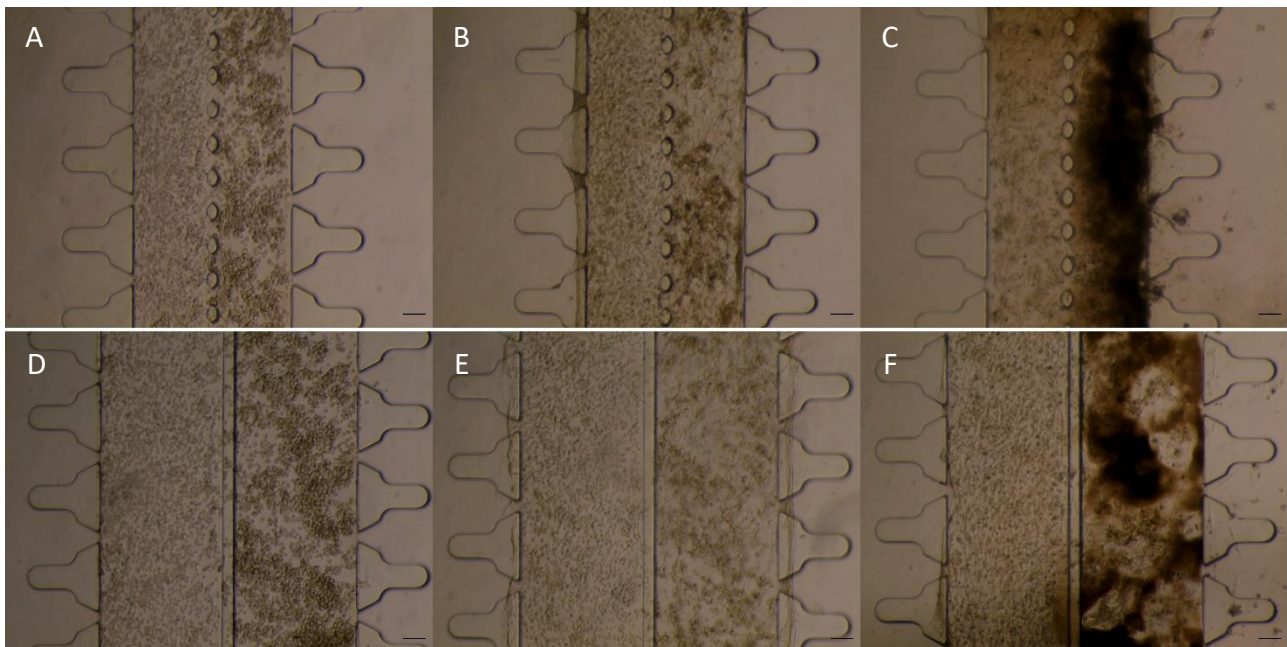
Fig. 3.8.1: *phase contrast images of the osteochondral cell construct at different time points and in different device versions: A) Pillar, day 0; B) Pillar, day 7; C) Pillar, day 14; D) Wall, day 0; E) Wall, day 7; F) Wall, day 14. The hyaline cartilage construct is visible on the left, the calcified cartilage construct on the right. Scale bar 100 μm.*

ECM composition and tissue maturation at different time points were investigated by means of immunofluorescence. Constructs were stained for cell nuclei, hydroxyapatite, aggrecan and collagen type II, and analysed under a confocal microscope. The results are shown in Fig. 3.8.2. At day 0 (Fig. 3.8.2 A), constructs were only positive for the DNA marker DAPI, while no ECM was present. At this rime point, due to the absence of ECM, constructs had a low structural integrity, and broke when opening microfluidic devices to perform the staining. For this reason, Fig. 3.8.2 A shows only a fragment of the osteochondral construct, and cells do not occupy the whole region. At day 7 (Fig. 3.8.2 B), the calcified cartilage construct was weakly stained for hydroxyapatite and

aggrecan, while the hyaline cartilage construct was negative. None of the constructs was found positive for collagen type II. At day 14 (Fig. 3.8.2 C), both the constructs were positively stained for aggrecan, demonstrating the deposition of a cartilage-specific matrix. Collagen type II, another marker of cartilage formation, was detected in the calcified cartilage construct, but not in the hyaline cartilage one. The calcified cartilage construct showed a strong mineralization, being positive for hydroxyapatite, while the hyaline cartilage construct remained negative, apart from some impurities.
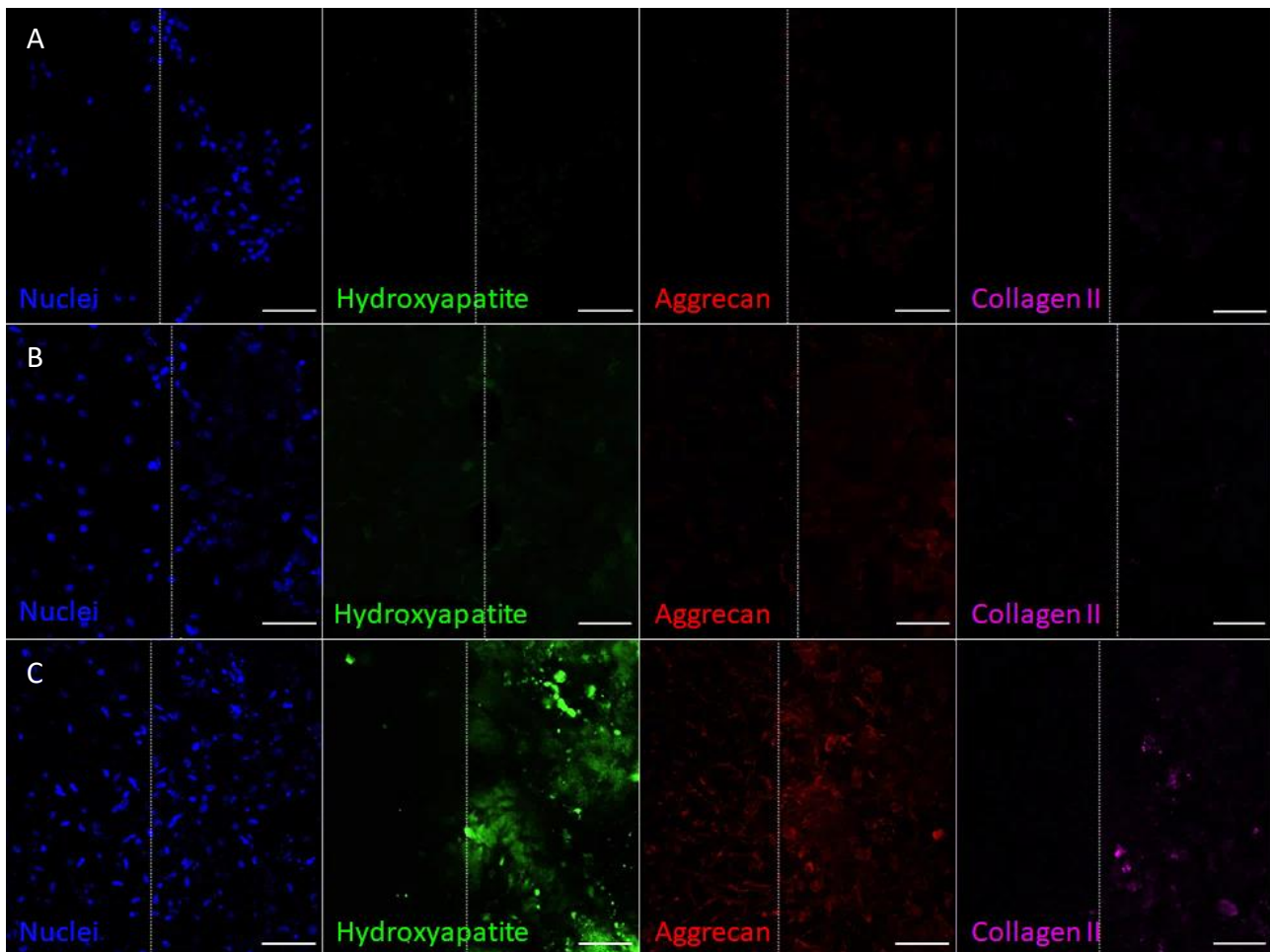
Fig. 3.8.2: immunofluorescence analysis of osteochondral constructs in the Pillar device, CLSM images. A) day 0; B) day 7; C) day 14. Constructs were stained for cell nuclei in blue, hydroxyapatite in green, aggrecan in red and collagen type II in magenta. The dashed lines indicate the interface between the hyaline cartilage construct (on the left) and the calcified cartilage construct (on the right). Scale bar 100 µm.

RESULTS

Gene expression was analysed at day 0 and day 14, to assess tissue maturation. n = 6 biologically independent samples from N = 2 MSCs donors and n = 6 biologically independent samples from N = 1 HACs donor were considered. To analyse possible effects of coculture, MSCs-derived hypertrophic chondrocytes and GFP-expressing HACs were sorted based on GFP expression. The amount of genetic material was very low in some of the cell constructs subjected to enzymatic digestion and sorting. Therefore, expression levels of some genes of interest could not be analysed in all the considered samples, and some data sets have a numerosity lower than 6. The amount of genetic material obtained after sorting displayed a high variability among samples, and it was not possible to correlate it with the number of cells initially seeded into the devices. Devices with a gel channel width of 500 µm and 300 µm were analysed. Devices with wider gel channels initially contained a higher number of cells, but the results did not reflect this difference, neither in terms of the numerosity of cell sub-populations obtained after sorting (as shown in Fig. 3.8.3.), nor in terms of the final amount of genetic material available for the analyses.

#Events

	Far Left	Left	Right	Far Right
A	🟩 + : 8317			🟦 - : 10525

	Far Left	Left	Right	Far Right
B	🟩 + : 6504			🟦 - : 17769
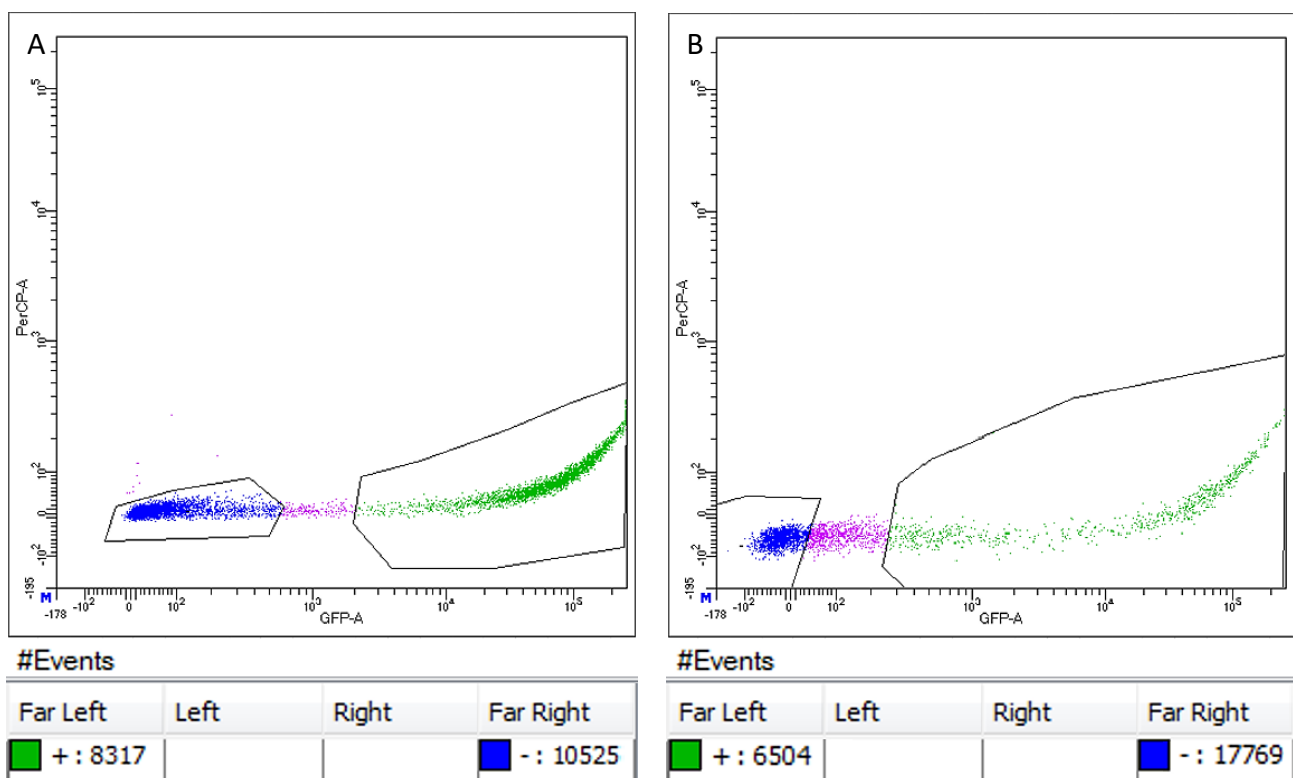
Fig. 3.8.3: representative scatter plots of sorted cells obtained from a device with a channel width of 300 µm (A) and a device with a channel width of 500 µm (B). Based on the intensity of the GFP fluorescent signal (reported on the X axis), cells were classified as GFP-negative (in blue) or GFP-positive (in green). Cells with an intermediate GFP expression and an uncertain identity (in purple) were discarded. The numerosity of the sub-populations obtained after sorting is reported below the two graphs.
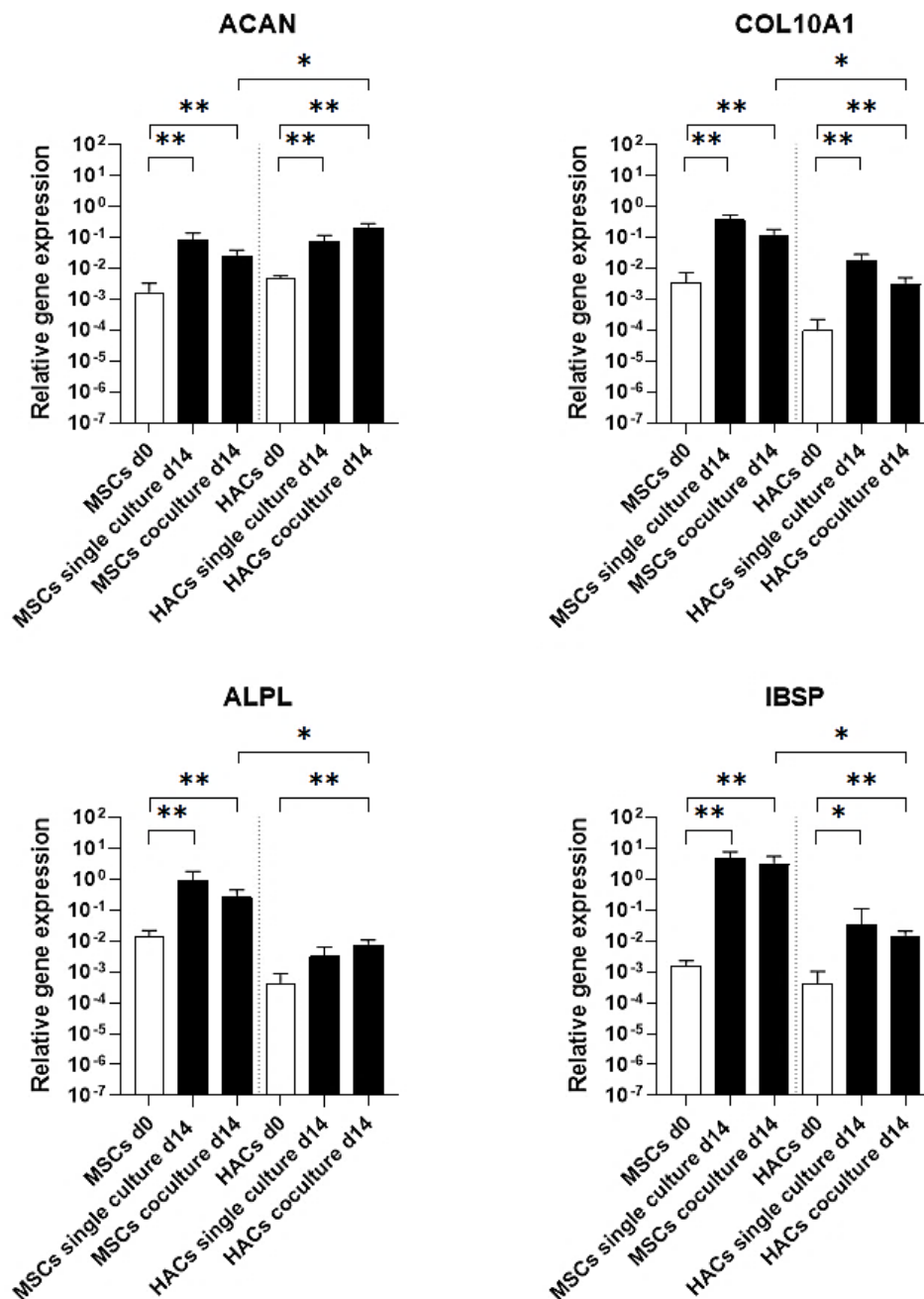
Fig. 3.8.4: *expression levels of relevant genes at day 0 and day 14, relative to the expression of GAPDH; n = 6 biologically independent samples from N = 2 MSCs donors and n = 6 biologically independent samples from N = 1 HACs donor were analysed. Mean and SD are reported. Statistical significance was determined by Mann-Whitney test.*
* p < 0.05, ** p < 0.01.

Gene expression at day 0 and 14 is reported in Fig. 3.8.4. Cocultured constructs were compared with each other and with their respective counterparts in single culture. Genes associated with chondrogenesis (ACAN), chondrocyte hypertrophy (COL10A1), mineralization (ALPL) and bone formation (IBSP) were considered. At day 14, ACAN was upregulated in HACs and MSCs both in single culture and coculture, as compared to day 0. In the osteochondral constructs, the expression of ACAN was significantly higher (8.4-fold) in the hyaline cartilage compartment with respect to the

calcified cartilage one. COL10A1 was upregulated in both constructs at day 14 as compared to day 0. However, the expression of this gene was significantly lower (39-fold) in the hyaline cartilage compartment as compared to the calcified cartilage one. ALPL and IBSP were significantly more expressed in the calcified cartilage constructs as compared to the hyaline cartilage ones, both in single culture and coculture. In the osteochondral constructs, the expression levels of ALPL and IBSP were respectively 35-fold and 215-fold higher in the calcified cartilage compartment as compared to the hyaline cartilage one. For all the experimental groups, ALPL and IBSP were significantly upregulated at day 14 as compared to day 0.

3.9 Effect of cyclic hyperphysiological compression on the osteochondral construct

The effect of cyclic hyperphysiological compression on the osteochondral cell constructs was assessed. Gene expression was analysed at day 21, to quantify the effect of mechanical stimulation. n = 6 biologically independent samples from N = 2 MSCs donors and n = 6 biologically independent samples from N = 1 HACs donor were considered for each experimental condition. To analyse possible effects of coculture, MSCs-derived hypertrophic chondrocytes and GFP-expressing HACs were sorted based on GFP expression. Also in this case, expression levels of some genes of interest could not be analysed in all the considered samples, due to the low amount of genetic material available after enzymatic digestion and sorting. Gene expression of constructs subjected to mechanical stimulation was normalized to that of the respective static controls, to exclude possible effects of enzymatic digestion and cell sorting and highlight only the effect of hyperphysiological compression. Results are reported in Fig. 3.9.1.

For hyaline cartilage constructs, genes associated with catabolism (MMP13), inflammation (CXCL8) and hypertrophy inhibition (FRZB) were analysed. MMP13 was upregulated (1.8-fold) in cells subjected to mechanical stimulation in Pillar devices, although this alteration was not statistically significant. The modulation was consistent with that observed in single culture. In UniLat devices, mechanical stimulation had an opposite effect, producing a significant downregulation of MMP13 (6.4-fold). CXCL8 was slightly upregulated in chondrocytes subjected to mechanical stimulation: in UniLat devices, the increase was 1.2-fold, while in Pillar devices the effect was more pronounced, resulting in a 2.4-fold upregulation. None of these alterations was statistically significant, and no relevant changes were observed with respect to single culture controls. For all the experimental groups, mechanical stimulation produced a downregulation of the hypertrophy

inhibitor FRZB. The reduction was 1.3-fold for Pillar devices and 2.1-fold for UniLat devices. Also in this case, alterations were consistent with those observed in single culture, and statistical significance was not achieved.

For calcified cartilage constructs, genes associated with bone formation (BLGAP), mineralization (ALPL), and hypertrophy inhibition (FRZB) were analysed. Hyperphysiological compression induced a 1.2-fold upregulation of BGLAP in Pillar devices and a 1.4-fold upregulation in UniLat devices, although these modulations were not statistically significant. In single culture controls, this effect was more pronounced, resulting in a 2.4-fold upregulation. ALPL was downregulated in all experimental groups subjected to mechanical stimulation, as compared to static controls. The downregulation was 2.1-fold for Pillar devices and 1.8-fold for UniLat devices. In both cases, the modulation was more pronounced that the one observed in single culture controls, but statistical significance was not achieved. In Pillar devices, hyperphysiological compression produced a statistically significant 8.6-fold downregulation of FRZB, consistent with what was observed in single culture controls. As regards UniLat devices, FRZB was not detected in any of the analysed samples, due to the low amount of genetic material obtained after enzymatic digestion and cell sorting.
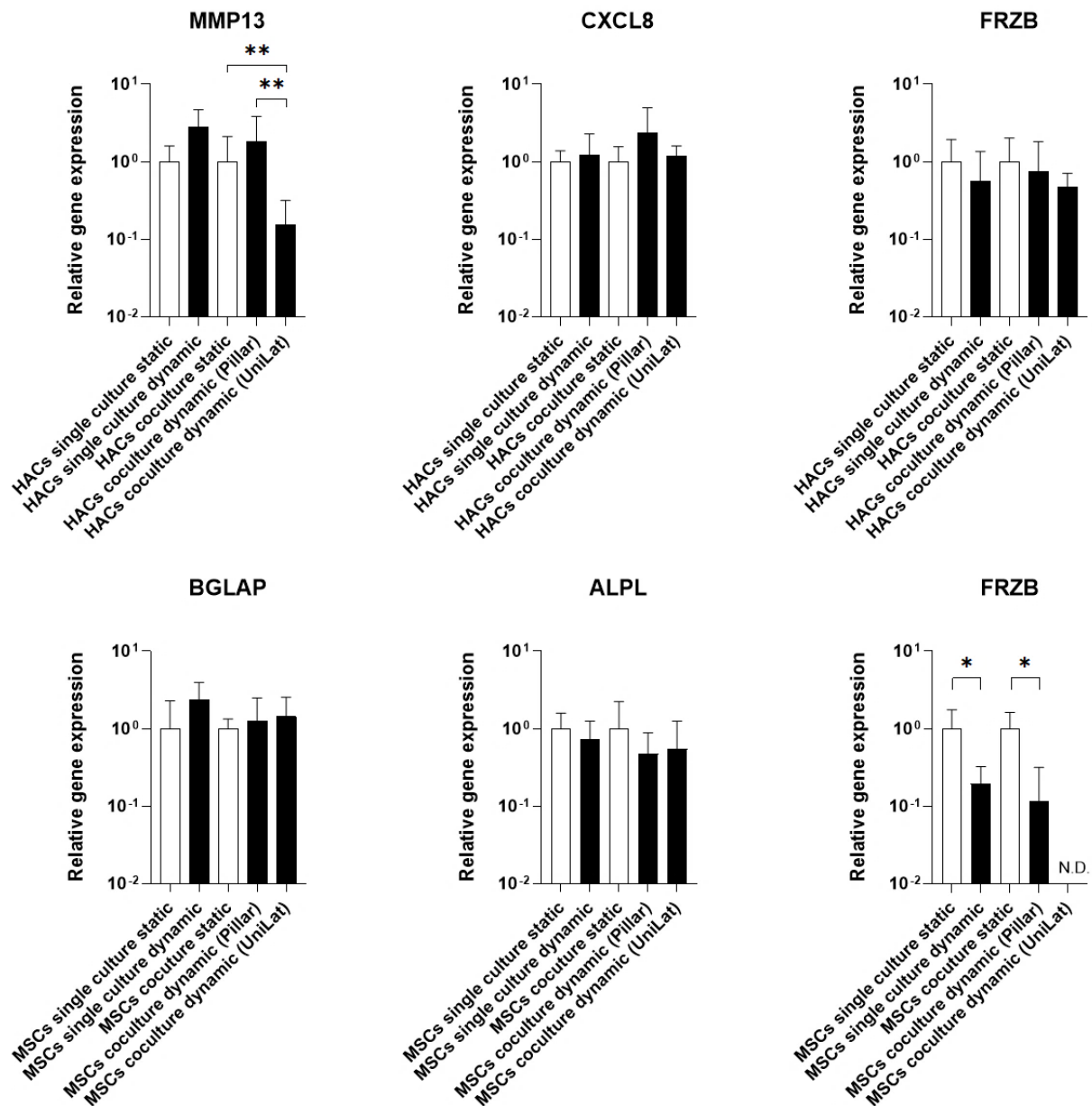
Fig. 3.9.1: *expression levels of relevant genes in cells subjected to hyperphysiological compression, relative to the expression of GAPDH. Data were normalized to the expression levels in cells cultured in static conditions; n = 6 biologically independent samples from N = 2 MSCs donors and n = 6 biologically independent samples from N = 1 HACs donor were analysed. Mean and SD are reported. Statistical significance was determined by Mann-Whitney test. * p < 0.05, ** p < 0.01.*

FRZB was not detected in any of the calcified cartilage constructs cultured in UniLat devices, due to the low amount of available genetic material.

4 DISCUSSION

OA is the most common musculoskeletal disorder in the world, with 15 million new cases diagnosed each year [2]. Currently, there are no effective disease-modifying therapies able to stop or reverse this pathology, and this lack is partly due to the absence of *in vitro* models able to recapitulate its complexity [19], [47].Traditional OA models based on monolayer cell culture provide a too simplistic description of the pathology, due to chondrocyte dedifferentiation in a 2D and ECM-free environment [19]. Several 3D models of OA at the macroscale have been developed, either cytokine-based [52]–[54] or load-based [63]–[65]. Cytokine-based models aim at the induction of OA-like biological responses in cells through their exposure to pro-inflammatory cytokines, which are present in the osteoarthritic joint following synovial inflammation. Load-based models, on the other hand, aim at recreating the condition of mechanical overloading typical of the native osteoarthritic joint. Most of the proposed macroscale systems, however, are bulky, difficult to scale up in terms of experimental throughput, and still fail to reconstitute some crucial features of native organs, including their microarchitecture, the interfaces between different tissues, and the spatiotemporal gradients of chemicals and oxygen [82], [112]. Microfluidics recently opened up new perspectives in the field of cell biology, with the introduction of pathophysiological tissue and organ models (i.e., organs-on-a-chip) with enhanced capabilities of replicating *in vivo* structures and functionalities [82], [89]. Microfluidic models allow a precise tailoring of the cellular microenvironment, and the generation of geometrically defined tissue-tissue interfaces [82], [89]. Moreover, the reduced scale determines a minimization of the transport distances and a maximization of the interfaces between different phases, enhancing the efficiency of diffusive phenomena and leading to faster and well-controlled reactions. Finally, another perk of miniaturization is the reduced consumption of reagents and analytes, which results in lower experimental costs [69], [70]. A previous study proved the feasibility of developing representative microfluidic models of OA [95]. This study, however, only focused on hyaline cartilage, while OA is widely recognized as a pathology affecting the whole joint [17], [20]. Therefore, a multi-tissue model could better recapitulate its complexity.

In this framework, the aim of the present work was to develop a 3D, multi-tissue, more representative microfluidic model of OA. For this purpose, a microfluidic device for the coculture and the mechanical stimulation of two 3D cell constructs was developed. The device was designed to simultaneously host two tissues greatly involved in OA, namely hyaline cartilage and calcified

cartilage. A direct interface is present between the two tissues, and between each tissue and the culture medium, guaranteeing an adequate diffusion of nutrients and differentiation factors. Moreover, the device allows the induction of controlled mechanical stimuli on the tissues, recreating the condition of mechanical overloading typical of OA.

The device, based on a pre-existing microfluidic platform [94], consists in three different PDMS layers, realized through soft lithography techniques: a culture chamber, an actuation membrane, and a floor. The culture chamber is composed of two central channels hosting the constructs, consisting in cell laden hydrogels, and two lateral channels for the culture medium. The gel channels are separated from the medium channels by a row of T-shaped lateral pillars hanging from the ceiling of the chamber, while a central continuous wall or a series of pillars separates the two gel channels from each other. A gap is present between the bottom surface of the wall/pillars and the underlying membrane. The membrane and the floor are sealed together forming an actuation chamber. When the actuation chamber is pressurised, the membrane bends upwards until it abuts against the wall/pillars, delivering strain-controlled compressive stimuli to the cell constructs.

Three different versions of the device were designed, varying the interface between the cell constructs and the produced mechanical stimulation. For the first version ("Pillar"), a symmetric configuration was adopted, allowing to compress both the cell constructs. A row of hanging pillars was used to separate the constructs. In the second version ("Wall"), the symmetric configuration was maintained, but the central row of pillars was substituted with a continuous wall. Finally, an asymmetric version was developed ("UniLat"), allowing to compress only the hyaline cartilage construct. A row of pillars was reintroduced to separate the two constructs, and the gap underneath the central and lateral pillars in the calcified cartilage compartment was removed.

The dimensions of the culture chamber were optimized to guarantee an adequate diffusion of nutrients within the cell constructs and to achieve the desired compression level, set to 30% according to literature [95]. The micropillars were designed to minimize the lateral expansion of cell constructs upon compression, reduce the leakage probability during the hydrogel injection (according to a modified capillary burst valve model proposed by Huang *et al.* [88]) and provide a sufficient contact surface between the constructs and the culture medium.

Finite element models of the device were implemented to evaluate the strain field within cell constructs. PDMS was described as a Mooney-Rivlin hyperelastic material, while a BPE model was adopted for the hydrogel. In general, polymeric hydrogels exhibit a non-linear, time dependent strain behaviour [113]. According to DiSilvestro *et al.* [114], a complete description of the non-

DISCUSSION

linearities should account both for the time dependency due to the flow of the interstitial fluid and for the intrinsic viscoelasticity of the solid phase. A linear Biphasic Poroviscoelastic (BPVE) model would therefore describe the hydrogel better than a BPE model. However, results by DiSilvestro *et al.* showed that, while the BPE model underestimated the reaction forces in the material, it was still sufficiently accurate in the evaluation of the strain field. Given the limited availability of parameters describing the material, a BPE description was adopted, and only strains and displacements were used as readouts.

A mesh sensitivity analysis confirmed the robustness of proposed results. However, it should be noted that a relatively large size was adopted for the elements, to ease the model convergence given the high strains considered (30%) and the rather strict lateral confinement.

Results from the computational analysis demonstrated the capacity of the lateral pillars to minimize the lateral expansion of the constructs: in the symmetric configuration of the device, the lateral strain was -0.8% ± 2.0% in the hyaline cartilage compartment and 1.7% ± 2.4% in the calcified cartilage compartment (median ± IQR); in the asymmetric device, it was 0.4% ± 3.6% in the hyaline cartilage compartment and 0.1% ± 7.4% in the calcified cartilage one. Peaks with a maximum value of 22.1% were found in the constructs, but they were limited to the regions close to the openings between subsequent pillars, while the lateral expansion was close to zero in most of the bulk volume. In both device configurations, the strain along the longitudinal direction was found to be negligible. As regards the strain along the vertical direction, the obtained values were homogeneous and in line with the design criteria for the symmetric versions of the device (namely the Pillar and Wall versions). Values of -31.3% ± 1.5% and -27.5% ± 1.6% were computed for the hyaline cartilage compartment and the calcified cartilage compartment, respectively. On the other hand, some discrepancies were found between the computed strain in the vertical direction for the asymmetric device (UniLat version) and the initial requirements. In particular, the strain in the hyaline cartilage compartment, equal to -30.2% ± 4.6%, was less homogeneous than the one obtained using the symmetric version of the device. The lateral region of the construct was subjected to a compression level close to the desired one, but in the central region the strain was remarkably lower than the target. Secondly, the strain in the calcified compartment (-17.4% ± 12.0%) was different from the target, set to zero for this device version. As a matter of fact, the mechanical stop provided by the pillars towards the actuation membrane was different from the ideal one, due to the low stiffness of PDMS. This issue could be solved increasing the cross-section of the central micropillars, or using a stiffer material (i.e., increasing the percentage of curing agent in the preparation of PDMS, or

DISCUSSION

adopting a higher curing temperature [74]). Anyway, the UniLat device was considered to represent a good compromise between the different optimal conditions required for the two tissues, and it was used without further modifications. It should also be noted that the real strain borne by the native calcified cartilage layer is low, but not zero. In late OA, in particular, a marked erosion of hyaline cartilage occurs [17], and the calcified cartilage layer becomes the main responsible for the load bearing function.

After the computational simulations, the devices were produced and characterized. The height of the pillars and the gap was measured, and used to calculate the compression level produced by the devices. This parameter served as a tool to verify the correspondence between the nominal and the actual dimensions of the geometrical features, but it was not used to assess the real strain borne by the cells, since it did not account for the mechanical properties of PDMS. The compression level was equal to 30.3% ± 2.2% for Pillar devices, 29.7% ± 2.8% for Wall devices and 31.3% ± 2.2% for UniLat devices (mean ± SD). All the values were in line with the target compression level of 30%, demonstrating the overall accuracy of the fabrication process.

Once the different device versions had been characterized, they were used to generate a cellular model of OA. Before proceeding with the full osteochondral model, comprising a hyaline cartilage compartment and a calcified cartilage compartment, a characterization of calcified cartilage constructs in single culture was performed, using a pre-existing microfluidic platform [94]. This step was necessary because, while the culture conditions to obtain HACs-based hyaline cartilage and induce OA traits in it were available [95], works focusing on calcified cartilage were lacking. Bone marrow derived MSCs were laden into enzymatically crosslinkable and cleavable eight-arm PEG hydrogels [99], and seeded into uKnee devices. Two weeks of conditioning with TGF-β3, Dexamethasone, β-Glycerophosphate and ascorbic acid induced the differentiation of MSCs into hypertrophic chondrocytes, as shown by the upregulation of genes associated with chondrogenesis (namely ACAN and COL2A1) and hypertrophy (namely COL10A1 and IHH). The upregulation of IBSP indicated a differentiation towards the terminal stage of chondrocyte hypertrophy, which is a prerequisite of endochondral ossification [115]. Moreover, the capacity of cells to produce a calcified matrix was demonstrated by the upregulation of ALPL, and confirmed by Calcein staining. ECM deposition was also monitored through phase contrast microscopy, which provided a simple and immediate readout of the tissue maturation and the cellular state. Overall, these results demonstrated the adequacy of the adopted parameters for the development of mature calcified cartilage constructs.

DISCUSSION

After two weeks of static culture, the constructs were subjected to mechanical stimulation. Hyperphysiological compression determined the downregulation of the hypertrophy inhibitor FRZB, the downregulation of the antiangiogenic factor LECT1, and the upregulation of the bone marker BGLAP. These alterations recapitulated some of the key features of the zone of calcified cartilage in a native osteoarthritic joint, namely an enhanced chondrocyte hypertrophy, a higher proneness to vascularization, and the development of regions of new bone formation [20], [27].

Another preliminary experiment was performed, to validate the strain produced by the newly developed devices. Ideally, the UniLat device should deliver a 30% compression only to the hyaline cartilage construct, while leaving the calcified cartilage construct uncompressed. However, results from computational analysis showed that the calcified cartilage construct was actually subjected to a certain amount of strain. The effect of this unwanted strain was therefore assessed. MSCs were seeded into the channel of the UniLat device designed to host calcified cartilage. The other gel channel, designed to host hyaline cartilage, was filled with a gel without any cells. The constructs were cultured in OCM for two weeks in static conditions, and for one further week in dynamic conditions. Gene expression at day 21 was compared to the one of constructs cultured for three weeks in static conditions. No relevant changes were observed between the two experimental groups, indicating that the unwanted strain borne by the constructs did not induce phenotypical changes. However, results referred to n = 3 samples from a single cell donor, and additional data would be required to come to a more reliable conclusion.

The strain produced by the Pillar version of the device was validated as well, using uKnee devices as a control. HACs were seeded into both gel channels of a Pillar device, and they were cultured in OCM for two weeks in static conditions and one further week in dynamic conditions. Gene expression at day 21 was compared to the one of constructs cultured for three weeks in static conditions and to the one of constructs subjected to mechanical stimulation in a uKnee device. No relevant changes were observed between the constructs subjected to mechanical simulation in the two different devices, demonstrating that the Pillar version was able to provide cells with the desired compression level. In both devices, hyperphysiological compression determined a slight downregulation of the chondrogenic marker ACAN, an upregulation of the catabolic marker MMP13, an upregulation of the hypertrophy markers COL10A1 and IHH, and a downregulation of the hypertrophy inhibitors GREM1 and FRZB. These results are in accordance with what was previously reported about the effect of hyperphysiological compression on hyaline cartilage constructs-on-a-chip [95]. All these modulations, however, were not statistically significant,

probably due to the low numerosity of the considered data sets: only n = 3 biologically independent samples from a single cell donor were considered, and a more reliable conclusion would need additional data.

Once the validation of the newly developed devices was complete, they were used to produce an osteochondral cell construct. First, Pillar and Wall devices were tested, to assess which device version provided the best interface between the hyaline cartilage compartment and the calcified cartilage compartment. MSCs and HACs were seeded into the devices and cultured for two weeks in static conditions in OCM. Tissue maturation was assessed through phase contrast microscopy, immunofluorescence, and gene expression analysis. Mineralization of the calcified cartilage compartment at day 14 was clearly visible from phase contrast images of the constructs, while the hyaline cartilage compartment remained uncalcified. No clear differences were visible between the two device versions in terms of interface shape. The rationale of a wall interface was the provision of a cleaner interface between constructs, which came at the cost of a lower surface contact between them. Previous works [92], [95] noticed how cells tended to adhere to hexagonal shaped pillars, forming a dense interface. This feature, that could have hindered the crosstalk between the tissues in the Pillar device, was not observed in this case. The Wall version of the device was therefore abandoned in subsequent experiments. Immunofluorescence confirmed the presence of a mineralized matrix in the calcified cartilage compartment, and its absence in the hyaline cartilage one. Moreover, it revealed the presence of aggrecan in both compartments at day 14, demonstrating the deposition of a cartilage-specific matrix. Collagen type II, another marker of chondrogenesis, was detected in the calcified cartilage construct, but not in the hyaline cartilage one. This could be a donor-dependent effect due to the low chondrogenic capacity of the HACs used in this experiment. The analysis should be repeated considering a larger pool of cell donors, to achieve a more complete assessment of ECM deposition. Gene expression levels in the constructs at day 14 were analysed through RT-qPCR, considering n = 6 biologically independent samples from N = 2 MSCs donors and n = 6 samples from N = 1 HACs donor. GFP-expressing HACs were used for these samples. Constructs were subjected to enzymatic digestion and cell sorting based on GFP expression prior to RT-qPCR, to separate HACs and MSCs-derived hypertrophic chondrocytes. This procedure determined a reduction in the amount of genetic material available for the analyses, and therefore some genes could not be detected in all the considered samples. The results revealed an upregulation of ACAN in both compartments at day 14 as compared to day 0, confirming the chondrogenic capacity of cells. The expression levels of the hypertrophy marker COL10A1, the

DISCUSSION

mineralization marker ALPL, and the bone marker IBSP were significantly higher in the calcified cartilage compartment as compared to the hyaline cartilage one, showing that HACs and MSCs-derived hypertrophic chondrocytes were able to maintain their respective gene signatures when cocultured.

After the assessment of their maturation, the osteochondral constructs were subjected to mechanical stimulation, to assess the induction of OA-like phenotypical changes and analyse possible effects of the crosstalk between the two compartments. Two weeks of static culture and one additional week of dynamic culture in OCM were carried on. Gene expression at day 21 was analysed, considering n = 6 biologically independent samples from N = 2 MSCs donors and n = 6 samples from N = 1 HACs donor. Also in this case, expression levels of some genes of interest could not be analysed in all the considered samples, due to the low amount of genetic material available after cell sorting. In Pillar devices, hyperphysiological compression induced the upregulation of the catabolic marker MMP13, the upregulation of the inflammation marker CXCL8, and the downregulation of the hypertrophy inhibitor FRZB in the hyaline cartilage compartment. All these modulations were not statistically significant, probably due to the low numerosity of the considered data sets. No relevant changes were observed as compared to the single culture controls. The obtained trends were in accordance with what was previously reported about the effect of hyperphysiological compression on hyaline cartilage constructs-on-a-chip [95], but the modulations were less marked in this case. Such differences could be due to the different compositions of culture media used in the present work and in the work by Occhetta *et al.* In particular, the use of Dexamethasone in the present work could have reduced the effect of hyperphysiological compression in terms of an enhanced inflammatory and catabolic activity [116]. This hypothesis could be backed up by the fact that, while the upregulation of MMP13 and CXCL8 was present but limited, hypertrophy-related markers, which were demonstrated to be affected by hyperphysiological compression but not by Dexamethasone, showed higher modulation levels. Different medium compositions could be adopted for the week of dynamic culture and the two weeks of static culture, to boost the effect of the mechanical stimulation and still be able to guarantee the correct maturation of the cell constructs. In UniLat devices, the effect of mechanical stimulation on the expression of CXCL8 and FRZB was similar to the one observed in Pillar devices. However, a significant downregulation of MMP13 was observed, in contrast with the results obtained for the Pillar version. This could be due to the fact that the compression level produced by the UniLat device in the hyaline cartilage compartment was not homogenous, and cells located in

the region close to the central pillars were exposed to low compressive stimuli, which are known to enhance chondrocyte anabolism, rather than catabolism [65], [94]. Alternatively, this effect could be due to factors released by the MSCs-derived hypertrophic chondrocytes in the calcified compartment, which were subjected to even lower mechanical stimuli. In any case, further studies are required to come to more reliable conclusions.

As regards the calcified cartilage compartment, the hyperphysiological compression induced by Pillar devices determined a slight upregulation of the bone marker BGLAP, a slight downregulation of the mineralization marker ALPL, and a marked downregulation of the hypertrophy inhibitor FRZB. Only the results referring to FRZB were statistically significant, while the low numerosity of data sets probably prevented the achievement of statistical significance for ALPL and BGLAP. The modulation of FRZB was in line with the one observed in single culture controls. BGLAP and ALPL were respectively less and more modulated as compared to single culture controls, suggesting a possible effect of coculture on gene expression. Further studies considering a larger pool of cell donors would be needed to confirm this hypothesis. In UniLat devices, FRZB could not be detected in any of the analysed calcified cartilage constructs, due to the low amount of genetic material obtained after cell sorting. The effect of mechanical stimulation on the expression of ALPL and BGLAP in this device version was similar to the one observed in Pillar devices. Notably, these results were in contrast with those obtained from the strain validation of the UniLat device, which did not underline any modulations in the constructs subjected to mechanical stimulation as compared to the static controls. Also this discrepancy could be an effect of coculture, but further studies are needed to come to a reliable conclusion.

Overall, the microfluidic devices developed in the present work were able to provide the cell laden hydrogels with a 3D environment and an adequate biochemical conditioning, allowing the maturation of multi-tissue osteochondral constructs. Furthermore, the devices were used to expose the constructs to cyclic hyperphysiological compression, recreating the condition of mechanical overloading typical of the native osteoarthritic joint. The UniLat version of the device produced contraddictory results, while the Pillar version allowed to replicate some hallmarks of OA, such as chondrocyte hypertrophy, catabolism, and inflammation in hyaline cartilage, and hypertrophy and proneness to bone formation in calcified cartilage. Further studies are needed to achieve a complete understanding and an accurate modelling of OA, but the results of the present work represent a useful starting point, both for basic research and for the evaluation of possible anti-OA therapies.

5 CONCLUSIONS AND FUTURE DEVELOPMENTS

A mechanically active, PDMS-based microfluidic device was designed, fabricated, and successfully exploited to generate 3D multi-tissue osteochondral constructs, consisting in PEG-based hydrogels laden with HACs or MSCs. The device guaranteed an adequate diffusion of nutrients and differentiation factors within the constructs and was compatible with medium-long term cell culture. Furthermore, it was able to provide the constructs with defined compressive stimuli, resembling the condition of mechanical overloading typical of the native osteoarthritic joint. Finally, the device allowed to perform a wide range of analyses on the constructs, both on-line (e.g., phase contrast microscopy, Calcein staining) and at the end of the culture period (e.g., RT-qPCR, immunofluorescence). In particular, compatibility with phase contrast microscopy provided a simple and immediate readout of the tissue maturation and the cellular state. Biological results demonstrated the feasibility of developing microscale osteochondral constructs composed of two distinct compartments, representing hyaline cartilage and calcified cartilage. Moreover, the application of cyclic hyperphysiological compression on the constructs allowed to replicate some hallmarks of OA, such as chondrocyte hypertrophy, catabolism, and inflammation in hyaline cartilage, and hypertrophy and proneness to bone formation in calcified cartilage.

In parallel with the main work, a characterization of calcified cartilage constructs in single culture was performed, using a pre-existing microfluidic platform [94]. Biological results from this side work provided the culture parameters for the successful development of mature calcified cartilage constructs from bone marrow derived MSCs. Moreover, the application of cyclic hyperphysiological compression on the constructs allowed to replicate some key features of the zone of calcified cartilage in a native osteoarthritic joint, such as an enhanced chondrocyte hypertrophy, a higher proneness to vascularization and the development of regions of new bone formation.

The results of the present work shed some light on the role of calcified cartilage in OA, representing a useful starting point both for basic research and for the evaluation of possible anti-OA therapies. A repetition of the performed experiments, considering a larger pool of cell donors and samples, is required to confirm the obtained results and achieve more statistical significance. Moreover, further analyses could be conducted, e.g., a more exhaustive characterization of ECM composition, a quantification of the substances released by the constructs into the supernatant, or a direct comparison between the constructs and the native joint tissues in terms of gene expression.

CONCLUSIONS AND FUTURE DEVELOPMENTS

A further step could be a pharmacological validation of the model. First, the effect of well-characterized drugs on the constructs could be tested, to assess the reliablity of the model as a screening tool. After an exhaustive validation, the model could then be used to test possible innovative anti-OA therapies, targeting different aspects of the pathology not recapitulated by previous models (e.g., the advancement of bone formation in the deeper cartilage layers). Another future perspective could be the introduction in the model of additional elements involved in OA, such as vasculature. This would provide insight into the underlying mechanisms of OA, and a deeper understanding of its pathogenesis. However, the addition of other cell types allowing the formation of a microvascular network, such as human umbilical vein endothelial cells (HUVECs) [96], [117], would require a further optimization of the culture parameters. Finally, a desirable feature would be the possibility to use different medium compositions for the different tissues cultured in the device. This feature is not strictly necessary when coculturing hyaline cartilage and calcified cartilage only, since the present work demonstrated the feasibility of obtaining both tissues with a single medium composition, but it could be needed for the introduction in the model of additional cell types. To achieve this requirement, the microfluidic device could be integrated with a perfusion system able to generate a continuous flow of medium in its lateral channels, and a stable gradient between the two hydrogel compartments.

All the applications mentioned so far could be realized without further modifications of the current device design. However, design modifications would open up even larger possibilities. A new design, for instance, could allow the achievement of a strain field more representative of the one found in the native joint. In fact, given the anatomy of the native osteochondral unit, the hyaline cartilage layer and the calcified cartilage layer are compressed "in series", while the device developed in the present work allows the application of mechanical stimuli "in parallel". A drawback of the presented approach, therefore, is the fact that the two tissues are subjected to the same compression level. While the UniLat device version was developed to deliver different compressive stimuli to the two tissues, the produced strain field was not perfectly in line with the project requirements, and the biological results obtained with this design were contraddictory. However, to achieve a real compression "in series", the number of PDMS layers composing the microfluidic device should probaly be increased, and the design of the single layers further optimized.

Overall, the introduction of these features in a microfluidic device would represent a further step towards the development of a model of joint-on-a-chip, able to fully recapitulate *in vitro* the complexity of OA.

6 BIBLIOGRAPHY

[1]   S. Glyn-Jones *et al.*, "Osteoarthritis," *Lancet*, vol. 386, no. 9991, pp. 376–387, 2015, doi: 10.1016/S0140-6736(14)60802-3.

[2]   M. Kloppenburg and F. Berenbaum, "Osteoarthritis year in review 2019: epidemiology and therapy," *Osteoarthr. Cartil.*, vol. 28, no. 3, pp. 242–248, 2020, doi: 10.1016/j.joca.2020.01.002.

[3]   Y. Zhang and J. M. Jordan, "Epidemiology of osteoarthritis," *Clin. Geriatr. Med.*, vol. 26, no. 3, pp. 355–369, 2010, doi: 10.1016/j.cger.2010.03.001.

[4]   L. March, M. Cross, N. Arden, and G. Hawker, "Osteoarthritis: A Serious Disease, Submitted to the U. S. Food and Drug Administration," *Oarsi*, pp. 1–103, 2016.

[5]   J. L. C. M. Van Saase, L. K. J. Van Romunde, A. Cats, J. P. VanDenBroucke, and H. A. Valkenburg, "Epidemiology of osteoarthritis: Zoetermeer survey. Comparison of radiological osteoarthritis in a Dutch population with that in 10 other populations," *Ann. Rheum. Dis.*, vol. 48, no. 4, pp. 271–280, 1989, doi: 10.1136/ard.48.4.271.

[6]   S. Van Der Pas *et al.*, "European project on osteoarthritis: Design of a six-cohort study on the personal and societal burden of osteoarthritis in an older European population," *BMC Musculoskelet. Disord.*, vol. 14, 2013, doi: 10.1186/1471-2474-14-138.

[7]   M. Hiligsmann *et al.*, "Health economics in the field of osteoarthritis: An Expert's consensus paper from the European Society for Clinical and Economic Aspects of Osteoporosis and Osteoarthritis (ESCEO)," *Semin. Arthritis Rheum.*, vol. 43, no. 3, pp. 303–313, 2013, doi: 10.1016/j.semarthrit.2013.07.003.

[8]   A. J. Hall, B. Stubbs, M. A. Mamas, P. K. Myint, and T. O. Smith, "Association between osteoarthritis and cardiovascular disease: Systematic review and meta-analysis," *Eur. J. Prev. Cardiol.*, vol. 23, no. 9, pp. 938–946, 2015, doi: 10.1177/2047487315610663.

[9]   N. Arden and M. C. Nevitt, "Osteoarthritis: Epidemiology," *Best Pract. Res. Clin. Rheumatol.*, vol. 20, no. 1, pp. 3–25, 2006, doi: 10.1016/j.berh.2005.09.007.

[10]   S. L. James *et al.*, "Global, regional, and national incidence, prevalence, and years lived with disability for 354 Diseases and Injuries for 195 countries and territories, 1990-2017: A systematic analysis for the Global Burden of Disease Study 2017," *Lancet*, vol. 392, no. 10159, pp. 1789–1858, 2018, doi: 10.1016/S0140-6736(18)32279-7.

[11]   L. Sharma *et al.*, "Laxity in healthy and osteoarthritic knees," *Arthritis Rheum.*, vol. 42, no. 5, pp. 861–870, 1999, doi: 10.1002/1529-0131(199905)42:5<861::AID-ANR4>3.0.CO;2-N.

[12]   T. D. Spector, D. Nandra, D. J. Hart, and D. V. Doyle, "Is hormone replacement therapy protective for hand and knee osteoarthritis in women?: The Chingford Study," *Ann. Rheum. Dis.*, vol. 56, no. 7, pp. 432–434, 1997, doi: 10.1136/ard.56.7.432.

[13]   M. T. Hannan, D. T. Felson, J. J. Anderson, A. Naimark, and W. B. Kannel, "Estrogen use and radiographic osteoarthritis of the knee in women," *Arthritis Rheum.*, vol. 33, no. 4, pp. 525–532, 1990, doi: 10.1002/art.1780330410.

[14]   S. A. Oliveria, D. T. Felson, P. A. Cirillo, J. I. Reed, and A. M. Walker, "Body weight, body mass index, and incident symptomatic osteoarthritis of the hand, hip, and knee," *Epidemiology*, vol. 10, no. 2, pp. 161–166, 1999, doi: 10.1097/00001648-199903000-00013.

[15]   A. C. Gelber, M. C. Hochberg, L. A. Mead, N. Y. Wang, F. M. Wigley, and M. J. Klag, "Body mass index in young men and the risk of subsequent knee and hip osteoarthritis," *Am. J. Med.*, vol. 107, no. 6, pp. 542–548, 1999, doi: 10.1016/S0002-9343(99)00292-2.

[16]   W. J. Carman, M. Sowers, V. M. Hawthorne, and L. A. Weissfeld, "Obesity as a Risk Factor for Osteoarthritis of the Hand and Wrist: A Prospective Study," *Am. J. Epidemiol.*, vol. 139, no. 2,

pp. 119–129, 1994, doi: 10.1016/s0016-0032(40)90500-2.

[17] K. P. H. Pritzker *et al.*, "Osteoarthritis cartilage histopathology: Grading and staging," *Osteoarthr. Cartil.*, vol. 14, no. 1, pp. 13–29, 2006, doi: 10.1016/j.joca.2005.07.014.

[18] L. J. Sandell and T. Aigner, "Articular cartilage and changes in arthritis. An introduction: Cell biology of osteoarthritis," *Arthritis Res. Ther.*, vol. 3, no. 107, 2001, doi: 10.1186/ar148.

[19] C. I. Johnson, D. J. Argyle, and D. N. Clements, "In vitro models for the study of osteoarthritis," *Vet. J.*, vol. 209, pp. 40–49, 2016, doi: 10.1016/j.tvjl.2015.07.011.

[20] S. R. Goldring and M. B. Goldring, "Changes in the osteochondral unit during osteoarthritis: Structure, function and cartilage bone crosstalk," *Nat. Rev. Rheumatol.*, vol. 12, no. 11, pp. 632–644, 2016, doi: 10.1038/nrrheum.2016.148.

[21] S. L. Dunn, J. Soul, S. Anand, J. M. Schwartz, R. P. Boot-Handford, and T. E. Hardingham, "Gene expression changes in damaged osteoarthritic cartilage identify a signature of non-chondrogenic and mechanical responses," *Osteoarthr. Cartil.*, vol. 24, no. 8, pp. 1431–1440, 2016, doi: 10.1016/j.joca.2016.03.007.

[22] X. Zhang, I. Prasadam, W. Fang, R. Crawford, and Y. Xiao, "Chondromodulin-1 ameliorates osteoarthritis progression by inhibiting HIF-2α activity," *Osteoarthr. Cartil.*, vol. 24, no. 11, pp. 1970–1980, 2016, doi: 10.1016/j.joca.2016.06.005.

[23] D. Pfander, T. Cramer, D. Deuerling, G. Weseloh, and B. Swoboda, "Expression of thrombospondin-1 and its receptor CD36 in human osteoarthritic cartilage," *Ann. Rheum. Dis.*, vol. 59, no. 6, pp. 448–454, 2000, doi: 10.1136/ard.59.6.448.

[24] S. A. Fenwick, P. J. Gregg, and P. Rooney, "Osteoarthritic cartilage loses its ability to remain avascular," *Osteoarthr. Cartil.*, vol. 7, no. 5, pp. 441–452, 1999, doi: 10.1053/joca.1998.0238.

[25] D. A. Walsh *et al.*, "Angiogenesis and nerve growth factor at the osteochondral junction in rheumatoid arthritis and osteoarthritis," *Rheumatology*, vol. 49, no. 10, pp. 1852–1861, 2010, doi: 10.1093/rheumatology/keq188.

[26] P. A. Simkin, "Consider the tidemark," *J. Rheumatol.*, vol. 39, no. 5, pp. 890–892, 2012, doi: 10.3899/jrheum.110942.

[27] S. Suri and D. A. Walsh, "Osteochondral alterations in osteoarthritis," *Bone*, vol. 51, no. 2, pp. 204–211, 2012, doi: 10.1016/j.bone.2011.10.010.

[28] G. Li *et al.*, "Subchondral bone in osteoarthritis: Insight into risk factors and microstructural changes," *Arthritis Res. Ther.*, vol. 15, no. 6, 2013, doi: 10.1186/ar4405.

[29] L. A. Pottenger, F. M. Phillips, and L. F. Draganich, "The effect of marginal osteophytes on reduction of varus-valgus instability in osteoarthritic knees," *Arthritis Rheum.*, vol. 33, no. 6, pp. 853–858, 1990, doi: 10.1002/art.1780330612.

[30] A. Mathiessen and P. G. Conaghan, "Synovitis in osteoarthritis: Current understanding with therapeutic implications," *Arthritis Res. Ther.*, vol. 19, no. 1, pp. 1–9, 2017, doi: 10.1186/s13075-017-1229-9.

[31] M. J. Benito, D. J. Veale, O. FitzGerald, W. B. Van Den Berg, and B. Bresnihan, "Synovial tissue inflammation in early and late osteoarthritis," *Ann. Rheum. Dis.*, vol. 64, no. 9, pp. 1263–1267, 2005, doi: 10.1136/ard.2004.025270.

[32] S. Grässel and D. Muschter, "Recent advances in the treatment of osteoarthritis," *F1000Research*, vol. 9, no. May, 2020, doi: 10.12688/f1000research.22115.1.

[33] "Regenerative medicine." www.nature.com/subjects/regenerative-medicine (accessed Mar. 10, 2021).

[34] J. Malda, J. Boere, C. H. A. Van De Lest, P. R. Van Weeren, and M. H. M. Wauben, "Extracellular vesicles - New tool for joint repair and regeneration," *Nat. Rev. Rheumatol.*, vol. 12, no. 4, pp. 243–249, 2016, doi: 10.1038/nrrheum.2015.170.

[35] W. Bartlett *et al.*, "Autologous chondrocyte implantation versus matrix-induced autologous

chondrocyte implantation for osteochondral defects of the knee. A prospective, randomised study," *J. Bone Jt. Surg. - Ser. B*, vol. 87, no. 5, pp. 640–645, 2005, doi: 10.1302/0301-620X.87B5.15905.

[36]   L. Acevedo *et al.*, "Performance of nasal chondrocytes in an osteoarthritic environment," *Osteoarthr. Cartil.*, vol. 26, no. 2018, pp. S37–S38, 2018, doi: 10.1016/j.joca.2018.02.091.

[37]   M. Mumme *et al.*, "Regenerative Potential of Tissue-Engineered Nasal Chondrocytes in Goat Articular Cartilage Defects," *Tissue Eng. - Part A*, vol. 22, no. 21–22, pp. 1286–1295, 2016, doi: 10.1089/ten.tea.2016.0159.

[38]   J. C. Mansfield, V. Mandalia, A. Toms, C. Peter Winlove, and S. Brasselet, "Collagen reorganization in cartilage under strain probed by polarization sensitive second harmonic generation microscopy," *J. R. Soc. Interface*, vol. 16, no. 150, 2019, doi: 10.1098/rsif.2018.0611.

[39]   F. Boschetti, G. Pennati, F. Gervaso, G. M. Peretti, and G. Dubini, "Biomechanical properties of human articular cartilage under compressive loads," *Biorheology*, vol. 41, no. 3–4, pp. 159–166, 2004.

[40]   T. R. Oegema, R. J. Carpenter, F. Hofmeister, and R. C. Thompson, "The interaction of the zone of calcified cartilage and subchondral bone in osteoarthritis," *Microsc. Res. Tech.*, vol. 37, no. 4, pp. 324–332, 1997, doi: 10.1002/(SICI)1097-0029(19970515)37:4<324::AID-JEMT7>3.0.CO;2-K.

[41]   P. L. Mente and J. L. Lewis, "Elastic modulus of calcified cartilage is an order of magnitude less than that of subchondral bone," *J. Orthop. Res.*, vol. 12, no. 5, pp. 637–647, 1994, doi: 10.1002/jor.1100120506.

[42]   F. Eckstein *et al.*, "In vivo cartilage deformation after different types of actvity and its dependence on physical training status," *Ann. Rheum. Dis.*, vol. 64, no. 2, pp. 291–295, 2005, doi: 10.1136/ard.2004.022400.

[43]   Y. P. Zheng, A. F. T. Mak, K. P. Lau, and L. Qin, "An ultrasonic measurement for in vitro depth-dependent equilibrium strains of articular cartilage in compression," *Phys. Med. Biol.*, vol. 47, no. 17, pp. 3165–3180, 2002, doi: 10.1088/0031-9155/47/17/308.

[44]   D. D. Chan, L. Cai, K. D. Butz, S. B. Trippel, E. A. Nauman, and C. P. Neu, "In vivo articular cartilage deformation: Noninvasive quantification of intratissue strain during joint contact in the human knee," *Sci. Rep.*, vol. 6, no. January, pp. 1–14, 2016, doi: 10.1038/srep19220.

[45]   L. P. Li, M. D. Buschmann, and A. Shirazi-Adl, "Strain-rate dependent stiffness of articular cartilage in unconfined compression," *J. Biomech. Eng.*, vol. 125, no. 2, pp. 161–168, 2003, doi: 10.1115/1.1560142.

[46]   L. L. Gao, X. Y. Qin, C. Q. Zhang, H. Gao, H. Y. Ge, and X. Z. Zhang, "Ratcheting behavior of articular cartilage under cyclic unconfined compression," *Mater. Sci. Eng. C*, vol. 57, pp. 371–377, 2015, doi: 10.1016/j.msec.2015.07.061.

[47]   P. J. Cope, K. Ourradi, Y. Li, and M. Sharif, "Models of osteoarthritis: the good, the bad and the promising," *Osteoarthr. Cartil.*, vol. 27, no. 2, pp. 230–239, 2019, doi: 10.1016/j.joca.2018.09.016.

[48]   J. C. Madden, M. Hewitt, K. Przybylak, R. J. Vandebriel, A. H. Piersma, and M. T. D. Cronin, "Strategies for the optimisation of in vivo experiments in accordance with the 3Rs philosophy," *Regul. Toxicol. Pharmacol.*, vol. 63, no. 1, pp. 140–154, 2012, doi: 10.1016/j.yrtph.2012.03.010.

[49]   B. Yang *et al.*, "Effect of microRNA-145 on IL-1β-induced cartilage degradation in human chondrocytes," *FEBS Lett.*, vol. 588, no. 14, pp. 2344–2352, 2014, doi: 10.1016/j.febslet.2014.05.033.

[50]   L. Allas, Q. Rochoux, S. Leclercq, K. Boumédiene, and C. Baugé, "Development of a simple

osteoarthritis model useful to predict in vitro the anti-hypertrophic action of drugs," *Lab. Investig.*, vol. 100, no. 1, pp. 64–71, 2020, doi: 10.1038/s41374-019-0303-0.

[51] M. M. J. Caron *et al.*, "Redifferentiation of dedifferentiated human articular chondrocytes: Comparison of 2D and 3D cultures," *Osteoarthr. Cartil.*, vol. 20, no. 10, pp. 1170–1178, 2012, doi: 10.1016/j.joca.2012.06.016.

[52] M. Beekhuizen *et al.*, "Osteoarthritic synovial tissue inhibition of proteoglycan production in human osteoarthritic knee cartilage: Establishment and characterization of a long-term cartilage-synovium coculture," *Arthritis Rheum.*, vol. 63, no. 7, pp. 1918–1927, 2011, doi: 10.1002/art.30364.

[53] S. Francioli, C. Cavallo, B. Grigolo, I. Martin, and A. Barbero, "Engineered cartilage maturation regulates cytokine production and interleukin-1β response," *Clin. Orthop. Relat. Res.*, vol. 469, no. 10, pp. 2773–2784, 2011, doi: 10.1007/s11999-011-1826-x.

[54] L. Sun, X. Wang, and D. L. Kaplan, "A 3D cartilage - Inflammatory cell culture system for the modeling of human osteoarthritis," *Biomaterials*, vol. 32, no. 24, pp. 5581–5589, 2011, doi: 10.1016/j.biomaterials.2011.04.028.

[55] E. Pecchi *et al.*, "A potential role of chondroitin sulfatfrancise on bone in osteoarthritis: Inhibition of prostaglandin E 2 and matrix metalloproteinases synthesis in interleukin-1β-stimulated osteoblasts," *Osteoarthr. Cartil.*, vol. 20, no. 2, pp. 127–135, 2012, doi: 10.1016/j.joca.2011.12.002.

[56] Y. Ake, Y. Saegusa, T. Matsubara, and K. Mizuno, "Cultured osteoblast synthesize nitric oxide in response to cytokines and lipopolysaccharide," *Kobe J. Med. Sci.*, vol. 40, no. 3–4, pp. 125–137, 1994, [Online]. Available: http://europepmc.org/abstract/MED/7739201.

[57] H. Lin, T. P. Lozito, P. G. Alexander, R. Gottardi, and R. S. Tuan, "Stem cell-based microphysiological osteochondral system to model tissue response to interleukin-1B," *Mol. Pharm.*, vol. 11, no. 7, pp. 2203–2212, 2014, doi: 10.1021/mp500136b.

[58] D. L. Bader, D. M. Salter, and T. T. Chowdhury, "Biomechanical Influence of Cartilage Homeostasis in Health and Disease," *Arthritis*, vol. 2011, pp. 1–16, 2011, doi: 10.1155/2011/979032.

[59] W. Lee, F. Guilak, and W. Liedtke, *Role of Piezo Channels in Joint Health and Injury*, vol. 79. Elsevier Ltd, 2017.

[60] J. Sanchez-Adams, H. A. Leddy, A. L. McNulty, C. J. O'Conor, and F. Guilak, "The Mechanobiology of Articular Cartilage: Bearing the Burden of Osteoarthritis," *Curr. Rheumatol. Rep.*, vol. 16, no. 10, pp. 1–9, 2014, doi: 10.1007/s11926-014-0451-6.

[61] R. Ruhlen and K. Marberry, "The chondrocyte primary cilium.," *Osteoarthr. Cartil.*, vol. 22, no. 8, pp. 1071–1076, Aug. 2014, doi: 10.1016/j.joca.2014.05.011.

[62] R. C. Murray, S. Vedi, H. L. Birch, K. H. Lakhani, and A. E. Goodship, "Subchondral bone thickness, hardness and remodelling are influenced by short-term exercise in a site-specific manner," *J. Orthop. Res.*, vol. 19, no. 6, pp. 1035–1042, 2001, doi: 10.1016/S0736-0266(01)00027-4.

[63] J. B. Fitzgerald, M. Jin, D. Dean, D. J. Wood, M. H. Zheng, and A. J. Grodzinsky, "Mechanical Compression of Cartilage Explants Induces Multiple Time-dependent Gene Expression Patterns and Involves Intracellular Calcium and Cyclic AMP," *J. Biol. Chem.*, vol. 279, no. 19, pp. 19502–19511, 2004, doi: 10.1074/jbc.M400437200.

[64] J. N. A. De Croos, S. S. Dhaliwal, M. D. Grynpas, R. M. Pilliar, and R. A. Kandel, "Cyclic compressive mechanical stimulation induces sequential catabolic and anabolic gene changes in chondrocytes resulting in increased extracellular matrix accumulation," *Matrix Biol.*, vol. 25, no. 6, pp. 323–331, 2006, doi: 10.1016/j.matbio.2006.03.005.

[65] I. C. Young *et al.*, "A novel compressive stress-based osteoarthritis-like chondrocyte system,"

Exp. Biol. Med., vol. 242, no. 10, pp. 1062–1071, 2017, doi: 10.1177/1535370217699534.

[66] M. Vazquez *et al.*, "A new method to investigate how mechanical loading of osteocytes controls osteoblasts," *Front. Endocrinol. (Lausanne).*, vol. 5, no. DEC, pp. 1–18, 2014, doi: 10.3389/fendo.2014.00208.

[67] Y. Y. Lin *et al.*, "Applying an excessive mechanical stress alters the effect of subchondral osteoblasts on chondrocytes in a co-culture system," *Eur. J. Oral Sci.*, vol. 118, no. 2, pp. 151–158, 2010, doi: 10.1111/j.1600-0722.2010.00710.x.

[68] G. M. Whitesides, "The origins and the future of microfluidics," *Nature*, vol. 442, no. 7101, pp. 368–373, 2006, doi: 10.1038/nature05058.

[69] J. C. McDonald *et al.*, "Fabrication of microfluidic systems in poly-dimethylsiloxane," *Electrophoresis*, vol. 21, no. 1, pp. 27–40, 2000.

[70] P. Occhetta, M. Centola, B. Tonnarelli, A. Redaelli, I. Martin, and M. Rasponi, "High-throughput microfluidic platform for 3D cultures of mesenchymal stem cells, towards engineering developmental processes," *Sci. Rep.*, vol. 5, no. April, pp. 1–12, 2015, doi: 10.1038/srep10288.

[71] S. K. Sia and G. M. Whitesides, "Microfluidic devices fabricated in poly(dimethylsiloxane) for biological studies," *Electrophoresis*, vol. 24, no. 21, pp. 3563–3576, 2003, doi: 10.1002/elps.200305584.

[72] D. Qin, Y. Xia, and G. M. Whitesides, "Soft lithography for micro- and nanoscale patterning," *Nat. Protoc.*, vol. 5, no. 3, pp. 491–502, 2010, doi: 10.1038/nprot.2009.234.

[73] J. M. K. Ng, A. D. Stroock, and G. M. Whitesides, "Components for integrated poly (dimethylsiloxane) microfluidic systems," *Electrophoresis*, vol. 23, no. 20, pp. 3461–3473, 2002.

[74] I. D. Johnston, D. K. McCluskey, C. K. L. Tan, and M. C. Tracey, "Mechanical characterization of bulk Sylgard 184 for microfluidics and microengineering," *J. Micromechanics Microengineering*, vol. 24, no. 3, 2014, doi: 10.1088/0960-1317/24/3/035017.

[75] A. Mata, A. J. Fleischman, and S. Roy, "Characterization of Polydimethylsiloxane (PDMS) Properties for Biomedical Micro/Nanosystems," *Biomed. Microdevices*, vol. 7, no. 4, pp. 281–293, 2005, doi: 10.1007/s10544-005-6070-2.

[76] M. H. Madsen, N. A. Feidenhans'l, P. E. Hansen, J. Garnæs, and K. Dirscherl, "Accounting for PDMS shrinkage when replicating structures," *J. Micromechanics Microengineering*, vol. 24, no. 12, 2014, doi: 10.1088/0960-1317/24/12/127002.

[77] V. Linder, E. Verpoorte, N. F. De Rooij, H. Sigrist, and W. Thormann, "Application of surface biopassivated disposable poly(dimethylsiloxane)/glass chips to a heterogeneous competitive human serum immunoglobulin G immunoassay with incorporated internal standard," *Electrophoresis*, vol. 23, no. 5, pp. 740–749, 2002, doi: 10.1002/1522-2683(200203)23:5<740::AID-ELPS740>3.0.CO;2-7.

[78] R. F. Ismagilov, J. M. K. Ng, P. J. A. Kenis, and G. M. Whitesides, "Microfluidic arrays of fluid-fluid diffusional contacts as detection elements and combinatorial tools," *Anal. Chem.*, vol. 73, no. 21, pp. 5207–5213, 2001, doi: 10.1021/ac010502a.

[79] C. S. Effenhauser, G. J. M. Bruin, A. Paulus, and M. Ehrat, "Integrated Capillary Electrophoresis on Flexible Silicone Microdevices: Analysis of DNA Restriction Fragments and Detection of Single DNA Molecules on Microchips," *Anal. Chem.*, vol. 69, no. 17, pp. 3451–3457, 1997, doi: 10.1021/ac9703919.

[80] A. R. Wheeler *et al.*, "Microfluidic Device for Single-Cell Analysis," *Anal. Chem.*, vol. 75, no. 14, pp. 3581–3586, 2003.

[81] N. Li Jeon, H. Baskaran, S. K. W. Dertinger, G. M. Whitesides, L. Van de Water, and M. Toner, "Neutrophil chemotaxis in linear and complex gradients of interleukin-8 formed in a

microfabricated device.," *Nat. Biotechnol.*, vol. 20, no. 8, pp. 826–830, Aug. 2002, doi: 10.1038/nbt712.

[82] D. Huh, G. A. Hamilton, and D. E. Ingber, "From 3D cell culture to organs-on-chips," *Trends Cell Biol.*, vol. 21, no. 12, pp. 745–754, 2011, doi: 10.1016/j.tcb.2011.09.005.

[83] K. J. Jang, H. S. Cho, D. H. Kang, W. G. Bae, T. H. Kwon, and K. Y. Suh, "Fluid-shear-stress-induced translocation of aquaporin-2 and reorganization of actin cytoskeleton in renal tubular epithelial cells," *Integr. Biol.*, vol. 3, no. 2, pp. 134–141, 2011, doi: 10.1039/c0ib00018c.

[84] P. J. Lee, P. J. Hung, and L. P. Lee, "An Artificial Liver Sinusoid With a Microfluidic Endothelial-Like Barrier for Primary Hepatocyte Culture," *Biotechnol. Bioeng.*, vol. 97, no. 5, pp. 1340–1346, 2007, doi: 10.1002/bit.

[85] I. K. Zervantonakis, C. R. Kothapalli, S. Chung, R. Sudo, and R. D. Kamm, "Microfluidic devices for studying heterotypic cell-cell interactions and tissue specimen cultures under controlled microenvironments," *Biomicrofluidics*, vol. 5, no. 1, pp. 1–14, 2011, doi: 10.1063/1.3553237.

[86] M. W. Tibbitt and K. S. Anseth, "Hydrogels as extracellular matrix mimics for 3D cell culture," *Biotechnol. Bioeng.*, vol. 103, no. 4, pp. 655–663, 2009, doi: 10.1002/bit.22361.

[87] S. M. Ong *et al.*, "A gel-free 3D microfluidic cell culture system," *Biomaterials*, vol. 29, no. 22, pp. 3237–3244, 2008, doi: 10.1016/j.biomaterials.2008.04.022.

[88] C. P. Huang *et al.*, "Engineering microscale cellular niches for three-dimensional multicellular co-cultures," *Lab Chip*, vol. 9, no. 12, pp. 1740–1748, 2009, doi: 10.1038/jid.2014.371.

[89] D. Huh, B. D. Matthews, A. Mammoto, M. Montoya-Zavala, H. Y. Hsin, and D. E. Ingber, "Reconstituting Organ-Level Lung Functions on a Chip," *Science (80-.).*, vol. 328, no. 5986, pp. 1662–1668, 2010.

[90] S. Musah *et al.*, "Mature induced-pluripotent-stem-cell-derived human podocytes reconstitute kidney glomerular-capillary-wall function on a chip," *Nat. Biomed. Eng.*, vol. 1, no. 5, 2017, doi: 10.1038/s41551-017-0069.

[91] H. J. Kim, H. Li, J. J. Collins, and D. E. Ingber, "Contributions of microbiome and mechanical deformation to intestinal bacterial overgrowth and inflammation in a human gut-on-a-chip," *Proc. Natl. Acad. Sci. U. S. A.*, vol. 113, no. 1, pp. E7–E15, 2016, doi: 10.1073/pnas.1522193112.

[92] A. Marsano *et al.*, "Beating heart on a chip: A novel microfluidic platform to generate functional 3D cardiac microtissues," *Lab Chip*, vol. 16, no. 3, pp. 599–610, 2016, doi: 10.1039/c5lc01356a.

[93] D. Lee, A. Erickson, T. You, A. T. Dudley, and S. Ryu, "Pneumatic microfluidic cell compression device for high-throughput study of chondrocyte mechanobiology," *Lab Chip*, vol. 18, no. 14, pp. 2077–2086, 2018, doi: 10.1039/c8lc00320c.

[94] A. Mainardi, "Towards the knee on a chip: development of a microfluidic platform for the mechanical stimulation of three dimensional cartilaginous constructs," 2016.

[95] P. Occhetta *et al.*, "Hyperphysiological compression of articular cartilage induces an osteoarthritic phenotype in a cartilage-on-a-chip model," *Nat. Biomed. Eng.*, vol. 3, no. 7, pp. 545–557, 2019, doi: 10.1038/s41551-019-0406-3.

[96] A. Pirosa, R. Gottardi, P. G. Alexander, and R. S. Tuan, "Engineering in-vitro stem cell-based vascularized bone models for drug screening and predictive toxicology," *Stem Cell Res. Ther.*, vol. 9, no. 1, 2018, doi: 10.1186/s13287-018-0847-8.

[97] S. Bersini *et al.*, "A microfluidic 3D in vitro model for specificity of breast cancer metastasis to bone," *Biomaterials*, vol. 35, no. 8, pp. 2454–2461, 2014, doi: 10.1016/j.biomaterials.2013.11.050.

[98] G. Nasello, P. Alamán-Díez, J. Schiavi, M. Á. Pérez, L. McNamara, and J. M. García-Aznar,

"Primary Human Osteoblasts Cultured in a 3D Microenvironment Create a Unique Representative Model of Their Differentiation Into Osteocytes," *Front. Bioeng. Biotechnol.*, vol. 8, no. April, pp. 1–14, 2020, doi: 10.3389/fbioe.2020.00336.

[99]   M. Ehrbar *et al.*, "Biomolecular hydrogels formed and degraded via site-specific enzymatic reactions," *Biomacromolecules*, vol. 8, no. 10, pp. 3000–3007, 2007, doi: 10.1021/bm070228f.

[100] H. K. Heywood, D. L. Bader, and D. A. Lee, "Rate of oxygen consumption by isolated articular chondrocytes is sensitive to medium glucose concentration," *J. Cell. Physiol.*, vol. 206, no. 2, pp. 402–410, 2006, doi: 10.1002/jcp.20491.

[101] T. H. Lin, H. Y. Jhang, F. C. Chu, and C. A. Chung, "Computational modeling of nutrient utilization in engineered cartilage," *Biotechnol. Prog.*, vol. 29, no. 2, pp. 452–462, 2013, doi: 10.1002/btpr.1687.

[102] M. Lemme and C. Conficconi, "Design of a microfluidic device for cyclic mechanical stimulation of three-dimensional cardiac cell constructs," 2014.

[103] S. Hosmane *et al.*, "Valve-based microfluidic compression platform: Single axon injury and regrowth," *Lab Chip*, vol. 11, no. 22, pp. 3888–3895, 2011, doi: 10.1039/c1lc20549h.

[104] E. P. Chan, Y. Hu, P. M. Johnson, Z. Suo, and C. M. Stafford, "Spherical indentation testing of poroelastic relaxations in thin hydrogel layers," *Soft Matter*, vol. 8, no. 5, pp. 1492–1498, 2012, doi: 10.1039/c1sm06514a.

[105] Q. T. Nguyen, Y. Hwang, A. C. Chen, S. Varghese, and R. L. Sah, "Cartilage-like mechanical properties of poly (ethylene glycol)- diacrylate hydrogels," *Biomaterials*, vol. 33, no. 28, pp. 6682–6690, 2012, doi: 10.1038/jid.2014.371.

[106] E. A. Phelps *et al.*, "Maleimide cross-linked bioactive PEG hydrogel exhibits improved reaction kinetics and cross-linking for cell encapsulation and in-situ delivery," *Adv. Mater.*, vol. 24, no. 1, pp. 1–12, 2013, doi: 10.1002/adma.201103574.Maleimide.

[107] G. S. Offeddu, E. Axpe, B. A. C. Harley, and M. L. Oyen, "Relationship between permeability and diffusivity in polyethylene glycol hydrogels," *AIP Adv.*, vol. 8, no. 10, pp. 1–6, 2018, doi: 10.1063/1.5036999.

[108] S. C. Skaalure, S. C. Oppegard, and D. T. Eddington, "Characterization of sterilization techniques on a microfluidic oxygen delivery device," *J. Undergrad. Res. Univ. Illinois Chicago*, vol. 2, no. 1, 2008, doi: 10.5210/jur.v2i1.7462.

[109] F. Wei *et al.*, "Activation of Indian hedgehog promotes chondrocyte hypertrophy and upregulation of MMP-13 in human osteoarthritic cartilage," *Osteoarthr. Cartil.*, vol. 20, no. 7, pp. 755–763, 2012, doi: 10.1016/j.joca.2012.03.010.

[110] J. C. H. Leijten *et al.*, "GREM1, FRZB and DKK1 mRNA levels correlate with osteoarthritis and are regulated by osteoarthritis-associated factors," *Arthritis Res. Ther.*, vol. 15, no. 5, pp. 1–11, 2013, doi: 10.1186/ar4306.

[111] S. Miot *et al.*, "In Vitro and In Vivo Validation of Human and Goat Chondrocyte Labeling by Green Fluorescent Protein Lentivirus Transduction," *Tissue Eng. Part C Methods*, vol. 16, no. 1, pp. 11–21, Mar. 2009, doi: 10.1089/ten.tec.2008.0698.

[112] C. Probst, S. Schneider, and P. Loskill, "High-throughput organ-on-a-chip systems: Current status and remaining challenges," *Curr. Opin. Biomed. Eng.*, vol. 6, pp. 33–41, 2018, doi: https://doi.org/10.1016/j.cobme.2018.02.004.

[113] M. M. Blum and T. C. Ovaert, "Experimental and numerical tribological studies of a boundary lubricant functionalized poro-viscoelastic PVA hydrogel in normal contact and sliding," *J. Mech. Behav. Biomed. Mater.*, vol. 14, pp. 248–258, 2012, doi: 10.1016/j.jmbbm.2012.06.009.

[114] M. R. DiSilvestro, Q. Zhu, M. Wong, J. S. Jurvelin, and J. K. F. Suh, "Biphasic poroviscoelastic

simulation of the unconfined compression of articular cartilage: I - Simultaneous prediction of reaction force and lateral displacement," *J. Biomech. Eng.*, vol. 123, no. 2, pp. 191–197, 2001, doi: 10.1115/1.1351890.

[115] T. Komori, "Regulation of bone development and extracellular matrix protein genes by RUNX2," *Cell Tissue Res.*, vol. 339, no. 1, pp. 189–195, 2010, doi: 10.1007/s00441-009-0832-8.

[116] K. D. Huebner, N. G. Shrive, and C. B. Frank, "Dexamethasone inhibits inflammation and cartilage damage in a new model of post-traumatic osteoarthritis," *J. Orthop. Res.*, vol. 32, no. 4, pp. 566–572, 2014, doi: 10.1002/jor.22568.

[117] M. Bongio, S. Lopa, M. Gilardi, S. Bersini, and M. Moretti, "A 3D vascularized bone remodeling model combining osteoblasts and osteoclasts in a CaP nanoparticle-enriched matrix," *Nanomedicine*, vol. 11, no. 9, pp. 1073–1091, 2016, doi: 10.2217/nnm-2015-0021.